PHYSICAL REVIEW B **107**, 235135 (2023)

Editors' Suggestion

Symmetry-conserving maximally projected Wannier functions

K. Koepernik,[1] O. Janson,[1] Yan Sun,[2] and J. van den Brink[1,3]
[1]*Institute for Theoretical Solid State Physics, IFW Dresden, 01069 Dresden, Germany*
[2]*Max Planck Institute for Chemical Physics of Solids, 01187 Dresden, Germany*
[3]*Institute for Theoretical Physics and Würzburg-Dresden Cluster of Excellence ct.qmat,*
Technische Universität Dresden, 01069 Dresden, Germany

(Received 3 December 2021; revised 13 April 2023; accepted 17 May 2023; published 20 June 2023)

To obtain a local description with a small basis size from density functional theory codes often a transformation to a local orthonormal Wannier function basis is desirable. In order to do so while enforcing the constraints of the space group symmetry the symmetry conserving maximally projected Wannier functions (SCMPWF) approach has been implemented in the full potential-local orbital code, FPLO. SCMPWFs are obtained from the initial step of the maximally localized Wannier function algorithm, projecting a subset of wave functions onto a set of suitably chosen local trial functions with prescribed symmetry properties with subsequent orthonormalization. The particular nature of the local orbitals in FPLO makes them an ideal set of projectors since they are constructed to be a small basis adapted to the occupied sector and the lowest-lying unoccupied states. While in many cases projection onto the FPLO basis orbitals is sufficient, the option is there to choose particular local linear combinations as projectors, in order to treat cases of bond centered Wannier functions. This choice turns out to lead to very localized Wannier functions, which obey the space group symmetry of the crystal by construction. Furthermore we discuss the interplay of the Berry connection and position operator and especially its possible approximation, symmetries, and the optimal choice of Bloch sum phase gauge in cases where the basis is not explicitly known. We also introduce various features, which are accessible via the FPLO implementation of SCMPWFs, discuss and compare performance and provide example applications.

DOI: 10.1103/PhysRevB.107.235135

I. INTRODUCTION

A. Wannier functions and FPLO

Convenient basis states for the treatment of extended systems are extended states which carry a pseudo-momentum quantum number. On the other hand, chemistry is more intuitively described by local basis states, which resemble atomic orbitals, while extended model Hamiltonians are often built from (implicit) atomic entities (tight binding). Although several numerical methods exist, which treat molecules and solids with an atom like basis, many contemporary highly accurate density functional theory (DFT) codes are based on modified plane wave bases. To gain back the local description, a transformation to a local orthonormal Wannier function basis is desirable.

The usefulness of Wannier functions has gained new momentum in the context of topological properties of extended systems, for whose determination a downfolding of the whole system's Hamiltonian onto a smaller model is very helpful. While smaller models reduce the often heavy burden of calculating topological quantities, numerical accuracy, especially symmetry conservation, becomes an important issue as well, in particular for higher order transport properties, which involve taking derivatives (e.g., Berry curvature dipole [1]) or for tensorial properties.

Wannier functions (WFs) can be defined in many ways due to the gauge freedom in choosing a unitary transformation among the wave functions to be wannierized. One way of fixing the gauge, now widely used, is the requirement of maximum localization [2–4] (ignoring the constraints of the space group symmetry). This is an rather intricate algorithm which becomes even more complicated, if space group symmetry is added [5,6].

Extending the ideas of Ref. [7] to retain full symmetry information we implemented a different scheme into the full potential local orbital code, FPLO [8], as outlined in Ref. [9]. This scheme, which we call symmetry conserving maximally projected Wannier functions (SCMPWF), basically represents the zeroth order approximation of the maximally localized approach [2], in projecting a subset of wave functions onto a set of suitably chosen local trial functions with subsequent orthonormalization.

The particular nature of the local orbitals in FPLO make them an ideal set of projectors, since they are constructed to be a "chemical" basis. In many cases, projection onto the FPLO basis orbitals is sufficient, while the option is there to choose particular local linear combinations (molecular orbitals [MO]) as projectors, in order to treat cases of bond centered Wannier functions. It turns out that our choice leads to highly localized Wannier functions, which obey the space group symmetry of the crystal by construction. In cases where the resulting WFs are not well localized, it is due to a bad choice and can be fixed.

Many similar projective schemes have been proposed before, often including localization criteria (Refs. [10–12] and references therein) as well as including symmetry considerations [13]. The main difference to our method is that ours is straightforward and simple as the approach of Ref. [7].

On top it conserves symmetry and is generally applicable to entangled bands with very few adjustable parameters.

The main challenge of our approach is that the user has to decide where the WFs shall sit and which local symmetry they shall have. However, this is often exactly what one wants to do, when constructing a Wannier model for a given subset of bands. The strong connection of the FPLO basis and the resulting WFs and the comparatively small basis size allows for automatic wannierization, which is nothing but constructing the Löwdin orthogonalized FPLO basis. In principle, everything which can be expressed in WFs could be transformed back into the nonorthogonal FPLO basis, which opens the possibility to circumvent WFs altogether, although this is less efficient.

The method described here is used in conjunction with the FPLO density functional (DFT) code, but it can also be used whenever a Hamiltonian is given in a local basis [tight-binding (TB) models], even if the basis is not explicitly known. This can, for instance, be helpful to further reduce the dimensionality of a TB model.

The structure of a local basis code also requires modifications to the way the Berry connection/curvature need to be calculated. The connection of these quantities to the position operator was discussed in great detail in Ref. [14] before the recognition of their fundamental nature for topological properties of mater. The local basis formulation of the Berry operators presented here offers insights into the correct way of neglecting the position operator matrix elements and into the correct phase choice of Bloch sums, especially when the Wannier basis is not explicitly known, in particular, for tight-binding models.

B. Outline

This paper thus serves as a reference to the Wannier module of FPLO and describes the algorithm underlying it as well as the post-processing tools, including semi-infinite slab calculations, Weyl point search and calculation of Z_2 topological indices. In Sec. II, we outline in detail the construction of symmetry conserving maximally projected Wannier functions. In Sec. III, the position operator matrix elements are discussed. Sec. IV introduces various features which are accessible via the FPLO implementation of SCMPWF and Sec. V discusses and compares performance and gives example applications, in particular on the construction of tight-binding models and band disentangling, the calculation of the Berry curvature and anomalous Hall conductivity [15,16].

II. FORMALISM AND METHOD

A. Wannier orbitals in FPLO

The FPLO basis consists of local atom like orbitals $\Phi_{\boldsymbol{R}s\nu}(\boldsymbol{r})$ localized at site $\boldsymbol{s}$ in unit cell $\boldsymbol{R}$, having atom like quantum numbers (qns) $\nu = nlm\sigma$ without spin orbit coupling and $\nu = nlj\mu$ in the four-component full-relativistic mode, where n is the main quantum number, lm are the qns. of real spherical harmonics, σ is the spin index and $lj\mu$ are the qns. of a standard (complex) spherical spinor (see Appendix A 1).

From these orbitals Bloch sums can be formed

$$\Phi^{\boldsymbol{k}}_{s\nu}(\boldsymbol{r}) = \frac{1}{\sqrt{N}}\sum_{\boldsymbol{R}} \mathrm{e}^{i\boldsymbol{k}(\boldsymbol{R}+\lambda\boldsymbol{s})}\Phi_{\boldsymbol{R}s\nu}(\boldsymbol{r}), \tag{1}$$

where N is the number of unit cells in the Born-von-Kármán (BvK) torus. The chosen normalization is further discussed in Appendix A 2. The parameter λ allows to choose the phase gauge and is of interest later. The default gauge in FPLO and hence in constructing the Wannier functions is the *relative* gauge ($\lambda = 1$) in which matrix elements of an operator between two Bloch sums only depend on the relative vector connecting the two orbital locations in each term of the sum. In post processing modules, which use the WFs, the *periodic* gauge ($\lambda = 0$) can be chosen, in which the Bloch sums are periodic in $\boldsymbol{k}$ space.

The FPLO orbitals from different sites are in general nonorthogonal, which leads to a nontrivial overlap matrix $S^{\boldsymbol{k}}$. This avoids complicated orbital shapes away from the atomic core region and in fact the SCMPWF transformation is essentially nothing but the orthogonalization of (a subset of) our local orbitals (LO). Introducing the row vector $\Phi^{\boldsymbol{k}}$ of all orbitals and the matrix of wave function coefficients $C^{\boldsymbol{k}}$, the overlap and Hamiltonian matrices read

$$\begin{aligned} S^{\boldsymbol{k}} &= \langle \Phi^{\boldsymbol{k}} | \Phi^{\boldsymbol{k}} \rangle, \\ H^{\boldsymbol{k}} &= \langle \Phi^{\boldsymbol{k}} | \hat{H} | \Phi^{\boldsymbol{k}} \rangle, \end{aligned} \tag{2}$$

and the eigenvalue problem becomes

$$H^{\boldsymbol{k}}C^{\boldsymbol{k}} = S^{\boldsymbol{k}}C^{\boldsymbol{k}}\varepsilon^{\boldsymbol{k}}, \quad C^{\boldsymbol{k}+}S^{\boldsymbol{k}}C^{\boldsymbol{k}} = 1, \tag{3}$$

which gives the row vector of full wave functions

$$\Psi^{\boldsymbol{k}} = \Phi^{\boldsymbol{k}}C^{\boldsymbol{k}}. \tag{4}$$

as a linear combination of the Bloch sums of LOs. In the following, we will often suppress the orbital/WF indices (and sometimes site indices). The corresponding expressions must then be understood as subblocks of vectors of functions or matrices.

We will now expand on the method of Refs. [7,9] by introducing the symmetrization and Bloch gauges. In order to obtain Wannier functions, one needs to Fourier back transform the extended wave functions $\Psi^{\boldsymbol{k}}$ including some unitary matrix $\mathcal{U}^{\boldsymbol{k}}$ which constitutes a general gauge choice

$$w_{\boldsymbol{R}c} = \frac{1}{\sqrt{N}}\sum_{\boldsymbol{k}} \mathrm{e}^{-i\boldsymbol{k}(\boldsymbol{R}+\lambda\boldsymbol{c})}(\Psi^{\boldsymbol{k}}\mathcal{U}^{\boldsymbol{k}})_c, \tag{5}$$

where the normalization was chosen such that with $\mathcal{U}^{\boldsymbol{k}+}_{c'}\mathcal{U}^{\boldsymbol{k}}_{c} = \delta_{c'c}$ also $\langle w_{\boldsymbol{R}'c'} | w_{\boldsymbol{R}c} \rangle = \delta_{\boldsymbol{R}'\boldsymbol{R}}\delta_{c'c}$ holds. The phase gauge (λ term) is there for convenience and can be thought of as a part of $\mathcal{U}$. The difference between various methods to calculate Wannier functions is the choice of $\mathcal{U}$. In the following, we will describe our choice and argue why it is reasonable. It is a matter of experience through many calculations that a certain setup seems to guarantee localization if done right. Basically, if one knows from band characters and symmetry conditions which orbitals engender a certain band complex then the WFs obtained from projection onto these orbitals will be localized. In essence, SCMPWF as implemented in FPLO are a symmetry and chemistry based basis reduction. Note that the resulting WFs cannot in general be more localized than the corresponding projector orbitals, due to orthogonalization tails.

In order to obtain Wannier functions we need to select a physically motivated subset of wave functions (bands) and construct a weighted Hilbert subspace "projector"

$$\mathcal{H} = \sum_{\boldsymbol{k}} |\Psi^{\boldsymbol{k}}\rangle h^{\boldsymbol{k}} \langle \Psi^{\boldsymbol{k}}| \tag{6}$$

from them, where $h^{\boldsymbol{k}}$ is an energy dependent diagonal matrix with values between zero and one, which discards the unwanted part of the band structure. In contrast to a pure projector (e.g., Ref. [12]), the noninteger weights $h^{\boldsymbol{k}}$ help adjust the WF- to the target-band structure without the need to minimize a spread functional.

This Hilbert subspace must contain at least as many bands as the number of desired Wannier functions. It can contain more bands, however, of which some get discarded by the projection onto trial functions by the fact that the overlap of the trial functions with some wave-functions will be small.

If properly chosen this Hilbert space is mainly spanned by a well defined linear combination of a subset of the original LOs. For generality, we consider local linear combinations of LOs, which can be called molecular orbitals (MOs). Note that orthogonality of the MOs in this stage is not required. In detail, we construct MOs

$$\phi_{\boldsymbol{c}i} = \sum_{\boldsymbol{R}s\nu'} \Phi_{\boldsymbol{R}s\nu'} U_{\boldsymbol{R}s\nu',\boldsymbol{c}i} \tag{7}$$

sitting at an imagined Wannier center $\boldsymbol{c}$, having an index i from LOs $\Phi_{\boldsymbol{R}s\nu'}$ in the vicinity of $\boldsymbol{c}$. In practice, the input $U_{\boldsymbol{R}s\nu',\boldsymbol{c}i}$ consists of a few lines specifying the center $\boldsymbol{c}$, the contributing site numbers, difference vectors from the center to these sites and weights. In the simplest case, $U_{\boldsymbol{R}s\nu',\boldsymbol{c}i} = \delta_{\boldsymbol{R}+\boldsymbol{s},\boldsymbol{c}}\delta_{\nu',i}$ for a subset of orbitals. U can also contain a transformation onto different local quantization axes in which the LOs are rotated, which helps to yield WFs adapted to certain local symmetries.

At this step, we insist that the set of MOs transforms properly under the space group. A space group operation with point group matrix α and translation $\boldsymbol{\tau}$ is given in the Seitz notation by $g = \{\alpha|\boldsymbol{\tau}\}$. The atom positions transform as

$$g(\boldsymbol{R}+\boldsymbol{s}) = \alpha(\boldsymbol{R}+\boldsymbol{s}) + \boldsymbol{\tau} = \alpha\boldsymbol{R} + g\boldsymbol{s}. \tag{8}$$

The transformed site can be backfolded onto the original set of sites via

$$g\boldsymbol{s} = \boldsymbol{s}_g + \boldsymbol{R}_{g,s}, \tag{9}$$

where $\boldsymbol{s}_g$ is the site in the original set of sites which $\boldsymbol{s}$ gets mapped onto by g and $\boldsymbol{R}_{g,s}$ is a lattice vector. This backfolding is needed since Bloch sums of the same site in two different unit cells can differ in phase and since sites are indices to the Bloch sums. Hence, consistency requires that we always consider the functions in the original set of sites. Of course, also the Wannier centers $\boldsymbol{c}$ transform this way. Note that in our formalism, the Wannier centers are not an output of the calculation but an input. The most general transformation property of local orbitals or MOs is given by (see Appendix B 2)

$$\{\alpha|\tau\}\phi_{\boldsymbol{c}i} = \sum_{i'} \phi_{\alpha\boldsymbol{R}+\boldsymbol{R}_{g,c},\boldsymbol{c}_g i'} D_{\boldsymbol{c},i'i}(g), \tag{10}$$

where $D_{\boldsymbol{c},i'i}$ is a matrix which mixes the MOs at center $\boldsymbol{c}$ such that MOs at the transformed center $\boldsymbol{c}_g$ are obtained. In essence, if a MO at some center is picked, all MOs which are symmetry related at the same center as well as all equivalent MOs at symmetry related centers must be included into the set of projectors. The sets at related centers can be arbitrarily unitary mixed. Knowing the transformation properties of the FPLO orbitals and the MO matrix U in Eq. (7), D in Eq. (10) is fully defined. By constructing the MOs this way we have explicit information about the symmetry properties of the resulting Wannier functions. In most cases, the MOs are identical to a subset of our LOs.

Using Eq. (A8) in Appendix A 2, we can calculate the projection of the Hilbert subspace Eq. (6) onto a MO as

$$\begin{aligned}\mathcal{H}|\phi_{\boldsymbol{R}\boldsymbol{c}}\rangle &= \sum_{\boldsymbol{k}} |\Psi^{\boldsymbol{k}}\rangle h^{\boldsymbol{k}} \langle \Psi^{\boldsymbol{k}}|\phi_{\boldsymbol{R}\boldsymbol{c}}\rangle \\ &= \sum_{\boldsymbol{k}} \left(|\Psi^{\boldsymbol{k}}\rangle h^{\boldsymbol{k}} C^{\boldsymbol{k}+} S^{\boldsymbol{k}} U^{\boldsymbol{k}} \frac{1}{\sqrt{N}} \right)_{\boldsymbol{c}} \mathrm{e}^{-i\boldsymbol{k}(\boldsymbol{R}+\lambda\boldsymbol{c})} \\ &= \frac{1}{\sqrt{N}} \sum_{\boldsymbol{k}} \tilde{w}_{\boldsymbol{c}}^{\boldsymbol{k}} \mathrm{e}^{-i\boldsymbol{k}(\boldsymbol{R}+\lambda\boldsymbol{c})},\end{aligned} \tag{11}$$

which defines the Bloch sums

$$\tilde{w}_{\boldsymbol{c}i}^{\boldsymbol{k}} = (|\Psi^{\boldsymbol{k}}\rangle h^{\boldsymbol{k}} C^{\boldsymbol{k}+} S^{\boldsymbol{k}} U^{\boldsymbol{k}})_{\boldsymbol{c}i} \tag{12}$$

of the raw (not orthonormal) Wannier functions as well as the phase gauge to be used in the Fourier back transformation into real space.

This simple projection completely defines $\mathcal{U}^{\boldsymbol{k}}$ in Eq. (5) (besides orthonormality) and is quite intuitive: define the desired subset of bands by specifying $h^{\boldsymbol{k}}$ and project out the part which has overlap with suitably selected MOs (trial functions). If these MOs span the most part of this Hilbert space, the result must be the Wannier functions describing $\mathcal{H}$. The raw WF contains the weights $C^{\boldsymbol{k}+}S^{\boldsymbol{k}}U^{\boldsymbol{k}}$, which can be interpreted as the "square root" of the band weights of the MOs in $\Psi^{\boldsymbol{k}}$; a form of band characters (fat bands) of the considered orbitals, only with the phase information retained. So, we basically sum wave functions according to MO weights contained in them.

We apply the Löwdin procedure to Eq. (12) in order to obtain orthonormal WFs, which are guaranteed to have the smallest least square deviation from the raw functions: we divide by the square root of the overlap matrix of the raw WFs

$$O^{\boldsymbol{k}} = \langle \tilde{w}^{\boldsymbol{k}} | \tilde{w}^{\boldsymbol{k}} \rangle = U^{\boldsymbol{k}+} S^{\boldsymbol{k}} C^{\boldsymbol{k}} (h^{\boldsymbol{k}})^2 C^{\boldsymbol{k}+} S^{\boldsymbol{k}} U^{\boldsymbol{k}} \tag{13}$$

and obtain the orthonormal Bloch sums of maximally projected WFs

$$w_{\boldsymbol{c}i}^{\boldsymbol{k}} = \left(\tilde{w}^{\boldsymbol{k}} \frac{1}{\sqrt{O^{\boldsymbol{k}}}} \right)_{\boldsymbol{c}i}. \tag{14}$$

The inverse square root of the overlap is calculated using the eigendecomposition $O^{\boldsymbol{k}} Z^{\boldsymbol{k}} = Z^{\boldsymbol{k}} o^{\boldsymbol{k}}$ according to $(O^{\boldsymbol{k}})^{-1/2} = Z^{\boldsymbol{k}} \frac{1}{\sqrt{o^{\boldsymbol{k}}}} Z^{\boldsymbol{k}+}$. Furthermore, since we know the symmetry transformation $U^{\boldsymbol{k}} = U^{\boldsymbol{k}'} D$, we also know the transformation property $O^{\boldsymbol{k}} = D^+ O^{\boldsymbol{k}'} D$, which gives $Z^{\boldsymbol{k}} = D^+ Z^{\boldsymbol{k}'}$ and $(O^{\boldsymbol{k}})^{-\frac{1}{2}} = D^+ (O^{\boldsymbol{k}'})^{-\frac{1}{2}} D$. So, the WFs $w_{\boldsymbol{c}i}^{\boldsymbol{k}}$ transforms as the MOs themselves. Finally, we Fourier back transform into real space by inserting Eq. (14) into Eq. (11):

$$w_{\boldsymbol{R}ci} = \frac{1}{\sqrt{N}} \sum_{\boldsymbol{k}} w^{\boldsymbol{k}}_{ci} \mathrm{e}^{-i\boldsymbol{k}(\boldsymbol{R}+\lambda\boldsymbol{c})}. \tag{15}$$

In summary, our gauge fixing matrix when transforming wave functions into Wannier functions is obtained by basically picking linear combinations of wave functions of a Hilbert subspace which have maximal projection (band weight) for a number of MOs/LOs. The result then is orthogonalized and Fourier back transformed into real space to obtain the Wannier functions, which by construction have maximum resemblance to the MOs. Since the projectors are identical to or are constructed out of our original LOs, which form the basis of the wave functions to begin with, the projection result is expected to be closer to the picked subspace than what is obtained from the original idea of Ref. [7] of projecting onto hand-made atom like trial functions, which are not a basis of the wave function formation.

In the extreme case, where we calculate a Wannier basis as large as the FPLO basis (automatic mode), we can use $\phi = \Phi$ for all orbitals and $h^{\boldsymbol{k}} = 1$ (all bands), which gives $U = 1$ and with $C^{\boldsymbol{k}} C^{\boldsymbol{k}+} = (S^{\boldsymbol{k}})^{-1}$:

$$\tilde{w}^{\boldsymbol{k}} = \Phi^{\boldsymbol{k}}, \tag{16}$$

which results in the orthonormalized WFs

$$w^{\boldsymbol{k}} = \Phi^{\boldsymbol{k}} \frac{1}{\sqrt{\langle \Phi^{\boldsymbol{k}} | \Phi^{\boldsymbol{k}} \rangle}}, \tag{17}$$

which is nothing but the Löwdin orthonormalized FPLO basis. From this, it is also clear why we need to use the same λ in the Fourier back transformation as in the definition of the orbital Bloch sums Eq. (1). If $\Phi^{\boldsymbol{k}}$ were orthonormal the Fourier back transformation of Eq. (1) would just yield the (assumed to be orthonormal) local orbitals, i.e., Wannier functions.

Equations (12) and (14) can be written in matrix form as

$$w^{\boldsymbol{k}} = \Psi^{\boldsymbol{k}} \mathcal{U}^{\boldsymbol{k}} = \Phi^{\boldsymbol{k}} a^{\boldsymbol{k}}, \tag{18}$$

which emphasizes either the connection to the wave functions or the basis. While

$$\mathcal{U}^{\boldsymbol{k}} = h^{\boldsymbol{k}} C^{\boldsymbol{k}+} S^{\boldsymbol{k}} U^{\boldsymbol{k}} \frac{1}{\sqrt{O^{\boldsymbol{k}}}} \tag{19}$$

is projective unitary $\mathcal{U}^{\boldsymbol{k}+}\mathcal{U}^{\boldsymbol{k}} = 1$,

$$a^{\boldsymbol{k}} = C^{\boldsymbol{k}} \mathcal{U}^{\boldsymbol{k}} \tag{20}$$

fulfills $a^{\boldsymbol{k}+} S^{\boldsymbol{k}} a^{\boldsymbol{k}} = 1$ since the basis has nontrivial overlap. The Hamiltonian in the Wannier basis then becomes

$$H^{(w)\boldsymbol{k}} = \langle w^{\boldsymbol{k}} | \hat{H} | w^{\boldsymbol{k}} \rangle = \mathcal{U}^{\boldsymbol{k}+} \varepsilon^{\boldsymbol{k}} \mathcal{U}^{\boldsymbol{k}} = a^{\boldsymbol{k}+} H^{\boldsymbol{k}} a^{\boldsymbol{k}} \tag{21}$$

with $H^{\boldsymbol{k}}$ according to Eq. (2). A general operator $\hat{B}$ with matrix elements between LO Bloch sums $B^{\boldsymbol{k}}$ then reads in Wannier basis $B^{(w)\boldsymbol{k}} = \langle w^{\boldsymbol{k}} | \hat{B} | w^{\boldsymbol{k}} \rangle = a^{\boldsymbol{k}+} B^{\boldsymbol{k}} a^{\boldsymbol{k}}$.

B. Accuracy and localization

If the Wannier transformation is well set up, the eigenvalues of Eq. (21) will reproduce the band structure of the chosen band subspace. In cases of an isolated band complex with a WF basis of the same dimension, the Wannier and FPLO band structure are usually identical. If band disentangling is needed, the dimension of the Hilbert subspace is usually larger than the WF basis dimension [3]. Then $h^{\boldsymbol{k}}$ can be chosen such that an agreement of the two band structures for the targeted subset of bands is achieved to within an error of the order of 10 meV.

For post processing, the wannierized operators need to be stored in their real space representation which is obtained from

$$B^{(\mathrm{TB})}_{\boldsymbol{0}\boldsymbol{c}',\boldsymbol{R}\boldsymbol{c}} = \sum_{\boldsymbol{k}} f_{\boldsymbol{k}} \mathrm{e}^{-i\boldsymbol{k}(\boldsymbol{R}+\lambda(\boldsymbol{c}-\boldsymbol{c}'))} B^{(w)\boldsymbol{k}}_{\boldsymbol{c}',\boldsymbol{c}}, \tag{22}$$

where in the simplest case $f_{\boldsymbol{k}} = 1/N$. The superscript stands for tight-binding (TB). From the tight binding representation the WF Bloch representation is recovered via

$$B^{(\mathrm{BL})\boldsymbol{k}}_{\boldsymbol{c}'\boldsymbol{c}} = \sum_{\boldsymbol{R}} \mathrm{e}^{i\boldsymbol{k}(\boldsymbol{R}+\lambda(\boldsymbol{c}-\boldsymbol{c}'))} B^{(\mathrm{TB})}_{\boldsymbol{0}\boldsymbol{c}',\boldsymbol{R}\boldsymbol{c}}. \tag{23}$$

Besides the TB-representation of the operators also the basis representation of the WFs themselves is useful. Inserting Eqs. (1) and (18) into Eq. (15), one gets

$$w_{\boldsymbol{R}\boldsymbol{c}} = \sum_{\boldsymbol{R}'} \Phi_{\boldsymbol{R}'\boldsymbol{s}} a_{\boldsymbol{R}'\boldsymbol{s},\boldsymbol{R}\boldsymbol{c}} \tag{24}$$

with the coefficients

$$a_{\boldsymbol{0}\boldsymbol{s},\boldsymbol{R}-\boldsymbol{R}',\boldsymbol{c}} = a_{\boldsymbol{R}'\boldsymbol{s},\boldsymbol{R}\boldsymbol{c}} = \frac{1}{N} \sum_{\boldsymbol{k}} \mathrm{e}^{-i\boldsymbol{k}(\boldsymbol{R}+\lambda\boldsymbol{c}-\boldsymbol{R}'-\lambda\boldsymbol{s})} a^{\boldsymbol{k}}_{\boldsymbol{s}\boldsymbol{c}}. \tag{25}$$

These coefficients can serve to illustrate the WF decay and hence degree of localization.

At this step, we have two possibilities. Either a real space cutoff ρ is defined such that all matrix elements from a WF center $\boldsymbol{c}'$ to another center at $\boldsymbol{R}+\boldsymbol{c}$ are discarded if $|\boldsymbol{R}+\boldsymbol{c}-\boldsymbol{c}'| > \rho$, or one chooses the maximum possible set of center pairs $\boldsymbol{c}', \boldsymbol{R}\boldsymbol{c}$ which are consistent with the $\boldsymbol{k}$ mesh used in the Fourier back transformation, which is the mesh used in the self consistent DFT calculation (new since FPLO version 19.00). A cutoff is useful to reduce storage space, to speed up the calculation or to aim at a WF model with minimal number of parameters (not as accurate, of course).

Operators recovered via Eq. (23) at a post processing stage are in general different from their exact Wannier transform $B^{(w)\boldsymbol{k}}$ for a $\boldsymbol{k}$ point not included in the $\boldsymbol{k}$ mesh. This is the very essence of Wannier interpolation. Hence, the resulting band structure after this transformation through the real space representation will also differ from the band structure obtained directly from the exact transform Eq. (21). The size of this error determines the quality of the Wannier fit.

If the error is unacceptable there are two possible reasons: either the cutoff removed too much information and needs to be increased or the maximum possible cutoff is not big enough, which is equivalent to saying that the underlying $\boldsymbol{k}$ mesh is not fine enough. In practice a cutoff between 25–40 Bohr radii is sufficient to reduce this error to a satisfactory degree. An exception is the automatic mode in which all FPLO orbitals become Wannier functions. Since, the higher lying states are spanned by polarization orbitals which have a larger extent than the valence orbitals the corresponding WFs are also more extended.

To further elucidate this issue we discuss the Fourier back transformation in more detail. If symmetry was of no concern the acceptable $\boldsymbol{R}$ mesh in Eqs. (22) and (23) is determined entirely by the $\boldsymbol{k}$ mesh [17]. The $\boldsymbol{k}$ mesh is defined as a regular grid defined via N_i subdivisions of the three primitive reciprocal lattice vectors. The $\boldsymbol{R}$ mesh then is the dual mesh, i.e., the smallest parallelepiped supercell in real space for which $\exp(i\boldsymbol{kR}) \neq 1$. This supercell is the reciprocal cell of the smallest grid micro cell. This mesh is not optimal, instead one folds the vectors of this mesh back to form a set of vectors surrounding the origin and having smallest possible length. Localization of the Wannier functions ensures that the vectors of larger length become more and more unimportant.

If $\boldsymbol{R}$ vectors were included which lie outside of the supercell the Wannier functions will acquire replica features: the contributions of the local orbitals to a Wannier function as measured by $a_{\boldsymbol{0}s,\boldsymbol{Rc}}$ first decrease exponentially with increasing distance of the orbital to the Wannier center until distances are reached which are comparable to multiples of the real space length corresponding to the inverse of the smallest $\boldsymbol{k}$-mesh distance. At these points the orbital contributions start increasing again, i.e., the Wannier functions are quasiperiodic objects in real space with periods defined by the inverse of the smallest $\boldsymbol{k}$-mesh distances.

Since we construct symmetry conserving Wannier functions, ideally our $\boldsymbol{R}$ mesh would be chosen to reflect the symmetry. This is achieved by backfolding the supercell vectors into the smallest possible spherical volume around the origin for each pair of WF centers $\boldsymbol{c}'$, $\boldsymbol{Rc}$. Then for all vectors of this set all vectors additionally obtained by symmetry are added to the set. Finally, weights are attached to all vectors such that the weights for symmetry related vectors are identical and that the sum of the weights of all vectors which are identical by supercell translations is one. This way we include vectors which violate the supercell condition, but replica do not occur due to the weighting. This algorithm determines the maximal number of real space vectors if no cutoff is used.

In order to reduce computation time, the $\boldsymbol{k}$ summation is done for the irreducible part of the mesh, which changes the effective weights to $f_{\boldsymbol{k}} = m_{\boldsymbol{k}}/N$ by multiplying with the multiplicity of the $\boldsymbol{k}$ point. This also requires an explicit symmetrization of the resulting matrix elements Eq. (22). This can easily be done, since the transformation properties of the WFs are explicitly known.

The symmetry which we consider is the full space group or in spin polarized full relativistic mode the group formed by operations, which do not invert the magnetic field, and by products of time reversal with the operations, which invert the field. In non-spin-polarized full relativistic mode time reversal is added as an extra symmetry.

Without spin orbit coupling the FPLO orbitals are real, which means that WFs which are obtained by projecting onto these orbitals are also real, if inversion symmetry is present. In relativistic mode the angular parts of the orbitals are spherical spinors, which are inherently complex, and so are the Wannier functions.

C. Practical application of the method

For applications of this method, the input needs to be discussed. We outlined above that, unless automatic mode is used, a Hilbert subspace of the full band structure needs to be chosen first. This is usually the bands around the Fermi level. Once this decision is made it has to be determined which orbitals contribute to these bands, which can be achieved by inspecting the orbital character of the band structure. At this point, one has to make sure that at each point in $\boldsymbol{k}$ space the number of bands highlighted by the orbital character is not smaller than the dimension of the desired Wannier basis. If this condition is not fulfilled, it is an indication that other orbitals contribute essentially to the targeted bands, and most importantly, it means that at these $\boldsymbol{k}$ points the raw WF overlap Eq. (13) will be singular. In cases where bond centered WFs are expected, simple molecular orbitals can be constructed from the relevant orbitals, otherwise the relevant orbitals are the projectors themselves.

In full relativistic mode, the option exists to project onto spherical spinors with $lj\mu$ quantum numbers [Appendix B 1, Eq. (A1)] or onto orbitals which are transformed into pseudo nonrelativistic symmetry with $lm\sigma$ qns [Appendix B 1, Eq. (B7)]. The latter are still four spinors but their large components are mostly resembling real spherical harmonics and they transform as real spherical harmonics. Additionally, local quantization axes can be chosen separately for the orbital angular momentum part as well as the spin part, which facilitates the construction of specialized models and band structure analysis.

The automatic mode can be used in two ways: either all basis orbitals are Wannierized or a reduced set is Wannierized, where all deep lying orbitals (semicore and deep lying valence orbitals), which do not contribute to the essential band structure are removed.

The last step is the choice of $h^{\boldsymbol{k}}$. We will discuss the case of entangled bands, since this is the most common case. Isolated band complexes are a trivial sub case. The targeted group of bands has a certain energy window $[E_{\mathrm{min}}, E_{\mathrm{max}}]$ in which it is located. When these bands are entangled with other bands it means that the projector's character is also appearing to a certain degree in the entangled irrelevant bands outside of the core energy window while character of the irrelevant bands flows into the targeted bands inside the core window due to hybridization. By choosing $h^{\boldsymbol{k}} = 1$ for the core energy window, one ensures that all targeted bands are fully included in the Hilbert subspace $\mathcal{H}$. At points where the targeted bands go outside the core energy window $\mathcal{H}$ will suffer a sudden collapse of some of its dimensions. Hence, we apply smooth Gaussian tails

$$h^{\boldsymbol{k}} = \exp\left(-\left(\frac{\varepsilon^{\boldsymbol{k}} - E_{\mathrm{min}\,/\,\mathrm{max}}}{\Delta_{\mathrm{min}\,/\,\mathrm{max}}}\right)^2\right) \tag{26}$$

at the lower and upper end of the energy window, where $\varepsilon^{\boldsymbol{k}}$ is the band energy of the considered band. The width parameter ΔE and the core window boundaries $E_{\mathrm{min}\,/\,\mathrm{max}}$ need to be adjusted to achieve several objectives. First, the resulting wannierized band structure should not be pulled to lower or higher energies. Secondly, Eq. (13) must not be singular and lastly the projector weight which flows into entangled bands outside the core window must be sufficiently sampled by the Gaussian tails.

It turns out that a core window which is smaller than the targeted window supplied with relatively wide tails are the best recipe in most entangled cases. This choice also increases the localization of the resulting WFs. In cases like bcc iron where the d bands are hybridized with sp bands of several tens of electron volts band width, the upper tail must be large enough (order 10 eV) to capture some d weight which flows far up into the sp bands. The resulting WFs are well localized as shown by the comparison of the results of Sec. IV C (Figs. 2–4) and Sec. V B (Figs. 10 and 11).

The main reason why the tails can be larger than expected is the fact that we project onto the very orbitals which are the basis of the band structure and hence get large weights from the d projectors in the core window while the tails collect only small parts of d character. In cases of isolated band complexes, the tails can be chosen very small and the core window set to the energy window of the isolated band complex.

When picking isolated band complexes for wannierization it must be avoided that the gaps above and below are topological. Otherwise, the WFs cannot be localized due to topological obstruction. This is usually flagged by the fact that it will be hard to find a set of projectors with basis size equal to the number of targeted bands. In such cases molecular orbitals might look like a possible basis. However, the result would either be singular or not localized (the other option is breaking of symmetry, which we exclude by construction). Essentially, one has to avoid to pick parts of split elementary band representations according to the concepts of topological quantum Chemistry [18].

There is a general recipe which circumvents this issue: always pick a set of projectors which forms a chemical basis, i.e., for instance, a $4s4p3d$ basis for a transition metal or a $5s5p/6s6p$ basis for many cases with heavy main group elements (sometimes even a simple $5p/6p$ basis might work). In compounds the collection of these minimal chemical bases for all atoms contributing to the targeted bands must be chosen as projectors. This way the probability to pick split elementary band representations is drastically lowered, since the size of the projector set also increases the number of the targeted bands and chemical basis sets are likely to form whole elementary band representations. This strategy increases the size of the resulting WF model, but for many applications, one actually wants the whole set of valence bands and the low lying conduction bands, which is actually formed by the chemical basis.

The algorithm described here can also be applied in the molecule mode of FPLO (which is a genuine 0d mode without the need of a simulation box) to construct basis-reduced Hamiltonian models.

III. TOPOLOGICAL ASPECTS

This section is not essential for the basic understanding of the general method of calculating SCMPWFs. It discusses the position operator matrix elements in the framework of local basis methods, which enter a complete description of the Berry connection and curvature.

A. Position operator

The Berry connection and its relation to the position operator $\boldsymbol{r}$ has been discussed widely, especially in the context of Wannier functions where it is given as the Fourier back transform of the $\boldsymbol{r}$-matrix elements between a WF in the first cell and all other WFs. The representation of the position operator in Bloch and Wannier basis has also has been extensively discussed in Ref. [14], where all expressions for Berry connection and curvature are provided although without the realization of their benefit in the study of topological aspects of electronic structures [19].

Here we will reiterate the representation of the position operator and introduce a basis invariant formulation which allows for consistent and arbitrary basis transformations and naturally lends itself to application in local orbital frameworks. A simple gauge dependent approximation for the Berry connection will be given, which is important in TB frameworks, where the basis is only implicitly known. In the following, we will deal with whole connection/curvature matrices to retain the transformation properties. The final Berry connection/curvature is a subspace trace of these matrices.

We start with the obvious observation that the position operator is not translation invariant, which makes its lattice Fourier transform $\boldsymbol{r}^{\boldsymbol{q}\boldsymbol{k}}$ nondiagonal in $\boldsymbol{k}$. Furthermore, the limit $\boldsymbol{q} \to \boldsymbol{k}$ is badly defined [see Eqs. (B27) and (B28) in Appendix B 3].

In the space of extended (Bloch) functions, let us introduce the operator identity

$$\boldsymbol{r} = \mathrm{e}^{i\boldsymbol{k}\boldsymbol{r}} i\nabla_{\boldsymbol{k}} \mathrm{e}^{-i\boldsymbol{k}\boldsymbol{r}} - i\nabla_{\boldsymbol{k}}, \tag{27}$$

which defines the Berry operator (discussed below)

$$\boldsymbol{\beta}_{\boldsymbol{k}} = \mathrm{e}^{i\boldsymbol{k}\boldsymbol{r}} i\nabla_{\boldsymbol{k}} \mathrm{e}^{-i\boldsymbol{k}\boldsymbol{r}}. \tag{28}$$

Both equations are differential operators with respect to $\boldsymbol{k}$ for all terms which are multiplied from the right. The action of $\boldsymbol{\beta}_{\boldsymbol{k}}$ and $\nabla_{\boldsymbol{k}}$ hence must be understood as

$$\boldsymbol{\beta}_{\boldsymbol{k}}|\Phi^{\boldsymbol{k}}\rangle = |\boldsymbol{\beta}_{\boldsymbol{k}}\Phi^{\boldsymbol{k}}\rangle + |\Phi^{\boldsymbol{k}}\rangle i\nabla_{\boldsymbol{k}}, \tag{29a}$$

$$i\nabla_{\boldsymbol{k}}|\Phi^{\boldsymbol{k}}\rangle = |i\nabla_{\boldsymbol{k}}\Phi^{\boldsymbol{k}}\rangle + |\Phi^{\boldsymbol{k}}\rangle i\nabla_{\boldsymbol{k}} \tag{29b}$$

(using the chain rule), where $|\boldsymbol{\beta}_{\boldsymbol{k}}\Phi^{\boldsymbol{k}}\rangle$ is the isolated action of $\boldsymbol{\beta}_{\boldsymbol{k}}$ on $\Phi^{\boldsymbol{k}}$.

Matrix elements of $\boldsymbol{r}$ between Bloch functions (i.e., Bloch sums or linear combinations thereof) can be written as

$$\langle\Phi^{\boldsymbol{q}}|\boldsymbol{r}|\Phi^{\boldsymbol{k}}\rangle = \langle\Phi^{\boldsymbol{q}}|\boldsymbol{\beta}_{\boldsymbol{k}}|\Phi^{\boldsymbol{k}}\rangle - \langle\Phi^{\boldsymbol{q}}|i\nabla_{\boldsymbol{k}}|\Phi^{\boldsymbol{k}}\rangle, \tag{30a}$$

$$\langle\Phi^{\boldsymbol{q}}|\boldsymbol{r}|\Phi^{\boldsymbol{k}}\rangle = \langle\Phi^{\boldsymbol{q}}|\boldsymbol{\beta}_{\boldsymbol{k}}\Phi^{\boldsymbol{k}}\rangle - \big(i\nabla_{\boldsymbol{k}}S_{\Phi}^{\boldsymbol{q}\boldsymbol{k}}\big), \tag{30b}$$

where in Eq. (30a) the differentiations are not confined in both terms, while in Eq. (30b) the differentiation is confined, i.e., these are normal matrices. The unusual shape of Eq. (30b) is formally correct in that it transforms properly under basis changes such that with $\Psi^{\boldsymbol{k}} = \Phi^{\boldsymbol{k}}C^{\boldsymbol{k}}$ one gets

$$\langle\Psi^{\boldsymbol{q}}|\boldsymbol{r}|\Psi^{\boldsymbol{k}}\rangle = \langle\Psi^{\boldsymbol{q}}|\boldsymbol{\beta}_{\boldsymbol{k}}\Psi^{\boldsymbol{k}}\rangle - \big(i\nabla_{\boldsymbol{k}}S_{\Psi}^{\boldsymbol{q}\boldsymbol{k}}\big) \tag{31}$$

by bracketing Eq. (30b) with $C^{\boldsymbol{k}}$ from both sides and applying the chain rule Eq. (29) to both terms on the rhs. At this stage, it is vital to always consider the full nondiagonal form. Note that the last term of Eq. (30b) reduces to $(i\nabla_{\boldsymbol{k}}\delta_{\boldsymbol{q},\boldsymbol{k}})$ for orthonormal $\Phi^{\boldsymbol{k}}$, which is basis independent. (For correct transformation behavior the overlap matrix has to be kept until the end result, however.) Hence, *the essential part of the position operator is the Berry connection matrix* discussed in the following.

B. Berry connection

Using the Berry operator defined above it can be shown [Appendix B 3, Eq. (B29)] that $|\boldsymbol{\beta}_k \Phi^k\rangle$ fulfills the Bloch theorem and hence $\langle \Phi^q | \boldsymbol{\beta}_k \Phi^k\rangle$ is diagonal in $\boldsymbol{k}$. Each Bloch function can be written as $\Phi^k = \mathrm{e}^{i\boldsymbol{kr}} u^k_\Phi$ which leads to

$$\langle \Phi^q | \boldsymbol{\beta}_k \Phi^k\rangle = \delta_{qk} \big\langle u^k_\Phi \big| i\nabla_k u^k_\Phi \big\rangle, \tag{32}$$

which contains the matrix underlying the Berry connection

$$\boldsymbol{A}^k_\Phi = \big\langle u^k_\Phi \big| i\nabla_k u^k_\Phi \big\rangle. \tag{33}$$

Consequently, the position operator matrix elements in a Bloch basis consist of a $\boldsymbol{k}$-diagonal well defined part, the Berry connection matrix, and the gradient of the overlap matrix (delta function for orthonormal bases) (which also contains diagonal elements, implicitly) and this is true in all bases.

An illustrative example of the meaning of Eq. (31) is to formally calculate the dipole integral $\boldsymbol{D} = \int \boldsymbol{r} n(\boldsymbol{r}) d^3 r$ of the density $n(\boldsymbol{r}) = \sum_{kn} f_{kn} |\Psi^k_n|^2$, which using Eq. (31) becomes

$$\boldsymbol{D} = \sum_{kn} f_{kn} \big[\boldsymbol{A}^k_{\Psi,nn} - \lim_{q \to k} (i\nabla_k \delta_{qk}) \big] \tag{34}$$

of which the first term, the essential part of $\boldsymbol{r}$, is the polarization $\boldsymbol{P}^\lambda$ of Ref. [20] up to constant factors.

The Berry connection matrix is Hermitian if the Bloch basis is orthonormal

$$\boldsymbol{A}^{k+}_\Phi = \boldsymbol{A}^k_\Phi - i\nabla_k S^k_\Phi, \tag{35}$$

e.g., for Wannier functions and Hamiltonian eigenfunctions, which remedies its asymmetric formulation (derived via $i\nabla_k S^k = i\nabla_k \langle \Phi^k | \Phi^k\rangle = i\nabla_k \langle \mathrm{e}^{-i\boldsymbol{kr}} \Phi^k | \mathrm{e}^{-i\boldsymbol{kr}} \Phi^k\rangle$).

The basis change $\Psi^k = \Phi^k C^k$ of the $\boldsymbol{k}$-diagonal Berry connection matrix in Eq. (31) reads explicitly

$$\boldsymbol{A}^k_\Psi = C^{k+} \boldsymbol{A}^k_\Phi C^k + C^{k+} S^k_\Phi i\nabla_k C^k. \tag{36}$$

If one interprets Φ as the Bloch sums of local orbitals or Wannier functions and Ψ as the eigenfunctions of the Hamiltonian, the Berry connection consists of a term $C^+ \boldsymbol{A}_\Phi C$, where $\boldsymbol{A}_\Phi$ shall be called *basis connection*, and the usual gradient-of-coefficients term (with an overlap matrix for the nonorthonormal case). The latter term is always available while the former is not known in most situations involving tight binding models. Below, a proper approximation for the basis-connection will be introduced. Practically, Eq. (36) is not useful due to the random phase issue in $\nabla_k C^k$. It will be useful in deriving corrections to the Berry curvature later on.

For a plane wave basis $\Psi^k = \sum_G \mathrm{e}^{i(\boldsymbol{k}+\boldsymbol{G})\boldsymbol{r}} C_{k+G}$, the basis functions are the exponentials and the basis connection matrix is zero:

$$\boldsymbol{A}^k_{G'G} = \langle \mathrm{e}^{i\boldsymbol{G}'\boldsymbol{r}} | i\nabla_k \mathrm{e}^{i\boldsymbol{G}\boldsymbol{r}}\rangle = 0. \tag{37}$$

For a local basis, we introduce vector valued functions

$$(\boldsymbol{r}\Phi)_{\boldsymbol{R}s} = (\boldsymbol{r} - \boldsymbol{R} - \boldsymbol{s}) \Phi_s(\boldsymbol{r} - \boldsymbol{R} - \boldsymbol{s}) \tag{38}$$

with Bloch sums

$$(\boldsymbol{r}\Phi)^k_s = \frac{1}{\sqrt{N}} \sum_{\boldsymbol{R}} \mathrm{e}^{i\boldsymbol{k}(\boldsymbol{R}+\lambda \boldsymbol{s})} (\boldsymbol{r}\Phi)_{\boldsymbol{R}s}, \tag{39}$$

which leads to ($\bar{\lambda} = 1 - \lambda$)

$$\big(\boldsymbol{\beta}_k \Phi^k_s\big) = (\boldsymbol{r}\Phi)^k_s + \bar{\lambda} \Phi^k_s \boldsymbol{s} \tag{40}$$

and the basis connection

$$\begin{aligned} \boldsymbol{A}^k_{\Phi,s's} &= \big\langle \Phi^k_{s'} \big| \boldsymbol{\beta}_k \Phi^k_s \big\rangle \\ &= \big\langle \Phi^k_{s'} \big| (\boldsymbol{r}\Phi)^k_s \big\rangle + \bar{\lambda} S^k_{s's} \boldsymbol{s}. \end{aligned} \tag{41}$$

The λ term is zero for the relative gauge, but nonzero for the periodic gauge of the Bloch sums. The first term on the right-hand side (rhs), which shall be called *reduced position operator*, can be straightforwardly evaluated as

$$\big\langle \Phi^k_{s'} \big| (\boldsymbol{r}\Phi)^k_s \big\rangle = \sum_{\boldsymbol{R}} \mathrm{e}^{i\boldsymbol{k}(\boldsymbol{R}+\lambda(\boldsymbol{s}-\boldsymbol{s}'))} \langle \Phi_{\boldsymbol{0}s'} | (\boldsymbol{r}\Phi)_{\boldsymbol{R}s}\rangle \tag{42}$$

from local orbital matrix elements, which are translation invariant:

$$\langle \Phi_{\boldsymbol{R}'s'} | (\boldsymbol{r}\Phi)_{\boldsymbol{R}s}\rangle = \langle \Phi_{\boldsymbol{0}s'} | (\boldsymbol{r}\Phi)_{\boldsymbol{R}-\boldsymbol{R}',s}\rangle \tag{43}$$

and Hermitian if Φ is orthonormal.

Equation (43) is very useful due to its invariance, which makes them transferable on a lattice. It is the ideal form to store position operator matrix elements (also for the Wannier functions).

The relation to the position operator follows by expanding the $\boldsymbol{r} - \boldsymbol{R} - \boldsymbol{s}$ part of Eq. (38) in Eq. (41), using

$$i\nabla_k S^k_{s's} = -\sum_{\boldsymbol{R}} \mathrm{e}^{i\boldsymbol{k}(\boldsymbol{R}+\lambda(\boldsymbol{s}-\boldsymbol{s}'))} S_{\boldsymbol{0}s',\boldsymbol{R}s} (\boldsymbol{R} + \lambda(\boldsymbol{s} - \boldsymbol{s}'))$$

and reads

$$\boldsymbol{A}^k_{\Phi,s's} = \frac{1}{N} \sum_{\boldsymbol{R}} \mathrm{e}^{i\boldsymbol{k}(\boldsymbol{R}+\lambda(\boldsymbol{s}-\boldsymbol{s}'))} \langle \Phi_{\boldsymbol{0}s'} | \boldsymbol{r} | \Phi_{\boldsymbol{R}s}\rangle + (i\nabla_k - \lambda \boldsymbol{s}') S^k_{s's}. \tag{44}$$

In the periodic gauge $\lambda = 0$ and for WFs $S^k_{s's} = \delta_{s's}$, this is the expression usually given. However, Eq. (41) is the simpler and arguably the more natural choice.

In order to calculate the basis connection (41) for the Wannier functions, one needs to express the reduced position operator matrix (42) of the WFs in terms of the basis orbitals. Note that in our implementation the relative gauge $\lambda = 1$ is used and hence the last term in Eq. (41) is zero and basis-connection and reduced position operator matrix are identical.

Our Wannier functions are related to the LOs via Eq. (18). The Berry connection in the Wannier basis hence is obtained by a basis change Eq. (36) when letting $\Psi \to w$ and $C \to a$:

$$\boldsymbol{A}^k_w = a^{k+} \boldsymbol{A}^k_\Phi a^k + a^{k+} S^k_\Phi i\nabla_k a^k. \tag{45}$$

The first term on the rhs is given by Eq. (41) with Φ being our LOs, while the gradient needs special treatment. It turned out that a direct calculation via the real-space coefficients $a_{\boldsymbol{0}c',\boldsymbol{R}c}$ is not very accurate. Instead we use a numerical differentiation technique akin to the one described in Ref. [2]. Finally, $\boldsymbol{A}^k_w$ is Fourier back transformed which gives $\langle w_{\boldsymbol{0}c'} | (\boldsymbol{r}w)_{\boldsymbol{R},c}\rangle$ in real space which is stored together with the other WF information for post processing. From this the Wannier basis connection $\boldsymbol{A}^k_w$ can be retrieved via Eqs. (41) and (42) with $\Phi \to w$, $S_{s's} \to \delta_{s's}$ in either Bloch sum gauge.

The reduced position operator matrix elements Eq. (43), especially for orthonormal bases, are quite intuitive. The on-site elements are the integral of two orbitals multiplied with the position vector from the orbital origin. For two equal orbitals, which are eigenfunctions of inversion, this integral is always zero due to parity. For other cases and also for the off-site case one can argue that the orthonormality of the orbitals/WFs will somewhat transfer to these matrix element to make them rather small.

Also the reduced elements are Hermitian (for orthonormal bases) and transform according to all symmetries (see Appendix B 4). Hence, they are a reasonable choice to be considered as the physically important matrix. By approximating it by zero, we get

$$\boldsymbol{A}^{\boldsymbol{k}}_{w,s's} \approx \bar{\lambda}\delta_{s's}\boldsymbol{s} \tag{46}$$

for orthonormal bases. Note that this is nonzero in the periodic gauge, in which the Bloch sums are $\boldsymbol{k}$-periodic.

The basis connection can only be zero in one gauge, which forces a choice which matrix to put to zero. We argue that the relative gauge, which is usually not mentioned in the context of Wannier functions is the one in which the WF basis connection can be neglected. We will show numerical evidence for this later. This might be important in tight-binding models, where the basis is not explicitly known and hence the basis connection is missing. Furthermore, approximation Eq. (46) is needed to preserve symmetry properties (Appendix B 4), which further indicates the correctness of this choice.

C. Berry curvature

In this section, we derive the Berry curvature matrix

$$\boldsymbol{F}^{\boldsymbol{k}}_{\Psi} = \nabla_{\boldsymbol{k}} \times \boldsymbol{A}^{\boldsymbol{k}}_{\Psi} \tag{47}$$

in the eigenstate representation. Starting from the (Wannier) basis connection $\boldsymbol{A}^{\boldsymbol{k}}_{w} = \langle w^{\boldsymbol{k}} | \boldsymbol{\beta}_{\boldsymbol{k}} w^{\boldsymbol{k}} \rangle$ (usually reassembled from the reduced position operator in WF basis during post processing) we make a basis change $\Psi^{\boldsymbol{k}} = w^{\boldsymbol{k}} C^{\boldsymbol{k}}$ using Eq. (36) with $\Phi \to w$

$$\boldsymbol{A}^{\boldsymbol{k}}_{\Psi} = C^{\boldsymbol{k}+}\boldsymbol{A}^{\boldsymbol{k}}_{w}C^{\boldsymbol{k}} + C^{\boldsymbol{k}+}S^{\boldsymbol{k}}_{w} i\nabla_{\boldsymbol{k}}C^{\boldsymbol{k}} \tag{48}$$

where the overlap matrix is the unit matrix for orthonormal WFs. Let's introduce some short hands

$$\langle \boldsymbol{A} \rangle_{C} = C^{\boldsymbol{k}+}\boldsymbol{A}^{\boldsymbol{k}}_{w}C^{\boldsymbol{k}}, \tag{49}$$

$$\langle Si\nabla \rangle_{C} = C^{\boldsymbol{k}+}S^{\boldsymbol{k}}_{w} i\nabla_{\boldsymbol{k}}C^{\boldsymbol{k}}, \tag{50}$$

$$\langle \boldsymbol{f} \rangle_{C} = C^{\boldsymbol{k}+}\big(\nabla_{\boldsymbol{k}} \times \boldsymbol{A}^{\boldsymbol{k}}_{w}\big)C^{\boldsymbol{k}}. \tag{51}$$

Differentiation of the normalization $C^{\boldsymbol{k}+}S^{\boldsymbol{k}}_{w}C^{\boldsymbol{k}} = \mathbf{1}$ gives

$$\langle Si\nabla \rangle^{+}_{C} = \langle Si\nabla \rangle_{C} + C^{\boldsymbol{k}+}\big(i\nabla_{\boldsymbol{k}}S^{\boldsymbol{k}}_{w}\big)C^{\boldsymbol{k}} \tag{52}$$

and Eq. (35) gives

$$\langle \boldsymbol{A} \rangle^{+}_{C} = \langle \boldsymbol{A} \rangle_{C} - C^{\boldsymbol{k}+}\big(i\nabla_{\boldsymbol{k}}S^{\boldsymbol{k}}_{w}\big)C^{\boldsymbol{k}}. \tag{53}$$

Then using $\nabla \times u\boldsymbol{v}w = (\nabla u) \times \boldsymbol{v}w + u(\nabla \times \boldsymbol{v})w - u\boldsymbol{v} \times (\nabla w)$, where u, w are matrices and $\boldsymbol{v}$ is a vector of matrices, and the identity $C^{\boldsymbol{k}}C^{\boldsymbol{k}+}S^{\boldsymbol{k}}_{w} = \mathbf{1}$ and commuting nonvector matrices through the × symbol one gets

$$\boldsymbol{A}^{\boldsymbol{k}}_{\Psi} = \langle \boldsymbol{A} \rangle_{C} + \langle Si\nabla \rangle_{C}, \tag{54a}$$

$$\boldsymbol{F}^{\boldsymbol{k}}_{\Psi} = \langle \boldsymbol{f} \rangle_{C} - i\langle \boldsymbol{A} \rangle^{+}_{C} \times \langle \boldsymbol{A} \rangle_{C} + i\boldsymbol{A}^{\boldsymbol{k}+}_{\Psi} \times \boldsymbol{A}^{\boldsymbol{k}}_{\Psi} \tag{54b}$$

$$\begin{aligned} &= \langle \boldsymbol{f} \rangle_{C} + i\langle \boldsymbol{A} \rangle^{+}_{C} \times \langle Si\nabla \rangle_{C} + i\langle Si\nabla \rangle^{+}_{C} \times \langle \boldsymbol{A} \rangle_{C} \\ &\quad + i\langle Si\nabla \rangle^{+}_{C} \times \langle Si\nabla \rangle_{C}. \end{aligned} \tag{54c}$$

Note that the cross product expressions are matrix products at the same time ($(\boldsymbol{a} \times \boldsymbol{b})_{nm,k} = \sum_{lij} \varepsilon_{ijk}\boldsymbol{a}_{nl,i}\boldsymbol{b}_{lm,j}$). The second term grouping of $\boldsymbol{F}^{\boldsymbol{k}}_{\Psi}$ corresponds to the result of Ref. [21] while the first emphasizes the symmetry between the curvature in both bases and is discussed in the Appendix of Ref. [21].

Due to Eq. (35) $\boldsymbol{A}^{\boldsymbol{k}}_{\Psi}$ is Hermitian, since $\Psi^{\boldsymbol{k}}$ is orthonormal, and the basis curvature $\boldsymbol{f}^{\boldsymbol{k}} = \nabla \times \boldsymbol{A}^{\boldsymbol{k}}_{w}$ is Hermitian since $S^{\boldsymbol{k}}_{w}$ is smooth and $\nabla \times \nabla S = 0$. This makes $\langle \boldsymbol{f} \rangle_{C}$ and hence also $\boldsymbol{F}^{\boldsymbol{k}}_{\Psi}$ Hermitian. Equations (54) are true for any basis $w^{\boldsymbol{k}}$ and hence could also be used directly in the nonorthogonal FPLO basis. [If additionally $\Psi^{\boldsymbol{k}}$ were to be nonorthonormal $(S_{\Psi})^{-1}$ needs to be inserted before or after all × symbols in Eq. (54).]

In practice, $\langle Si\nabla \rangle_{C}$ is obtained in the parallel transport gauge [21], which is not a periodic gauge and hence makes Eq. (54a) useless for topological applications but it allows to calculate Eq. (54b). In detail, nondegenerate perturbation theory of first order gives

$$\langle Si\nabla \rangle_{C,mn} = i\frac{C^{\boldsymbol{k}+}_{m}\big(\nabla_{\boldsymbol{k}}H^{\boldsymbol{k}}_{w}\big)C^{\boldsymbol{k}}_{n} - C^{\boldsymbol{k}+}_{m}\big(\nabla_{\boldsymbol{k}}S^{\boldsymbol{k}}_{w}\big)C^{\boldsymbol{k}}_{n}\varepsilon^{\boldsymbol{k}}_{n}}{\varepsilon^{\boldsymbol{k}}_{n} - \varepsilon^{\boldsymbol{k}}_{m}}(1 - \delta_{mn}), \tag{55}$$

where the gradient of the Hamiltonian in Wannier basis reads

$$\begin{aligned} \nabla_{\boldsymbol{k}}H^{\boldsymbol{k}}_{w} = i\sum_{\boldsymbol{R}} &\mathrm{e}^{i\boldsymbol{k}(\boldsymbol{R}+\lambda(\boldsymbol{s}-\boldsymbol{s}'))}(\boldsymbol{R} + \lambda(\boldsymbol{s} - \boldsymbol{s}')) \\ &\times \langle w_{\mathbf{0}\boldsymbol{s}'} | \hat{H} | w_{\boldsymbol{R}\boldsymbol{s}} \rangle. \end{aligned} \tag{56}$$

For an orthonormal basis, the gradient of the overlap vanishes. The basis curvature $\boldsymbol{f}^{\boldsymbol{k}}$ is obtained by directly taking the curl of the exponential in Eq. (42) ($\Phi \to w$) and inserting into Eq. (41). (The curl of the overlap can be obtained in a similar way for nonorthonormal bases.)

We need to discuss the non Abelian (degenerate) case, in which the Berry curvature matrix obtains a covariant correction in each degenerate subspace [22]. If P_i denotes the projector onto the ith subspace (degenerate or not), one needs to write

$$P_i\boldsymbol{F}^{\boldsymbol{k}}_{\Psi nA}P_i = P_i\big(\boldsymbol{F}^{\boldsymbol{k}}_{\Psi} - i\boldsymbol{A}^{\boldsymbol{k}}_{\Psi}P_i \times P_i\boldsymbol{A}^{\boldsymbol{k}}_{\Psi}\big)P_i \tag{57}$$

for each subspace. For a nondegenerate subspace, $\boldsymbol{A}^{\boldsymbol{k}}_{\Psi,ii} = P_i\boldsymbol{A}^{\boldsymbol{k}}_{\Psi}P_i$ is a single vector-valued matrix element and hence $\boldsymbol{A}^{\boldsymbol{k}}_{\Psi,ii} \times \boldsymbol{A}^{\boldsymbol{k}}_{\Psi,ii} = 0$ and the correction is zero. In a degenerate subspace, only the average of the trace is physically meaningful. In the case of an orthonormal basis, this allows to introduce a unitary transformation, which ultimately leads to $i\mathrm{Tr}P_i\langle \boldsymbol{A} \rangle_{C}P_i \times P_i\langle \boldsymbol{A} \rangle_{C}P_i = 0$ and permits to discard such block diagonal terms (if only degenerate subspace averages are considered). Inserting Eq. (54b) into Eq. (57) and introducing

$Q_i = 1 - P_i$, one gets for orthonormal bases

$$\begin{aligned} P_i \boldsymbol{F}^{\boldsymbol{k}}_{\Psi nA} P_i = P_i\big(&\langle \boldsymbol{f}\rangle_C - i\langle \boldsymbol{A}\rangle_C Q_i \times Q_i \langle \boldsymbol{A}\rangle_C \\ &+ i\boldsymbol{A}^{\boldsymbol{k}}_{\Psi} Q_i \times Q_i \boldsymbol{A}^{\boldsymbol{k}}_{\Psi}\big)P_i. \end{aligned} \tag{58}$$

This expression contains $\langle Si\nabla\rangle$ bracketed between Q_i and P_i and hence only matrix elements between different subspaces such that the energy denominator in Eq. (55) is never zero. This solves the division by zero issue. In essence, the non-Abelian Berry curvature is obtained from Eqs. (54b) and (54c) by removing the diagonal blocks of all subspaces from $\langle \boldsymbol{A}\rangle_C$ and $\langle Si\nabla\rangle_C$.

Reference [21] discusses the terms of $F^{\boldsymbol{k}}$ and argues that the $\langle Si\nabla\rangle \times \langle Si\nabla\rangle$ term of Eqs. (54c) is by far the leading term. This would allow to ignore the basis connection/curvature terms, especially if they are not obtainable. However, this is not necessarily correct. In Appendix B 4, it is shown that the term $\langle Si\nabla\rangle \times \langle Si\nabla\rangle$ does not transform properly under symmetry in the periodic gauge. However, if $\boldsymbol{A}^{\boldsymbol{k}}_{w}$ is approximated by Eq. (46) in Eqs. (49) and (54a) proper symmetry transformation is restored. This shows that the term grouping Eqs. (54b) and (58) is to be preferred and in fact under the approximation the only term left is $iP\boldsymbol{A}^{\mathrm{appr}}_{\Psi} Q \times Q\boldsymbol{A}^{\mathrm{appr}}_{\Psi} P$ with approximated $\boldsymbol{A}^{\mathrm{appr}}_{\Psi}$, which reduces to the $\langle Si\nabla\rangle$-only term in relative gauge.

Another argument for the grouping Eq. (54b) is the fact that both $iP\boldsymbol{A}_{\Psi} Q \times Q\boldsymbol{A}_{\Psi} P$ and $\langle \boldsymbol{f}\rangle_C - i\langle \boldsymbol{A}\rangle_C Q_i \times Q_i\langle \boldsymbol{A}\rangle_C$ are invariant under symmetry and with respect to the Bloch sum gauge choice controlled by λ (see Appendix B 5) while the other grouping is not, especially not the approximation of only taking the $\langle Si\nabla\rangle \times \langle Si\nabla\rangle$ term. Finally, if the Ψ basis is complete $\langle \boldsymbol{f}\rangle_C - i\langle \boldsymbol{A}\rangle_C Q_i \times Q_i\langle \boldsymbol{A}\rangle_C$ will go to zero and $\boldsymbol{F}^{\boldsymbol{k}}_{\Psi nA} = iP\boldsymbol{A}_{\Psi} Q \times Q\boldsymbol{A}_{\Psi} P$ is the complete Berry curvature.

In FPLO before version 19, only the periodic gauge was implemented; now both gauges as well as the full basis connection are available. Furthermore, for historical reasons the FPLO implementation contains an overall minus sign for the Berry connection/curvature as if we defined $\boldsymbol{A}^{\boldsymbol{k}} = \langle u^{\boldsymbol{k}}| - i\nabla_{\boldsymbol{k}} u^{\boldsymbol{k}}\rangle$ instead of Eq. (33). Taking this sign into account we are consistent with the data presented in Ref. [21].

On a final note, in cases of TB models for which no explicit WFs but the nature/symmetry of these functions are known, instead of approximation Eq. (46) one could derive parametrized analytic expressions for leading matrix elements in Eq. (43) based on the nature of the WFs which inserted into Eq. (41) give a reasonable approximation for the basis connections.

IV. FEATURES OF MAXIMALLY PROJECTED WANNIER FUNCTIONS

The examples shown here are not discussed in terms of their DFT setup. More details can be found in Appendix C.

A. Work flow

The WF creation is controlled by the choice of projectors ϕ, the energy window, which can be chosen individually for each projector (although most of the time a global window is used) and the real space cutoff ρ and a coefficient threshold (to save space), below which WF data are discarded. The latter might need to be changed from its default if the targeted bands are very flat.

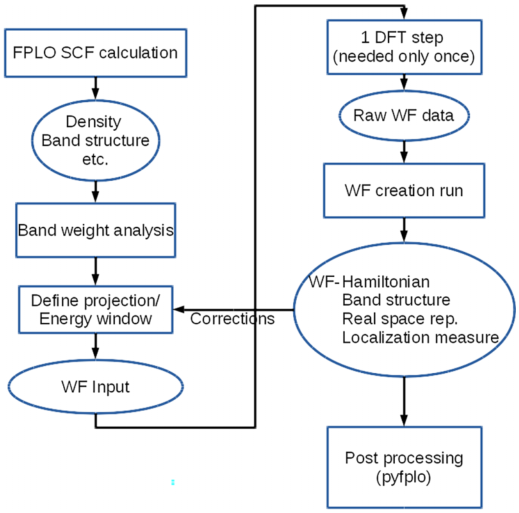

FIG. 1. The work flow to construct and use SCMPWFs in the FPLO implementation.

The projectors can be single FPLO orbitals, for which only a site number, an orbital descriptor and optionally local quantization axes need to be defined. In full relativistic mode, the projectors can be in four-spinor quantum numbers $nlj\mu$ or in pseudo-non-relativistic qns. $nlm\sigma$, in which case separate local spin axes can be defined. Also unnormalized linear combinations of LOs (MOs) can be chosen as projectors, which are defined by picking an imagined Wannier center, from which difference vectors to the contributing sites must be defined. Furthermore, for each contribution a site number, a weight and local axes must be specified. The main constraint is that the set of projectors must be closed under all symmetry operations. Band disentangling and the quality of the fit is controlled by proper choice of projectors and energy window.

Alternatively, there is an automatic mode, which picks either all FPLO orbitals as projectors or only the subset which does not clearly form semicore states. The FPLO basis is relatively small with of 15 to 35 orbitals per atoms for most of the periodic table, which avoids a too large resulting WF basis. Removal of semicore states further decreases the basis size. The advantage of this mode is application in automated calculations and the fact that no energy window needs to be defined. The cutoff ρ however might need to be increased (preferably to it is maximum) due to the larger extent of higher energy WFs.

To construct WFs with FPLO a WF input file needs to be created, which can be done by hand or with the help of a PYTHON module, which allows to efficiently create single-orbital projectors for any set of sites/orbitals as well as molecular orbital projectors. Starting from a converged calculation and with the input file present an FPLO run will produce a file with all the data needed to construct the Wannier functions in a second run (see Fig. 1). At this stage, the real space Wannier representation, the symmetry operations and all demanded operators [like reduced position operator, full relativistic spin operators $\beta\vec{\Sigma}$ and the exchange-correlation (xc) magnetic field] are written to a separate file for post

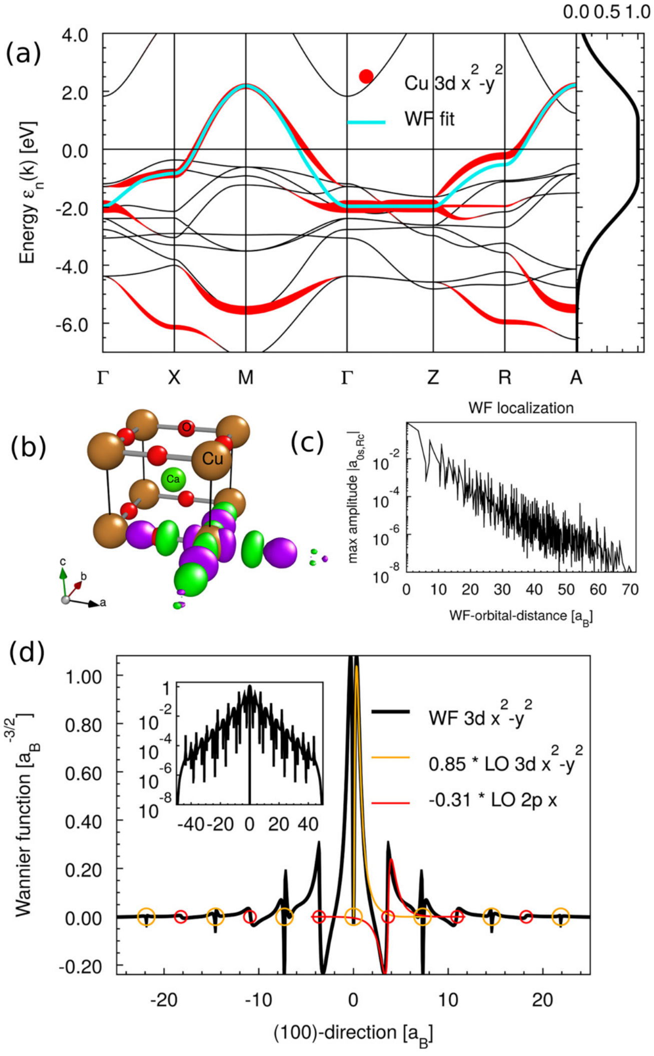

FIG. 2. (a) Band structure (black) of CaCuO$_2$, the FPLO orbital $3d_{x^2-y^2}$ band character (red) and the single band Wannier fit (cyan). (b) Unit cell containing the Wannier function at isovalue 0.04. (c) Maximum of orbital contributions to the WF in logarithmic scale as a function of WF-orbital distance. (d) WF printed along the (100) axis through the WF center (black), the Cu $3d_{x^2-y^2}$ (orange), and the O $2p_x$ (red) orbitals scaled according to their amplitude. The inset shows $|w|$ along the same path in logarithmic scale.

processing. Additionally, WF output on a real space grid for visualization purposes can be requested.

B. Model extraction

The first example demonstrates the construction of a single band model of the anti-bonding (AB) Cu $3d_{x^2-y^2}$ band for the infinite layer cuprate CaCuO$_2$. The band structure (Fig. 2) contains the prototypical AB band in the energy interval $[-2, 2]$ eV around the Fermi level highlighted by the FPLO-orbital band character. The bonding part below -3 eV, which is more diffuse, is of course also present.

The input (essentially a site number and an orbital name) for the wannierization contains a single projector consisting of the $3d_{x^2-y^2}$ orbital sitting at the Cu site. The $\boldsymbol{k}$ mesh has 12^3 points. The core energy window is chosen as $[-1, 1]$ eV with symmetrical Gaussian tails, Eq. (26), of width $\Delta = 2$ eV as indicated on the right side of the band structure. This window is considerably overlapping with the bonding part, yet the resulting WF (cyan) follows the antibonding part, where $h^{\boldsymbol{k}}$ is dominant. The fit is not perfect, owed to the fact that there are lots of hybridizations interrupting the unbroken flow of the band character. It however samples the essence of the targeted band. The WF fit was calculated from WF data with a real space cutoff $\rho = 25a_{\mathrm{B}}$. To illustrate the exponential localization of the WF the maximum of the amplitudes $\max(|a_{\boldsymbol{Rs},\boldsymbol{0c}}|)$ of contributing orbitals around the WF, Eq. (24), as a function of WF-orbital distance are shown in Fig. 2(c) for a cutoff $\rho = 70a_{\mathrm{B}}$. Note, the logarithmic scale.

Figure 2(b) shows the crystal structure and the WF, which clearly has $x^2 - y^2$ symmetry and sizable oxygen hybridization tails as to be expected for this case. The WF along the (100) direction through the WF center is plotted in Fig. 2(d). Additionally, the Cu $3d_{x^2-y^2}$ and O $2p_x$ orbitals scaled according to their amplitude $a_{\boldsymbol{Rs},\boldsymbol{0c}}$ is shown. The circles show the position of the atoms in the same color as the orbitals. This WF is rather extended since it needs to describe a Cu-O hybridized band via a single WF. It is however exponentially localized as indicated by the inset which shows $|w|$ in logarithmic scale. Note that the projector consists only of the Cu $3d_{x^2-y^2}$ orbital (orange), all other contributions to the WF are pulled in due to the projection process.

C. Band disentangling

A more complex example which demonstrates band disentangling is the $3d$-only WFs for spin polarized fully relativistic bcc iron (see Appendix C 2). Spin is no longer a good qn. although spin orbit coupling and hence spin-mixing is quite small. The complication is the hybridization with the $4sp$ bands, which have a band width of several tens of electron volts, which means that bands which start as d bands at some $\boldsymbol{k}$ point can mutate into free electron bands away from the point. Hence, the predominantly $3d$-character Hilbert space is not restricted to a finite energy window and the corresponding WFs cannot follow the d-band structure at all points.

We performed a Wannier fit using $3d$ orbitals with nonrelativistic symmetry as projectors [see Appendix B 1, Eq. (B7)]. These are obtained from a linear combination of the four spinors Eq. (A1), such that the resulting orbital transforms as a real Harmonic (which is an inbuilt option besides projection onto the relativistic four spinors themselves). The energy window as indicated at the right side of Fig. 3(a) has a core region $[-5, 0]$ eV and Gaussian tails of width $\Delta = 7$ eV. We used a $\boldsymbol{k}$ mesh with 16^3 points in the primitive reciprocal cell and a cutoff $\rho = 25a_{\mathrm{B}}$ for the real space representation of the WFs. Although, the energy window is quite large, the resulting Wannier fit (bright green and red) follows the bands with $3d$ character (milky green and red) very closely at most parts of the Brillouin zone (BZ). The WFs also resolve the original spin character.

Figure 3(a) shows three regions marked by numbers. In region 1, the highest minority d band at Γ becomes a free electron band (milky blue) as it progresses towards the H point. At the same time, an sp band enters the d region from below. So, the WFs must reconnect the manifold at Γ to the

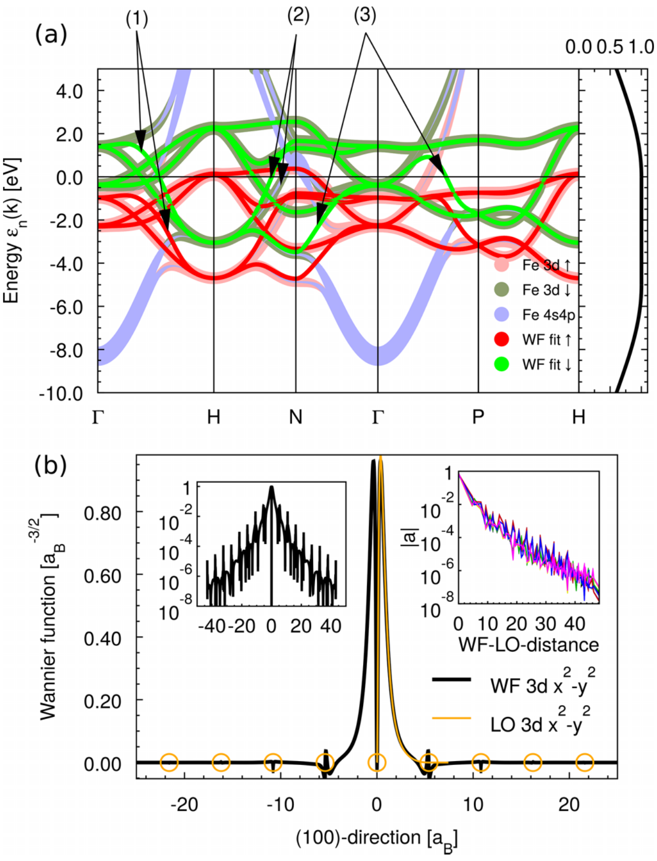

FIG. 3. (a) Band weights of the FPLO calculation in pastel colors and Fe $3d$ WF fit in bright colors (see text). (b) $3d_{x^2-y^2}$ WF printed along the (100) axis through the WF center (black), the Fe $3d_{x^2-y^2}$ local orbital (orange). Left inset shows $|w|$ along the same path in logarithmic scale. Right inset shows the maximal orbital contributions to the WFs in logarithmic scale as a function of WF-LO distance.

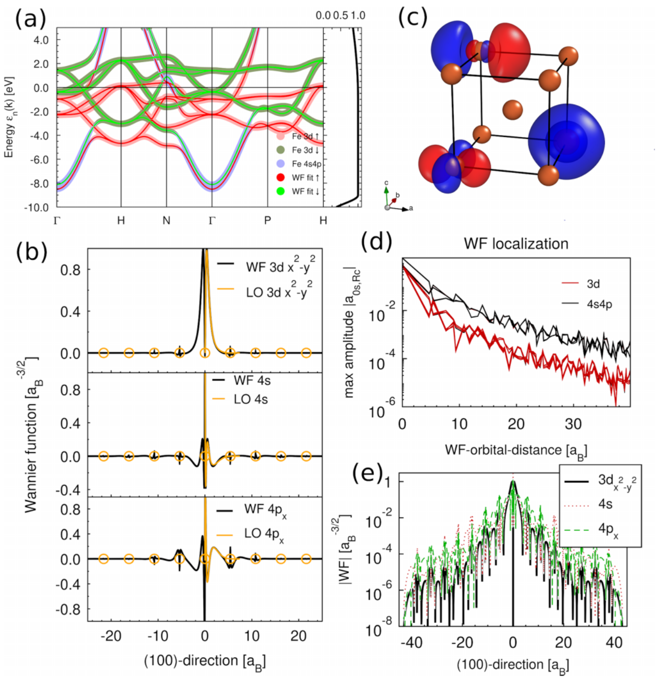

FIG. 4. (a) Band weights of the FPLO calculation in pastel colors and the WF fit in bright colors. (b) (Top down) $3d_{x^2-y^2}$, $4s$ and $4p$ WFs printed along the (100) axis through the WF center (black), the FPLO local orbitals (orange). (c) Corresponding WF isosurfaces for isovalue 0.09. (d) Maximal orbital contributions to the WFs in logarithmic scale as a function of WF-LO distance. (e) $|w|$ along the same path in logarithmic scale.

manifold at H by interpolating through some dispersion not existing in the DFT band structure (the same happens for the majority spin bands).

One of the lowest (degenerate) minority bands (-3 eV) at H bends upwards and turns into an *sp* band at N, as marked by the right arrow in region 2, while the missing *d* character flows in from above 2 eV. At the N point, all *d* weight sits in the two bands at 1–1.5 eV. Consequently, the WF (left arrow) must deviate from the DFT band to smoothly interpolate the pure *d* bands between H and N.

A similar situation as in region 1 occurs in region 3 between the H and Γ points and the Γ and P points, respectively. *d* weight flows to lower energies from N to Γ and to higher energies between Γ and P, which forces the WFs to deviate from the original band structure. Between, P and H the second and forth lowest Wannier bands deviate from the DFT bands by 180 meV (not visible in the fat-band plot). Besides these regions the WF fit follows the original bands rather closely.

Figure 3(b) plots the WF along the (100) direction through the Wannier center (black) together with the $3d_{x^2-y^2}$ orbital (orange). The circles denote the atom positions. There are some notable orthogonalization tails at first and second neighbor, but otherwise the WF and the local orbital are nearly identical. The right inset shows $\max(|a_{\mathbf{Rs},\mathbf{0c}}|)$ [Eq. (24)] as a function of the WF-LO distance and the left inset shows the WF along the same direction as the main panel with logarithmic y axis. Clearly, the expansion coefficients as well as the WF itself are exponentially localized and the localization is similar to that of the *d* orbital.

To get a useful $3d$ WF fit, the $4s4p$ orbitals have to be included, which represents the minimum chemical basis for bcc Fe. The corresponding projectors are all the $4s4p3d$ orbitals sitting at their respective site, i.e., (000). The energy window needs to have a rather large upper Gaussian tail to sample all the needed representations of which especially the "free-electron" states lie at higher energies. The core window is $[-9, -1]$ and the upper tail has $\Delta = 15$ eV (the lower does not matter). A real space cutoff $\rho = 40a_{\mathrm{B}}$ was used. Figure 4(a) shows the resulting WF fit. The DFT results are shown in pastel colors with larger width while on top the WF fit is plotted with a smaller width. The two sets of bands are on top of each other to within 20 meV error. Figure 4(b) shows the WFs along the (100) direction through the origin for the $3d_{x^2-y^2}$, $4s$, and $4p_x$ orbitals together with the corresponding FPLO basis functions (orange and only plotted towards the positive axis). The WFs follow the orbitals very closely within the first neighbor region, while the "free-electron" WFs have sizable hybridization tails which is related to their large band width. Figure 4(c) shows the (suitably translated) isosurfaces of these three functions for isovalue 0.09, while (d) shows the maximum orbital contributions $\max(|a_{\mathbf{Rs},\mathbf{0c}}|)$ to all WFs

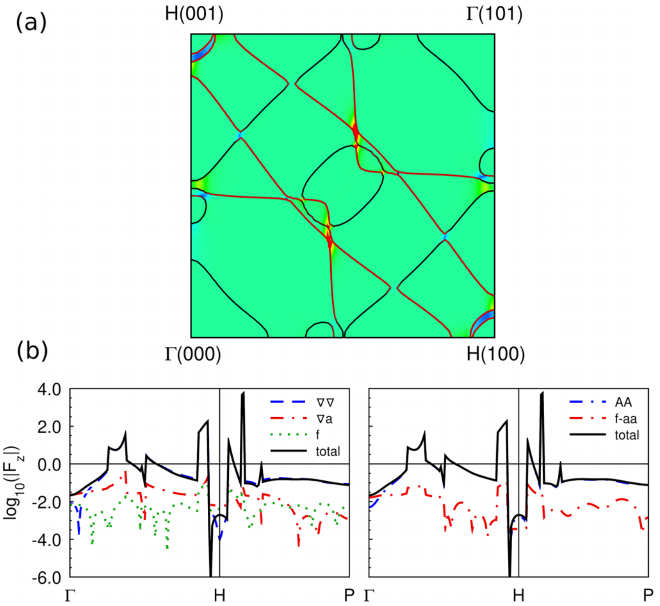

FIG. 5. Berry curvature of spin polarized full relativistic bcc Fe. (a) Thin lines: Fermi surface contour in the $k_y = 0$ plane. Color plot: $-\boldsymbol{F}_z$. (b) The Berry curvature components along the path ΓHP (see text). The left panel shows term-grouping of Ref. [21]: $\nabla\nabla = i\langle Si\nabla\rangle_C \times \langle Si\nabla\rangle_C$, $\nabla a = i\langle Si\nabla\rangle_C \times \langle \boldsymbol{A}\rangle_C + \text{H.c.}$, and $f = \langle \boldsymbol{f}\rangle_C$ The right panel shows our preferred grouping $AA = i\boldsymbol{A}_\Psi \times \boldsymbol{A}_\Psi$ and $f - aa = \langle \boldsymbol{f}\rangle_C - i\langle \boldsymbol{A}\rangle_C \times \langle \boldsymbol{A}\rangle_C$.

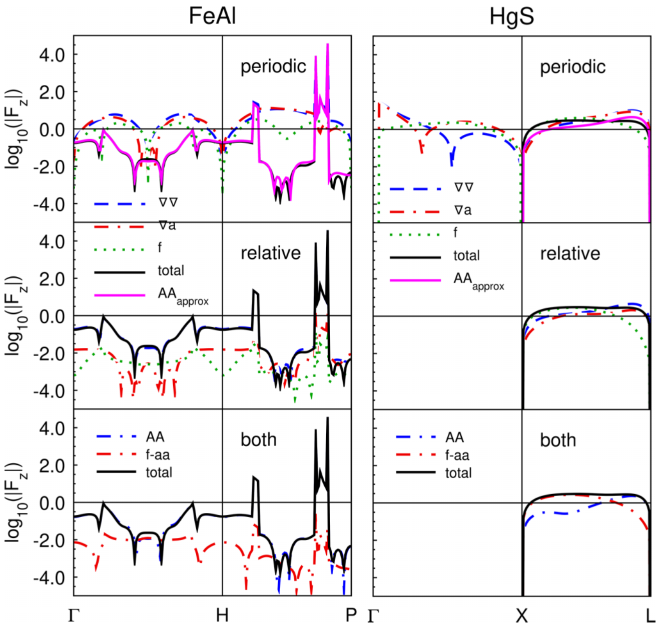

FIG. 6. (Left) Berry curvature of spin polarized full relativistic B2 FeAl. (Right) Berry curvature of non-spin-polarized full relativistic HgS. (Top) Term grouping of Ref. [21] for periodic gauge. (Middle) Term grouping of Ref. [21] for relative gauge. (Bottom) Preferred term grouping. The terms are explained in Fig. 5 except for AA_{approx}, which is the AA term with approximated basis connection.

in logarithmic scale, which shows exponential localization, albeit less localized than the pure Fe-3d fit discussed above. Note that the 3d orbitals are more localized than the rest as is to be expected. Finally Fig. 4(e) shows the absolute value of the WFs from (b) in the logarithmic scale along the same path, which also proves localization.

D. Berry curvature, anomalous Hall conductivity

To compare to Ref. [21] and to illustrate the Berry curvature terms and their grouping we show the results for the Berry curvature of full-relativistic spin-polarized bcc Fe in Fig. 5 (for the 3d4s4p Wannier model of Sec. IV C). By comparing the Fermi surface contour to Ref. [21], it becomes clear that the two band structure codes do not give the exact same result, which is not surprising given that the cited results use a pseudo-potential code and treats the relativistic effects differently from our full four-component treatment. It is likely that our results compare better for slightly different lattice constants. Nevertheless, the Berry curvature plot and the curvature plotted along the Brillouin zone path Γ(000) − H(010) − P($\frac{1}{2}\frac{1}{2}\frac{1}{2}$) compare well. Figure 5(b) shows the two different ways of grouping the terms. The left panel uses the grouping of Ref. [21], which corresponds to Eq. (54c) while the right panel shows the grouping Eq. (54b) (also discussed in the Appendix of Ref. [21]), preferred by us for symmetry, gauge invariance and approximation reasons. In bcc Fe, there is only one site at (000) and hence the gauge dependent corrections are all zero and periodic and relative gauge identical. The term-grouping according to the Ref. [21] shows that the $\langle Si\nabla\rangle \times \langle Si\nabla\rangle$ is indeed the dominant term while $\langle Si\nabla\rangle \times \langle \boldsymbol{A}\rangle_C$ and $\langle f\rangle_C$ are quite small. The approximation Eq. (46) is zero and hence the approximated curvature is the $\langle Si\nabla\rangle \times \langle Si\nabla\rangle$ term itself.

Our preferred term grouping in the right panel shows that $\boldsymbol{A}_\Psi \times \boldsymbol{A}_\Psi$ is even closer to the total result while $\langle f\rangle_C - \langle A\rangle_C \times \langle A\rangle_C$ is rather small.

We also integrated the Berry curvature over the irreducible part of the BZ (with subsequent symmetrization) to obtain anomalous Hall conductivity (AHC). To speed up this quite time consuming calculation we reduced the real space cutoff to $\rho = 25a_{\text{B}}$, which leads to small band energy errors of maximal 200 meV around the N point but yields a smaller Wannier model. For a mesh with 300^3 k points in the total BZ, we obtain 715.4 and 720.5 S/cm for the $\nabla \times \nabla$ only and the full Berry curvature, respectively. For 600^3 k points, this becomes 717.9 and 722.90 S/cm. This is a bit smaller than the 756.8 S/cm reported by Ref. [21], which used a finer adaptive integration. However, their smallest mesh which compares to our largest also deviates by about the same amount, which is most likely due to the method/band structure differences discusses above.

To further assess the validity of the general arguments of Sec. III A in favor of our preferred term grouping we show the Berry curvature results for two more cases. The left panel of Fig. 6 shows the Berry curvature along a BZ path for spin-polarized full-relativistic B2 FeAl, which is obtained from bcc Fe by replacing the iron at the unit cell center by Al (see Appendix C 3), while the right panel shows $\boldsymbol{F}$ for non-spin-polarized full-relativistic HgS along the same path (different high symmetry point names). The top and middle rows show the results for the term-grouping of Ref. [21]

in the periodic and relative gauge, respectively, while the bottom row shows the preferred term-grouping which is independent of the Bloch sum gauge. Additionally, in the top row the $\boldsymbol{A}_{\Psi}^{\text{appr}} \times \boldsymbol{A}_{\Psi}^{\text{appr}}$ term is shown within the approximation Eq. (46), which is distinct in the periodic gauge and equivalent to the $\langle Si\nabla\rangle_C \times \langle Si\nabla\rangle_C$ term in relative gauge.

Clearly, for FeAl in the periodic gauge, the individual terms in the Ref. [21] grouping are larger than the total which demonstrates the necessity of including the basis connection terms. Interestingly, the approximated $\boldsymbol{A}_{\Psi}^{\text{appr}} \times \boldsymbol{A}_{\Psi}^{\text{appr}}$ term in periodic gauge (which equals the $\nabla \times \nabla$ term in relative gauge) is quite close to the total. The preferred grouping shows as for bcc Fe that the $\boldsymbol{A}_{\Psi} \times \boldsymbol{A}_{\Psi}$ term is largely dominant.

For HgS, the situation is less satisfactory. We first note that all individual terms in the Ref. [21] grouping in periodic gauge (top right panel) are nonzero along $\Gamma - \text{X}$, although the total as well as the approximated $\boldsymbol{A}_{\Psi}^{\text{appr}} \times \boldsymbol{A}_{\Psi}^{\text{appr}}$ term are zero due to symmetry (non-spin-polarized). In the relative gauge (middle right panel) as well as in the preferred grouping (bottom right panel), the symmetry is preserved, which confirms the general arguments of Sec. III A. On the line X-L neither term grouping has a dominant term.

E. Molecular orbital projectors

Up to now, we always projected onto single orbitals, which creates WFs which look like these orbitals in the Fe case or which acquire sizable hybridization tails for CaCuO_2. Especially in cases of isolated band complexes (and if these complexes are Wannier representable) bond centered WFs might be needed. To illustrate this we perform a Wannier fit for MgB_2, which has alternating triangular Mg and hexagonal boron layers. The occupied band structure consists of 3 boron-$2s2p_{x,y}$ bands, which can be described by sp^2 hybrids and one mostly decoupled boron-$2p_z$ band. We will construct a Wannier model of the occupied sp^2 hybrids.

Figure 7(d) shows the two boron sites in the boron plane of the unit cell viewed down the c axis. On each site, we define a projector containing a $2s$ and a $2p_x$ orbitals with the local quantization axis chosen such that the linear combinations as depicted in the upper panel of Fig. 7(d) (in solid color) are obtained. The $2s$ and $2p$ orbitals get a weight of 1 and $\sqrt{2}$, respectively, which corresponds to the relative weights in an sp^2 hybrid. Also depicted are the other two hybrids at site s_2, which are obtained by a C_3 rotation. Together with the rotated hybrids at site s_1 these form six MOs, of which the bonding combinations, shown in the lower panel, form the three occupied sp^2 bands. These unnormalized bonding sp^2 MOs consist each of four LOs. A simple PYTHON script was used to setup these molecular orbital projectors, which essentially uses the C_3 rotation to determine the local axes of all contributing p orbitals.

The energy window, shown at the right side of Fig. 7(a) was chosen such that the most part of the target bands where sampled by a larger upper Gaussian tail with $\Delta_E = 7\,\text{eV}$. Due to the weak hybridization with the $2p_z$ band away from the high symmetry lines, the WF band energies at the band bottom along $\Gamma - \text{A}$ would be pulled to higher energies, compared to the FPLO bands, if a simple rectangular window encompassing the target bands would be chosen.

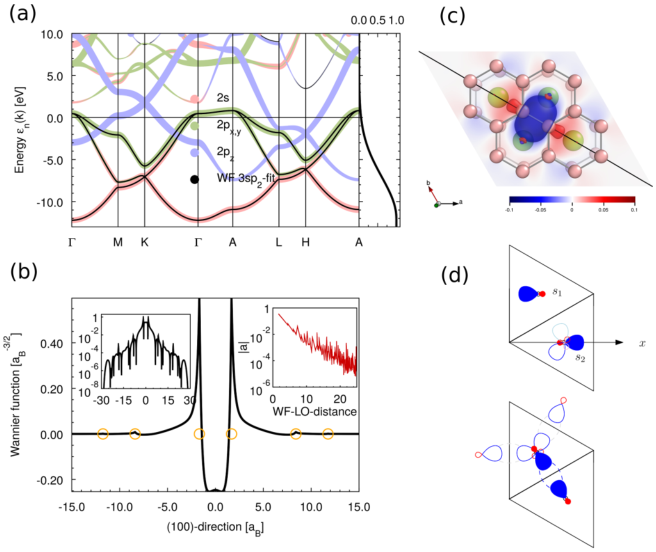

FIG. 7. (a) FPLO band weights in pastel colors compared to the sp^2-hybrid Wannier fit in black and the energy window plotted at the right side. (b) WF profile along a path through the Wannier center as indicated by the thin line in (c). The left inset shows $|w|$ along the same path in a logarithmic plot, while the right inset shows $\max(|a_{\boldsymbol{R}s,\boldsymbol{0}c}|)$, i.e., the orbital contributions to the WF, also in a logarithmic plot. (c) Isosurface of the WF for isovalue 0.4. (d) Schematic of the MO projectors used to obtain the WFs.

The three bands of the WF-fit in Fig. 7(a) accurately follow the FPLO band structure. Figure 7(c) shows an isosurface of one of the bonding sp^2 WFs together with a semitransparent density plot of the WF in the plane through it's center. Along a path, indicated by the thin line through the Wannier center, the WF has a profile as shown in Fig. 7(b), where the circles mark the positions of the boron atoms. The WF is clearly localized as shown by the logarithmic plot of $|w|$ along the path in the left inset and the logarithmic plot of the maximal orbital contributions [Eq. (24)] to the WF in the right inset.

F. Molecule Wannier functions

In FPLO, molecules are treated without a simulation box, since all orbitals have a finite compact support. The algorithm described in Sec. II A is not restricted to bulk materials. The only places where the extended nature of a sytem comes into play are $\boldsymbol{k}$ sums and by using the Γ point only (effectively no sum) one can also create molecule WFs. To illustrate this we will determine the smallest model Hamiltonian for an H_2O molecule (see Appendix C 6). There are four occupied valence MOs formed by O-$2s/2p$ and H-$1s$ orbitals of which one is formed to nearly 100% by the O-$2p_y$ orbital, whose lobes point out of the H-O-H plane and which hence is decoupled by symmetry from the other orbitals in lower orders, so that this orbital can be neglected in a model. To obtain WFs, we chose the O-$2s$, O-$2p_z$ and the two H-$1s$ orbitals as projectors. The O-$2p_x$ orbital will be pulled into the Wannier basis via hybridization tails at the other WFs by choosing an energy window $[-24, 0.3]\,\text{eV}$ with an upper $\Delta = 1\,\text{eV}$,

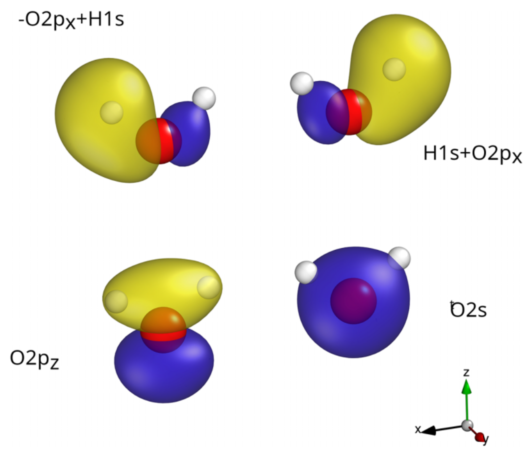

FIG. 8. Isosurfaces of the four WFs of the minimum model for H_2O for an isovalue of 0.09. The character is denoted at the side. The atoms are shown as white (H) and red (O) spheres.

which encompasses the four lowest valence MOs and some unoccupied states. This basis will fit the three mixed occupied MOs and one unoccupied MO. The corresponding Wannier model Hamiltonian (C1) will have the same eigenenergies as the corresponding MOs in the DFT calculation Eq. (C2) except for the omitted orbital. Isosurfaces of the resulting WFs in real space are shown in Fig. 8.

G. Post processing

For post processing of the Wannier function data a PYTHON package is provided. It reads the Wannier data and maps them onto a chosen structure. This can be the original unit cell forming the original lattice, any supercell and corresponding lattice, a semi infinite slab or a finite slab based on a chosen supercell. If the original lattice is 2d, the resulting slabs are one-dimensional. The slabs are idealized in the sense that no surface relaxation effects can be considered; it is a straightforward mapping of the original hoppings/data onto the sites forming the slabs. For the semi-infinite slab, the termination can be chosen and for the finite slab both terminations can be chosen and an arbitrary number of atoms can be removed to get a rough estimate of such effects on the surface states.

The python package offers an interface to obtain the Hamiltonian and all requested operators for a user specified $\boldsymbol{k}$ point, which provides maximum flexibility. It also offers ready made procedures to calculate several properties depending on the chosen structure mapping. For all but the semi-infinite mapping the band structure, including band weights, and Fermi surfaces and Fermi surface cuts can be calculated. For the original and super cell mappings, a bulk-projected band structure can be obtained which integrates the band structure along a chosen $\boldsymbol{k}$ direction. This offers the spectral densities with surface effects excluded.

For the semi-infinite slabs a Green's function method [23,24] is used to calculate spectral densities as a function of energy and momentum (band structure plot equivalent) or in a $\boldsymbol{k}$ plane (Fermi surface cut equivalent). Figure 9 shows an example of this for the ternary Type-II Weyl semimetal $TaIrTe_4$ [25].

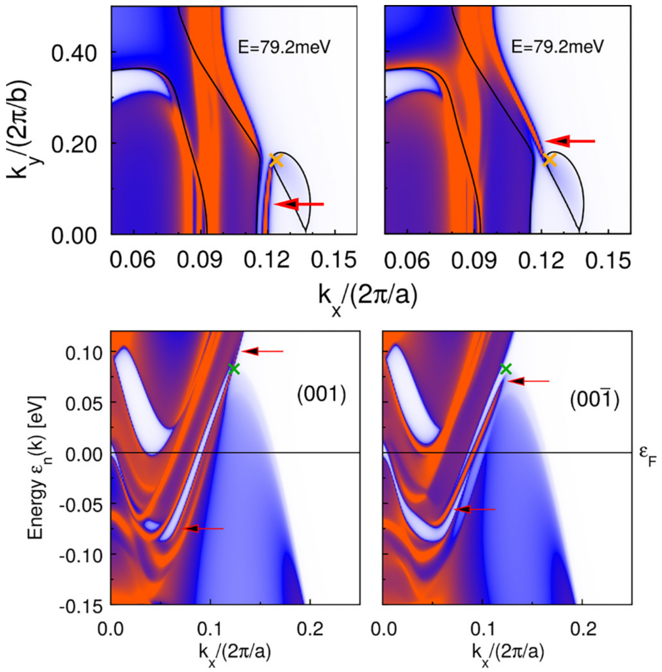

FIG. 9. Surface spectral densities (SD) for $TaIrTe_4$ of a semi infinite slab with (001) (left column) and $(00\bar{1})$ (right column) termination. The crosses mark the position of the Weyl point. (Top) Fermi surface SD, the arrows mark the Fermi arcs. (Bottom) Corresponding energy resolve SD along a line $k_y = 0.125$. The arrows mark the surface bands forming the arcs.

For the mapping onto the original lattice, the symmetry operations and their eigenvalues can be analyzed. Furthermore, an adaptive algorithm for the search for Weyl points (WP) is available. We use a 3d version of the methods of Ref. [26] to determine the chirality of each microcell of a regular subdivision of the primitive unit cell. Then in refinement steps for each cell with a nontrivial chirality the cell is subdivided into eight subcells for which the chirality again is determined. The subdivision stops if the subcell size falls bellow a specified threshold. For each found Weyl point, its veracity can be checked by calculating an integral of the Berry curvature over

TABLE I. CPU time in seconds for the cases discussed in Sec. IV on a single core of an Intel Xeon CPU E5-1650 @ 3.5 GHz. SCF: full self consistent calculation from scratch. WF: calculation of Wannier functions consisting of dumping the relevant data from a single SCF cycle (first number) and the actual WF creation run (second number). WF on grid: the WF creation run can optionally include the calculation of the WF on a real space grid for visualization, which is not needed in most applications. Post processing: for Fe the largest time is used for the calculation of the Berry curvature of Fig. 5(a).

	SCF	WF	WF on grid	Post processing
$CaCuO_2$	53	8 + 2	9	
Fe ($3d4s4p$)	39	11 + 10	76	198
FeAl	74	23 + 77	248	32
HgS	46	18 + 25	142	14
MgB_2	13	3 + 2	9	
H_2O	2.9	0.2 + 0.2	1.3	

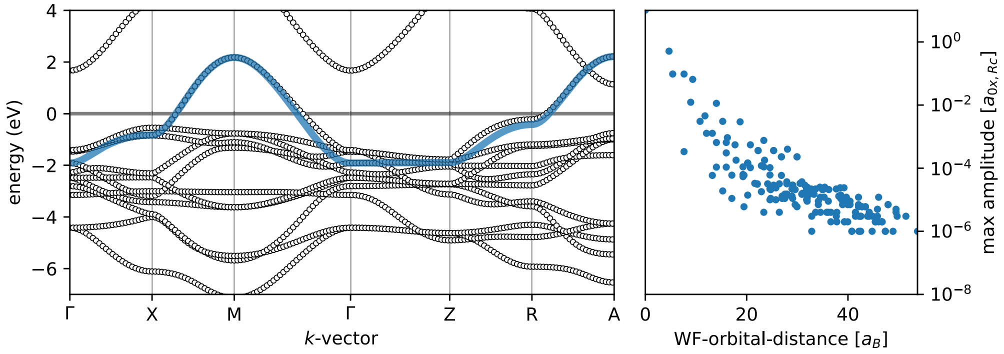

FIG. 10. (Left) LDA band structure of $CaCuO_2$ computed with QUANTUM ESPRESSO and Wannier fit for a one-orbital model performed using symmetry-adapted scheme implemented in WANNIER90. Right: maximal contributions to the WF in a logarithmic scale as a function of WF-orbital distance.

a small spherical shell around the WP, as well as creating a plot of the Berry curvature field for visual confirmation. The resulting Fermi arks can be analyzed by calculating the spectral density for a mapping onto a semi-infinite slab or by calculating the band structure and Fermi surface cuts for a finite slab.

Also for the original mapping the Z_2 topological indices can be determined for noncentrosymmetric lattices using a Wannier-center algorithm [27] with automatic determination of the indices [28]. This algorithm is also directly available from the FPLO code itself, by internally Löwdin orthogonalizing the whole FPLO basis (which results in full-basis Wannier functions), but it is faster to use a Wannier model due to the resulting basis reduction. For centrosymmetric lattices FPLO itself calculates the Z_2 indices.

The Berry curvature can be calculated band wise for any nonslab mapping either with approximated reduced position operator as discussed in Sec. III A or in full form, which also gives access to the anomalous Hall conductivity (Sec. IV D). By using the symmetry information mirror Chern numbers [29,30] for topological crystalline insulators can be obtained as well.

Besides Hamiltonian and reduced position operator in full-relativistic mode the spin operators and the exchange correlation magnetic field can be extracted. This is achieved by starting from the xc term of the Hamiltonian

$$H_B = \langle \Phi^{\boldsymbol{k}} | \beta \boldsymbol{\Sigma} \boldsymbol{B} | \Phi^{\boldsymbol{k}} \rangle, \tag{59}$$

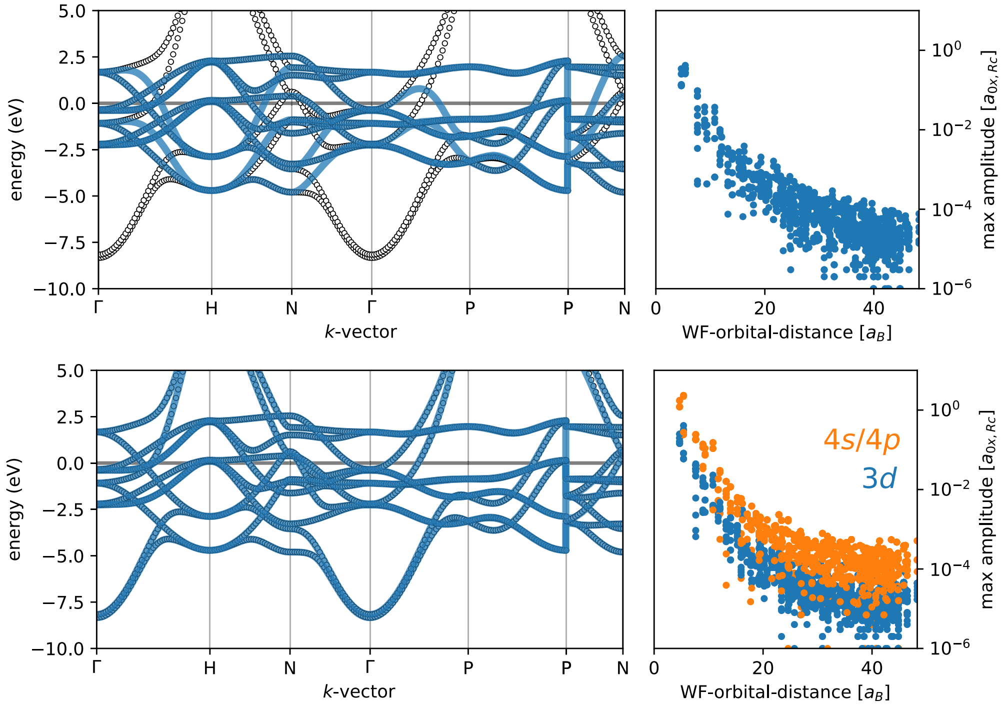

FIG. 11. (Top) Wannier fit of the LDA band structure of bcc Fe computed with QUANTUM ESPRESSO. The Wannier model is constructed by projections onto $3d$ states. Right panel shows maximal contributions to the WF in a logarithmic scale as a function of WF-orbital distance. Only the orbital-diagonal contributions are shown. (Bottom) Same for the model comprising $3d$, $4s$, and $4p$ states.

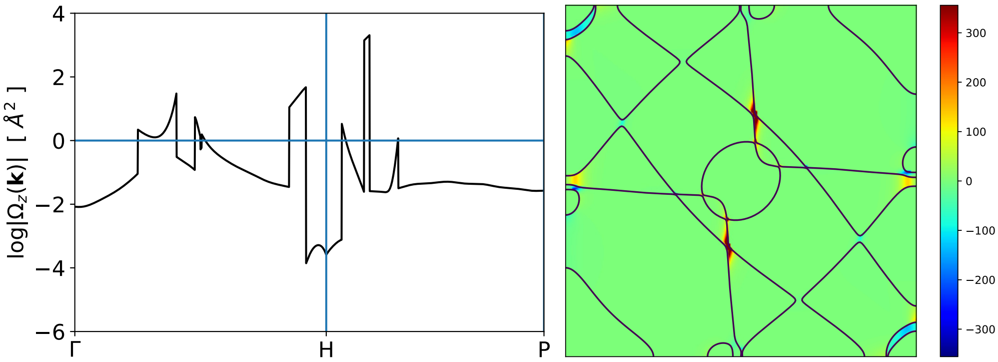

FIG. 12. Berry curvature of spin polarized full relativistic bcc Fe computed using WANNIER90.

where the 4 × 4 matrices β and $\mathbf{\Sigma}$ are defined as

$$\beta = \begin{pmatrix} \mathbf{1}_{2\times 2} & \\ & -\mathbf{1}_{2\times 2} \end{pmatrix}, \quad \mathbf{\Sigma} = \begin{pmatrix} \boldsymbol{\sigma} & \\ & \boldsymbol{\sigma} \end{pmatrix}. \tag{60}$$

$\boldsymbol{B}(\boldsymbol{r})$ is the xc-field and $\Phi^{\boldsymbol{k}}$ is the column vector of the FPLO basis orbitals. Assuming basis completeness, the identity

$$1 = |\Phi^{\boldsymbol{k}}\rangle \frac{1}{S^{\boldsymbol{k}}} \langle \Phi^{\boldsymbol{k}}| \tag{61}$$

can be inserted to separate the field followed by the Wannier transformation Eq. (18) using the identity $1 = S^{\boldsymbol{k}}_w = a^{\boldsymbol{k}+} S^{\boldsymbol{k}}_\Phi a^{\boldsymbol{k}}$, which leads to Wannier representation

$$H^w_B = \langle \beta \mathbf{\Sigma} \rangle^{\boldsymbol{k}}_w \langle \boldsymbol{B} \rangle^{\boldsymbol{k}}_w, \tag{62}$$

$$\langle \beta \mathbf{\Sigma} \rangle^{\boldsymbol{k}}_w = \langle w^{\boldsymbol{k}} | \beta \mathbf{\Sigma} | w^{\boldsymbol{k}} \rangle, \tag{63}$$

$$\langle \boldsymbol{B} \rangle^{\boldsymbol{k}}_w = \langle w^{\boldsymbol{k}} | \boldsymbol{B} | w^{\boldsymbol{k}} \rangle \tag{64}$$

with separate matrix representation for the vector of spin operators and of the xc field.

The spin operator matrix can be used to add model magnetic fields as was for instance done in Ref. [31] to simulate a canted magnetic field. The PYTHON interface provides model fields which are constant on user defined subsets of WFs with the definition

$$H^w_B = \sum_i P_i \langle \beta \mathbf{\Sigma} \rangle_w \boldsymbol{B}_i P_i, \tag{65}$$

where the diagonal of matrix P_i is one for the targeted WFs and zero otherwise and $\boldsymbol{B}_i$ is a constant vector.

The Wannier functions can also be used in the dHvA-package of FPLO instead of the full FPLO data [32]. Although the dHvA-package already uses an adaptive algorithm to sample the Fermi surface the use of a Wannier model can considerably speed of the process.

V. PERFORMANCE AND COMPARISON

A. Numerical performance

For orientation Table I shows the timing of various stages of the calculations of Sec. IV. We recorded the times for the complete self consistent calculation, for the single loop, which dumps the raw data needed for the WFs, for the actual Wannier function creation run, for the calculation of the WFs on a real space grid and for post processing, where it was used. All calculations are done on a single core.

B. Comparison with WANNIER90

At present, the most popular code in the community is WANNIER90 [4,33,34]. It supports interfaces with widely used band-structure codes has a growing number of postprocessing options [4]. It is therefore reasonable to use WANNIER90 for benchmarking our FPLO results. To this end, we use band-structure tools from the QUANTUM ESPRESSO package version 6.7 [35] and the wannierization software provided in WANNIER90 version 3.1.0. We use serial (single-core) executables compiled using the Intel's Math Kernel Library (MKL) version 2020.4.304. In contrast to the full-potential code FPLO, QUANTUM ESPRESSO does not calculate the potential of core electrons explicitly, it is adopted from external pseudopo-

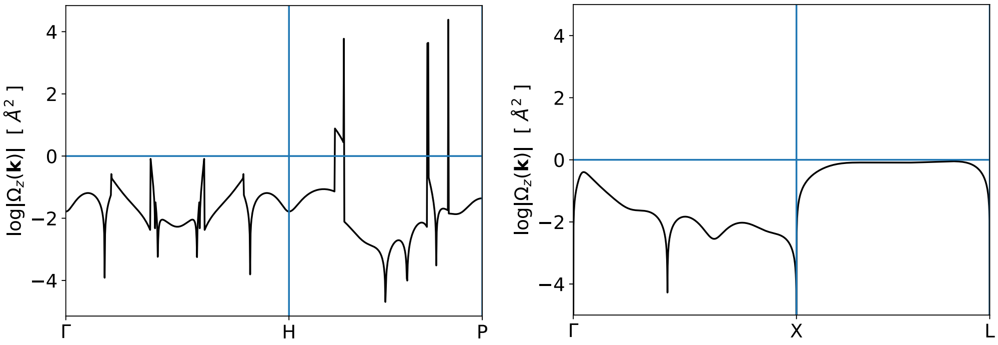

FIG. 13. Berry curvature of spin polarized full relativistic FeAl (left) and nonmagentic HgS (right) computed using WANNIER90.

TABLE II. Anomalous Hall effect.

Compound	Theory (S/cm)	Experiment (S/cm)	This work (S/cm)
Co_2FeAl	39 [41]	320–360 [52]	60
Co_2FeGa	181 [41]	50–350 [42]	210
Co_2FeSi	189 [41]	163, 400–600 [42,43]	260
Co_2FeGe	119 [41]		64
Fe_3Sn_2		200 400 [47,48]	590
$Co_3Sn_2S_2$		1100 [49]	1130
Co_2MnAl	1631 [50]		1520
Rh_2MnGa	1860 [50]		1760
Rh_2MnAl	1720 [50]		1640
Fe		1000 [44]	840
Fe_3GeTe_2		500 [51]	590
Ni	2200 [45]		2300
Co(hcp)	470 [45]		480
Co (fcc)	250 [46]		270

tential files. Here, we used ultrasoft LDA (Perdew-Wang 91 [36]) Rappe-Rabe-Kaxiras-Joannopoulos (RRKJ) pseudopotenitals [37] from PSLIBRARY version 1.0.0 [38], except for bcc-Fe calculations for which projector-augmented-wave pseudopotenitals [39] were employed.

We start with the one-orbital model for $CaCuO_2$. As these calculations do not include the spin-orbit coupling, we can use symmetry-adapted Wannier functions [5] implemented in WANNIER90 [4]. The agreement with the GGA band and the localization of the resulting Wannier functions (Fig. 10) are comparable to that in FPLO (Fig. 2).

Next, we consider full-relativistic calculations of bcc Fe. Again, we distinguish two models: a ten-band model which includes only the $3d$ states, and a 18-bands model, which additionally accounts for $4s$ and $4p$ contributions. The former provides a generally good description of the LDA band structure, but deviations can be seen with a naked eye (Fig. 11, top left). Inclusion of the $4s$ and $4p$ states readily yields an excellent description of the entire valence band and the low-energy region of the polarization band (Fig. 11, bottom left). Also here the degree of localization is comparable with respective models calculated using FPLO. Berry curvature calculations (Fig. 12) are in excellent quantitative agreement with the FPLO results (Fig. 5).

TABLE III. Anomalous Nernst effect. Maximum value with $T < 500K$ for Fe_3Pt, Fe_3Ga, Fe_3Al, Fe_3Si, and Fe_4N.

Compound	Theory (A/Km)	Experiment (A/Km)	This work
Fe_3Pt	6.2 [53]		4.0
Fe_3Ga	3.0 [53]		3.0
Fe_3Al	2.7 [53]		3.0
Fe_3Si	2.5 [53]		2.7
Fe_4N	2.4 [53]		1.1
Co_2MnGa	4 ($E_F = E_0$ +0.08 eV)	6.2 (300K) [54]	4.4 ($E_F = E_0$ +0.06 eV))
$Co_3Sn_2S_2$		3 (80K) [55]	2.6
Fe_3GeTe_2		0.3 (150 K) [56]	0.38

TABLE IV. Pt, SHC in unit of $(\hbar/e)$ (S/cm).

	Pt
	σ^z_{xy}
This work	2260
Ref. (*ab initio*)	2200 [61]
Ref. (*ab initio*)	2281 [62]
Ref. (*ab initio*)	∼2200 [63]
Ref. (*ab initio*)	∼2500 [64]
Ref. (Exp., $T = 10$ K)	1700 ± 400 [65]
Ref. (Exp., room temperature)	∼5100 [66]
Ref. (Exp., room temperature)	310 ± 50 [67]
Ref. (Exp., room temperature)	870 ± 120 [68]
Ref. (Exp., room temperature)	1750 [69]
Ref. (Exp., room temperature)	1900 [70]

Berry curvature of FeAl (Fig. 13, left) generally agrees with the FPLO result (Fig. 6, left), the discrepancies likely stem from the RRKJ pseudopotential for Fe. For HgS, the calculated Berry curvature does not vanish along the $\Gamma - X$ line (Fig. 13, right), in contrast with the FPLO result (Fig. 6, right). This discrepancy is however quite small and must be due to either symmetry violation (due to full relativistic mode) and or numerical artefacts, since we argued in Sec. IV D that the total contribution must vanish along this line.

C. Comparison with previous reports

We performed calculations of the anomalous Hall effect [15,16], the anomalous Nernst effect[40], and the spin Hall effect based on the symmetry conserving Wannier functions implemented in FPLO. Our results for the anomalous Hall conductivity in Heusler compounds Co_2FeX (X=Al, Ga, Si, and Ge) are around 60, 210, 260, and 64 S/cm, respectively, by choosing the magnetic moment along the z direction. We obtain good agreement with the previous *ab initio* report [41]. In addition to calculations, different groups also performed experimental Hall measurement for Co_2FeAl, Co_2FeGa, and Co_2FeSi. The calculated results fit well with the experimental measurements in Co_2FeGa and Co_2FeGe [42,43]. Though our results and previous *ab initio* reports give similar anomalous Hall conductivity for Co_2FeAl, it is much smaller than the

TABLE V. fcc Au, SHC is in unit of $(\hbar/e)$ (S/cm).

	Au
	σ^z_{xy}
This work	377
Ref. (*ab initio*)	400 [71]
Ref. (*ab initio*)	470 [64]
Ref. (*ab initio*)	350 [72]
Ref. (Exp., $T = 4$ K)	11100 [73]
Ref. (Exp., room temperature)	880 ± 80 [67]
Ref. (Exp., room temperature)	∼234 [74]
Ref. (Exp., room temperature)	500 ± 100 [75]
Ref. (Exp., room temperature)	42000 [76]

TABLE VI. fcc Pd, SHC in unit of $(\hbar/e)$ (S/cm).

	Pd
	σ_{xy}^{z}
This work	1180
Ref. (*ab initio*)	1200 [71]
Ref. (Exp., room temperature)	∼350 [77]
Ref. (Exp., $T = 10$ K)	270 ± 90 [65]
Ref. (Exp., room temperature)	260 ± 40 [67]
Ref. (Exp., room temperature)	∼200 [78]
Ref. (Exp., room temperature)	300 ± 70 [79]
Ref. (Exp., room temperature)	290 ± 50 [75]

value from Hall measurements [41], which might be due to a large extrinsic scattering contribution in the experimental setup.

For the anomalous Hall effect in typical transition elements such as Fe, Co, and Ni, our calculations show good agreement with both experimental measurements and previous *ab initio* calculations [44–46]. We also made comparisons with some typical magnetic topological materials from recent reports, such as Fe_3Sn_2 which features a massive Dirac cone [47,48], the first experimentally verified magnetic Weyl semimetal $Co_3Sn_2S_2$ [49], and the magnetic nodal line semimetals Rh_2MnGa, Rh_2MnAl, and Fe_3GeTe_2 [50,51]. We find good agreements for all of these magnetic topological systems, see Tables II.

Recently, starting with high throughput calculations, strong anomalous Nernst effects were observed in iron-based ferromagnets Fe_3X (X=Pt, Ga, Al, and Si) and Fe_4N [53]. From Table III, one can see the good agreement between our calculations and recent reports. We also find good agreements for the anomalous Nernst conductivity in typical magnetic topological materials Co_2MnGa [54], $Co_3Sn_2S_2$ [55], and Fe_3GeTe_2 [56]. All of them show the reliability of the Wannier functions derived from FPLO.

Another widely studied transport property in the linear response regime is the spin Hall effect [57–60] (SHC). We made a systematic comparison between reported results and that obtained from FPLO. We find that the results for cubic (bcc and fcc) transition metals from our calculations are in good agreement with previous *ab initio* calculations, see Tables IV–X. We also tried to compare our theoretical results to the experimental reports. However, the experimental values from different reports differ a lot, due to details of experimental setup and extrinsic contributions.

TABLE VII. bcc Ta, SHC in unit of $(\hbar/e)$ (S/cm).

	Ta
	σ_{xy}^{z}
This work	−133
Ref. (*ab initio*)	−142 [62]
Ref. (Exp., $T = 10$ K)	11 ± 3 [65]
Ref. (Exp., room temperature)	−630 [80]
Ref. (Exp., room temperature)	-160 ± 120 [81]

TABLE VIII. bcc Nb, SHC in unit of $(\hbar/e)$ (S/cm).

	Nb
	σ_{xy}^{z}
This work	−94
Ref. (Exp., $T = 10$ K)	100 ± 20 [65]

As for the hexagonal transition metals, there are some differences between our calculations and that from previous reports [84] (Tables XI and XII), but overall, the two calculations are in good agreement. The differences might be due to the different sets of coordinates for the hexagonal lattice vectors. So far, most of the experiments focused on cubic transition metals and some compounds, whereas, to the best of our knowledge, there are almost no experimental reports for hexagonal transition metals. In addition to the transition metals, we also made a comparison for other compounds with available experimental reports and *ab initio* calculations, see Table XIII, and here good agreements can also be found.

D. Berry curvature dipole

We also calculated the Berry curvature dipole [1] for the type-I Weyl semimetal TaAs and the type-II Weyl semimetal $TaIrTe_4$. The crystal structure of TaAs and $TaIrTe_4$ belong to point group 4*mm* and *mm*2, respectively. According to the symmetry analysis for these two point groups, TaAs has only one independent component with $D_{xy}=-D_{yx}$, and $TaIrTe_4$ has two independent components of D_{xy} and D_{yx}. Our calculations fulfill these symmetry restrictions. The results reach convergence at a dense k grid of 720^3 and 480^3 for TaAs and $TaIrTe_4$, respectively, see Fig. 14. The Berry curvature dipole has a value of about 0.37 for the xy component of TaAs, in good agreement with Ref. [91]. The Berry curvature dipole in $TaIrTe_4$ can reach up to around −0.19 and −0.50 for the xy and yx components, respectively.

VI. SUMMARY AND CONCLUSIONS

We thoroughly documented the underlying methods of the FPLO package for the construction of symmetry conserving maximally projected Wannier functions.

The method does not enforce maximum localization but rather results in Wannier functions with (near) maximum projection onto FPLO orbitals or linear combinations thereof, yet yields a very high degree of localization due to the nature of the orbitals while retaining the symmetry properties of the chosen projectors. The simplicity of this algorithm leads to numerical efficiency and a high level of accuracy, which is

TABLE IX. bcc W, SHC in unit of $(\hbar/e)$ (S/cm).

	W
	σ_{xy}^{z}
This work	−819
Ref. (*ab initio*)	−785 [82]
Ref. (Exp., room temperature)	-1270 ± 230 [83]

TABLE X. bcc Mo, SHC in unit of $(\hbar/e)$ (S/cm).

	Mo
	σ^z_{xy}
This work	−276
Ref. (Exp., $K = 10$ T)	−230 ± 50 [65]
Ref. (Exp., room temperature)	−23 ± 5 [67]

needed in the context of topological properties, where symmetry conservation is of the essence, especially when taking derivatives (e.g., for the Berry curvature dipole).

For a complete treatment of topological properties, the full Berry connection/curvature is desirable. To this end, we discussed the position operator matrix elements as they have to be treated in a local orbital context as well as their symmetry properties in the context of possible approximations of this operator. The latter gives valuable insights for the application of such approximations in tight binding models with implicit (unknown) Wannier basis.

TABLE XI. Hexagonal transitionmetals from [84]. The SHC is in unit of $(\hbar/e)$ (S/cm).

	σ^z_{xy}	σ^x_{yz}	σ^y_{zx}
Sc			
This work	−40	7	6
Ref. (*ab initio*)	∼50	∼−10	–
Ti			
This work	−2	−23	−19
Ref. (*ab initio*)	∼5	∼−15	–
Zn			
This work	−70	−6	−6
Ref. (*ab initio*)	∼−130	∼−20	–
Y			
This work	109	77	68
Ref. (*ab initio*)	∼140	∼40	–
Zr			
This work	−242	−48	−19
Ref. (*ab initio*)	∼−300	∼−60	–
Tc			
This work	−160	−18	−97
Ref. (*ab initio*)	∼−200	∼−140	–
Ru			
This work	90	190	163
Ref. (*ab initio*)	∼−10	∼90	–

TABLE XII. Continuation of Table XI. The SHC is in unit of $(\hbar/e)$ (S/cm).

	σ^z_{xy}	σ^x_{yz}	σ^y_{zx}
La			
This work	290	316	308
Ref. (*ab initio*)	∼150	∼300	–
Hf			
This work	−375	−53	112
Ref. (*ab initio*)	∼−800	∼−600	–
Re			
This work	−325	−441	−519
Ref. (*ab initio*)	∼−500	∼−700	–
Cd			
This work	−93	2	−5
Ref. (*ab initio*)	∼−30	∼−20	–
Os			
This work	−68	−162	−72
Ref. (*ab initio*)	∼−260	∼−300	–

The method has been applied to a set of compounds to illustrate various applicational aspects as well as to demonstrate the general quality of the resulting Wannier models and the available post processing tools.

TABLE XIII. Other compounds, SHC in unit of $(\hbar/e)$ (S/cm).

Pt_3O_4			
	bcc σ^z_{xy}	Cubic σ^z_{xy}	
This work	1420	215	
Ref. (*ab initio*) [85]	1838	244	
$PtTe_2$			
This work (largest component σ^x_{yz})	122		
Ref. (Exp. room temperature) [86]	100–800		
$NbSe_2$			
This work (largest component σ^z_{yx})	188		
Ref. (Exp. room temperature) [87]	∼150		
WTe_2			
	σ^x_{zy}	σ^y_{zx}	
This work	34	85	
Ref. (*ab initio*) [88]	∼20	∼80	
Ref. (Exp., room temperature) [88]	14–96		
Bi_2Se_3			
	σ^z_{xy}	σ^y_{zx}	σ^x_{yz}
This work	105	104	96
Ref. (Exp., room temperature) [89]	∼80		
Ref. (Exp., room temperature) [90]	500–1000		

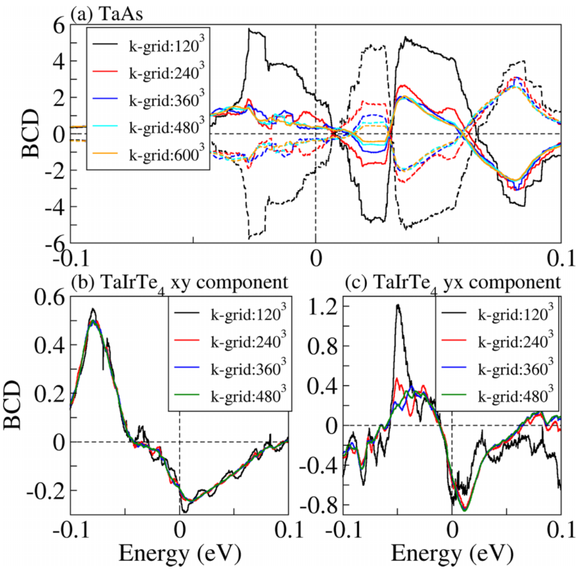

FIG. 14. (a) Berry curvature dipole of TaAs. The solid and dashed lines represent the *xy* and *yx* components, respectively. The Berry curvature dipole of (b) the *xy* component and (c) the *yx* component of TaIrTe$_4$.

We gave an idea of the efficiency of our method and repeated some of the calculations using the WANNIER90 package to convince the reader that our method indeed yields comparable results. We gave an extensive list of results for the anomalous Hall effect, the anomalous Nernst effect, and the spin Hall effect compared to results of other publications.

As a technical reference an extended Appendix documents the FPLO basis orbitals and their transformation properties from which the symmetry properties of the Wannier functions result.

In summary, we believe to have demonstrated that maximally projected symmetry conserving Wannier functions based on optimized local orbital methods have similar localization and flexibility as maximally localized Wannier functions, however with minimal computational cost and complexity and explicit symmetry properties.

ACKNOWLEDGMENTS

K.K. acknowledges inspirations by and discussions with Wei Ku, Helge Rosner, Alexander Tsirlin, and Manuel Richter. Ulrike Nitzsche is acknowledged for the maintenance of the ITF computational cluster and technical support. We acknowledge financial support by the Deutsche Forschungsgemeinschaft (DFG, German Research Foundation), through SFB 1143 project A5 and the Würzburg-Dresden Cluster of Excellence on Complexity and Topology in Quantum Matter-ct.qmat (EXC 2147, Project Id No. 390858490). O.J. was supported by the Leibniz Association (Project No. J50/2018) through the Leibniz Competition.

APPENDIX A: LOCAL BASIS STATES

1. FPLO basis

An FPLO basis orbital $\Phi_{\boldsymbol{R}s\nu}(\boldsymbol{r})$ is a solution of a Schrödinger/Dirac equation in an atom centered suitably modified potential with compact support. The boundary conditions are chosen such that there is no leakage of the orbital wave function at the compact support radius (this is not possible exactly in the Dirac case but practically the leakage can be made tiny and irrelevant). The orbitals sit in the unit cell at lattice vector $\boldsymbol{R}$ at site $\boldsymbol{s}$ and have quantum numbers ν. To be precise $\Phi_{\boldsymbol{R}s\nu}(\boldsymbol{r}) = \Phi_{s\nu}(\boldsymbol{r}-\boldsymbol{R}-\boldsymbol{s})$, where $\Phi_{s\nu}(\boldsymbol{r})$ is a function of atom site index s and qns. ν.

In non- and scalar-relativistic modes, the orbitals have the shape $\Phi_{snlm\sigma} = \varphi_{snl}(r)Y_{lm}(\hat{\boldsymbol{r}})\chi_\sigma$ where n is the main quantum number, Y_{lm} is a real spherical harmonic with angular momentum qns. l and m and χ_σ is a spin-1/2 basis spinor defined via $\sigma_z\chi_\sigma = \chi_\sigma\sigma$ ($\sigma = \pm 1$). The radial basis functions are not spin dependent which is compensated by the variational freedom of the chosen basis set which contains polarization orbitals additionally to the chemical valence (and semicore) orbitals.

In the full relativistic mode, the orbitals are solutions to a four-component Dirac equation and are four spinors

$$\Phi_{snlj\mu} = \begin{pmatrix} g_{snlj}(r)\chi_{\kappa\mu} \\ if_{snlj}(r)\chi_{-\kappa\mu} \end{pmatrix} \tag{A1}$$

with one large component (g_{snlj}) and one small component (f_{snlj}) radial function per lj-shell and spherical spinors $\chi_{\kappa\mu}$, where $\kappa = (2j+1)(l-j)$ are the eigenvalues of the spin orbit operator $\hat{\kappa} = 1 + \hat{\boldsymbol{\sigma}}\hat{\boldsymbol{L}}$ with $\hat{\kappa}\chi_{\kappa\mu} = -\chi_{\kappa\mu}\kappa$ (in detail $\kappa_{j=l-\frac{1}{2}} = l$ and $\kappa_{j=l+\frac{1}{2}} = -l-1$) and $\mu = -j, -j+1, \dots, j$ is the $\hat{J}_z$ eigenvalue.

The orbitals can be made orthonormal at each site. However, off-site orthonormality is hard to achieve, since this would mean to explicitly construct Wannier functions from the start. With a proper choice of orbitals a well conditioned overlap matrix

$$S_{\boldsymbol{R}'s'\nu',\boldsymbol{R}s\nu} = \langle \Phi_{\boldsymbol{R}'s'\nu'} | \Phi_{\boldsymbol{R}s\nu} \rangle$$

can be achieved. Lattice translations

$$\begin{aligned} \hat{T}_{\boldsymbol{R}'}\Phi_{\boldsymbol{R}s\nu}(\boldsymbol{r}) &= \Phi_{\boldsymbol{R}s\nu}(\boldsymbol{r}-\boldsymbol{R}') = \Phi_{s\nu}(\boldsymbol{r}-\boldsymbol{R}-\boldsymbol{s}-\boldsymbol{R}') \\ &= \Phi_{\boldsymbol{R}+\boldsymbol{R}',s\nu}(\boldsymbol{r}) \end{aligned} \tag{A2}$$

yield translation invariance according to

$$\begin{aligned} S_{\boldsymbol{R}'s'\nu',\boldsymbol{R}s\nu} &= \langle \hat{T}_{-\boldsymbol{R}'}\Phi_{\boldsymbol{R}'s'\nu'} | \hat{T}_{-\boldsymbol{R}'}\Phi_{\boldsymbol{R}s\nu} \rangle \\ &= \langle \Phi_{\boldsymbol{0}s'\nu'} | \Phi_{\boldsymbol{R}-\boldsymbol{R}',s\nu} \rangle \\ &= S_{\boldsymbol{0}s'\nu',\boldsymbol{R}-\boldsymbol{R}',s\nu}. \end{aligned} \tag{A3}$$

2. Bloch sums

In order to form extended basis states, Bloch sums of local orbitals are defined as

$$\Phi^{\boldsymbol{k}}_{s\nu}(\boldsymbol{r}) = \frac{1}{\sqrt{N}}\sum_{\boldsymbol{R}} e^{i\boldsymbol{k}(\boldsymbol{R}+\lambda\boldsymbol{s})}\Phi_{\boldsymbol{R}s\nu}(\boldsymbol{r}), \tag{A4}$$

where $\lambda = 0, 1$ ($\bar{\lambda} = 1-\lambda$) picks a particular phase gauge as discussed in the main text. The normalization contains the number of unit cells N in the Born-von-Kármán (BvK) torus, which is there for formal correctness but never actually appears in any coded formulas except for the normalization of the Fourier back transform. The Fourier transformed overlap matrix is defined as

$$\begin{aligned} S^{\boldsymbol{k}}_{\boldsymbol{s}'\nu',\boldsymbol{s}\nu} &= \frac{1}{N}\sum_{\boldsymbol{R}\boldsymbol{R}'} \mathrm{e}^{i\boldsymbol{k}(\boldsymbol{R}+\lambda\boldsymbol{s}-\boldsymbol{R}'-\lambda\boldsymbol{s}')} S_{\boldsymbol{R}'\boldsymbol{s}'\nu',\boldsymbol{R}\boldsymbol{s}\nu} \\ &= \frac{1}{N}\sum_{\boldsymbol{R}\boldsymbol{R}'} \mathrm{e}^{i\boldsymbol{k}(\boldsymbol{R}+\lambda\boldsymbol{s}-\boldsymbol{R}'-\lambda\boldsymbol{s}')} S_{\boldsymbol{0}\boldsymbol{s}'\nu',\boldsymbol{R}-\boldsymbol{R}'\boldsymbol{s}\nu} \\ &= \frac{1}{N}\sum_{\boldsymbol{R}'}\sum_{\boldsymbol{R}} \mathrm{e}^{i\boldsymbol{k}(\boldsymbol{R}+\lambda(\boldsymbol{s}-\boldsymbol{s}'))} S_{\boldsymbol{0}\boldsymbol{s}'\nu',\boldsymbol{R}\boldsymbol{s}\nu} \\ &= \sum_{\boldsymbol{R}} \mathrm{e}^{i\boldsymbol{k}(\boldsymbol{R}+\lambda(\boldsymbol{s}-\boldsymbol{s}'))} S_{\boldsymbol{0}\boldsymbol{s}'\nu',\boldsymbol{R}\boldsymbol{s}\nu}, \end{aligned} \tag{A5}$$

which motivates the normalization choice in Eq. (A4). The exponential contains the difference vector between the two orbital positions if $\lambda = 1$, which is why we call it *relative* gauge.

The overlap of a Bloch sum with a single basis orbital $\Phi_{\boldsymbol{R}\boldsymbol{s}\nu}$ reads

$$\begin{aligned} \left\langle \Phi^{\boldsymbol{k}}_{\boldsymbol{s}'\nu'} \middle| \Phi_{\boldsymbol{R}\boldsymbol{s}\nu} \right\rangle &= \frac{1}{\sqrt{N}}\sum_{\boldsymbol{R}'} \mathrm{e}^{-i\boldsymbol{k}(\boldsymbol{R}'+\lambda\boldsymbol{s}')} \langle \Phi_{\boldsymbol{R}'\boldsymbol{s}'\nu'} | \Phi_{\boldsymbol{R}\boldsymbol{s}\nu} \rangle \\ &= \frac{1}{\sqrt{N}}\sum_{\boldsymbol{R}'} \mathrm{e}^{-i\boldsymbol{k}(\boldsymbol{R}'+\lambda\boldsymbol{s}')} S_{\boldsymbol{R}'\boldsymbol{s}'\nu',\boldsymbol{R}\boldsymbol{s}\nu} \\ &= \frac{1}{\sqrt{N}}\sum_{\boldsymbol{R}'} \mathrm{e}^{-i\boldsymbol{k}(\boldsymbol{R}-\boldsymbol{R}'+\lambda\boldsymbol{s}')} S_{\boldsymbol{0}\boldsymbol{s}'\nu',\boldsymbol{R}'\boldsymbol{s}\nu} \\ &= \frac{1}{\sqrt{N}}\sum_{\boldsymbol{R}'} \mathrm{e}^{i\boldsymbol{k}(\boldsymbol{R}'+\lambda(\boldsymbol{s}-\boldsymbol{s}'))} S_{\boldsymbol{0}\boldsymbol{s}'\nu',\boldsymbol{R}'\boldsymbol{s}\nu} \mathrm{e}^{-i\boldsymbol{k}(\boldsymbol{R}+\lambda\boldsymbol{s})} \\ &= \frac{1}{\sqrt{N}} S^{\boldsymbol{k}}_{\boldsymbol{s}'\nu',\boldsymbol{s}\nu} \mathrm{e}^{-i\boldsymbol{k}(\boldsymbol{R}+\lambda\boldsymbol{s})} \end{aligned} \tag{A6}$$

using $\boldsymbol{R}' \to -\boldsymbol{R}' + \boldsymbol{R}$ and Eqs. (A3) and (A5). Using Eqs. (A4) and (A6), the overlap of two Bloch functions yields the overlap matrix

$$\left\langle \Phi^{\boldsymbol{k}}_{\boldsymbol{s}'\nu'} \middle| \Phi^{\boldsymbol{k}}_{\boldsymbol{s}\nu} \right\rangle = \frac{1}{N}\sum_{\boldsymbol{R}} S^{\boldsymbol{k}}_{\boldsymbol{s}'\nu',\boldsymbol{s}\nu} = S^{\boldsymbol{k}}_{\boldsymbol{s}'\nu',\boldsymbol{s}\nu}.$$

We introduce local linear combinations of orbitals (MOs) for projection purposes

$$\phi_{\boldsymbol{R}\boldsymbol{c}i} = \sum_{\boldsymbol{R}'\boldsymbol{s}\nu'} \Phi_{\boldsymbol{R}'\boldsymbol{s}\nu'} U_{\boldsymbol{R}'\boldsymbol{s}\nu',\boldsymbol{R}\boldsymbol{c}i}, \tag{A7}$$

which shall be translation invariant in the same way as the orbitals Eq. (A2), i.e., $U_{\boldsymbol{R}'\boldsymbol{s}\nu',\boldsymbol{R}\boldsymbol{c}i} = U_{\boldsymbol{0}\boldsymbol{s}\nu',\boldsymbol{R}-\boldsymbol{R}'\boldsymbol{c}i}$ and have Bloch sums

$$\begin{aligned} \phi^{\boldsymbol{k}}_{\boldsymbol{c}i} &= \frac{1}{\sqrt{N}}\sum_{\boldsymbol{R}} \mathrm{e}^{i\boldsymbol{k}(\boldsymbol{R}+\lambda\boldsymbol{c})} \phi_{\boldsymbol{R}\boldsymbol{c}i} = \sum_{\boldsymbol{s}\nu'} \Phi^{\boldsymbol{k}}_{\boldsymbol{s}\nu'} U^{\boldsymbol{k}}_{\boldsymbol{s}\nu',\boldsymbol{c}i}, \\ U^{\boldsymbol{k}}_{\boldsymbol{s}\nu',\boldsymbol{c}i} &= \sum_{\boldsymbol{R}} U_{0\boldsymbol{s}\nu',\boldsymbol{R}\boldsymbol{c}i} \mathrm{e}^{i\boldsymbol{k}(\boldsymbol{R}+\lambda\boldsymbol{c}-\lambda\boldsymbol{s})}. \end{aligned}$$

To calculate the overlap between a MO and an orbital Bloch sum, Eq. (A6) gets then modified according to

$$\left\langle \Phi^{\boldsymbol{k}}_{\boldsymbol{s}\nu} \middle| \phi_{\boldsymbol{R}\boldsymbol{c}i} \right\rangle = \frac{1}{\sqrt{N}} (S^{\boldsymbol{k}} U^{\boldsymbol{k}})_{\boldsymbol{s}\nu,\boldsymbol{c}i} \mathrm{e}^{-i\boldsymbol{k}(\boldsymbol{R}+\lambda\boldsymbol{c})}. \tag{A8}$$

The Fourier back transformation which yields real space objects is practically obtained by a $\boldsymbol{k}$ sum whose underlying mesh implicitly defines the BvK torus and N

$$S_{\boldsymbol{0}\boldsymbol{s}',\boldsymbol{R}\boldsymbol{s}} = \sum_{\boldsymbol{k}} f_{\boldsymbol{k}} \mathrm{e}^{-i\boldsymbol{k}(\boldsymbol{R}+\lambda(\boldsymbol{s}-\boldsymbol{s}'))} S^{\boldsymbol{k}}_{\boldsymbol{s}'\boldsymbol{s}} \tag{A9}$$

with

$$\sum_{\boldsymbol{k}} f_{\boldsymbol{k}} = 1.$$

If the full mesh is used $f_{\boldsymbol{k}} = N^{-1}$, but if only irreducible $\boldsymbol{k}$ points are used $f_{\boldsymbol{k}}$ is corrected for the multiplicity of the irreducible point. Combining Eqs. (A5) and (A9), one gets

$$\sum_{\boldsymbol{k}} f_{\boldsymbol{k}} \mathrm{e}^{i\boldsymbol{k}(\boldsymbol{R}-\boldsymbol{R}')} = \delta_{\boldsymbol{R},\boldsymbol{R}'},$$

which is only true modulo a lattice vector which describes the BvK periodicity. The back transformation of a Bloch sum itself with correct normalization reads

$$\Phi_{\boldsymbol{R}\boldsymbol{s}} = \frac{1}{\sqrt{N}}\sum_{\boldsymbol{k}} \mathrm{e}^{-i\boldsymbol{k}(\boldsymbol{R}+\boldsymbol{s})} \Phi^{\boldsymbol{k}}_{\boldsymbol{s}}.$$

A translation invariant operator in Bloch sum basis (as the overlap) contains two Bloch sums and is diagonal in $\boldsymbol{k}$ space. A full Fourier back transformation of both sides of the matrix then reduces to Eq. (A9) with $1/N$ normalization instead of $1/\sqrt{N}$.

APPENDIX B: SYMMETRY

1. Local basis symmetry

The complex spherical harmonics are defined as

$$\mathcal{Y}_{lm}(\varphi,\theta) = (-1)^{\frac{m+|m|}{2}} \sqrt{\frac{2l+1}{4\pi}\frac{(l-|m|)!}{(l+|m|)!}} P_l^{|m|}(\cos\theta)\mathrm{e}^{im\varphi} \tag{B1}$$

with the associated Legendre functions for positive m as a function of $z = \cos(\theta)$

$$\begin{aligned} P_l^m(z) &= (1-z^2)^{\frac{m}{2}} \frac{d^m}{dz^m} P_l(z), \\ P_l(z) \equiv P_l^0(z) &= \frac{1}{2^l l!}\frac{d^l}{dz^l}(z^2-1)^l. \end{aligned}$$

From this, the real harmonics are obtained via

$$\begin{aligned} Y_{lm}(\theta,\varphi) &= \sum_{m'} \mathcal{Y}_{lm'}(\theta,\varphi) U^*_{mm'} \\ &= \begin{cases} \frac{1}{\sqrt{2}}((-1)^m \mathcal{Y}_{l|m|} + \mathcal{Y}_{l-|m|}) & m > 0 \\ \mathcal{Y}_{l0} & m = 0 \\ \frac{1}{i\sqrt{2}}\left((-1)^{|m|}\mathcal{Y}_{l|m|} - \mathcal{Y}_{l-|m|}\right) & m < 0 \end{cases}. \end{aligned} \tag{B2}$$

The spherical spinors as introduced after Eq. (A1) are defined as

$$\chi_{\kappa\mu} = \sum_{s=\pm1} \chi_s \mathcal{Y}_{l\mu-\frac{s}{2}} c^s_{\kappa\mu} \tag{B3}$$

with basis spinors χ_s, complex harmonics Eq. (B1) and Clebsch-Gordon coefficients

$$c^s_{\kappa\mu} = -\left(\frac{s(\kappa+|\kappa|)+(\kappa-|\kappa|)}{2|\kappa|}\right)\sqrt{\frac{1}{2} - s\frac{\mu}{(2\kappa+1)}},$$

which can be written as

$$\begin{aligned}
\chi_{\kappa\mu} &= \sum_{s=\pm 1, m=-l_\kappa}^{l_\kappa} \chi_s \mathcal{Y}_{l_\kappa m} T^{l_\kappa}_{ms,\kappa\mu},\\
\chi_{\kappa\mu} &= \sum_{s=\pm 1, m=-l_\kappa}^{l_\kappa} \chi_s Y_{l_\kappa m} (UT)^{l_\kappa}_{ms,\kappa\mu},\\
T^l_{ms,\kappa\mu} &= \delta_{m,\mu-\frac{s}{2}} c^s_{\kappa\mu}
\end{aligned} \tag{B4}$$

with $l_\kappa = \frac{|2\kappa+1|-1}{2}$, where T^l can be arranged in a unitary matrix for each l shell.

Inversion $\hat{I}\boldsymbol{r} = -\boldsymbol{r}$ at the origin of the harmonics with $\hat{I}f(\boldsymbol{r}) = f(-\boldsymbol{r})$ acts like

$$\hat{I}\mathcal{Y}_{lm} = \mathcal{Y}_{lm}(-1)^l, \quad \hat{I}Y_{lm} = Y_{lm}(-1)^l, \quad \hat{I}\chi_{\kappa\mu} = \chi_{\kappa\mu}(-1)^{l_\kappa},$$
$$\hat{I}\chi_s = \chi_s.$$

A proper rotation $\hat{\alpha}$ with $\hat{\alpha}f(\boldsymbol{r}) = f(\hat{\alpha}^{-1}\boldsymbol{r})$ parametrized by the Euler angles is represented by the Wigner-D functions in the l or lj basis which without further details reads

$$\hat{\alpha}\mathcal{Y}_{lm} = \sum_{m'=-l}^{l} \mathcal{Y}_{lm'} D^l_{m'm}(\alpha), \tag{B5a}$$

$$\hat{\alpha}Y_{lm} = \sum_{m'=-l}^{l} Y_{lm'} \tilde{D}^l_{m'm}(\alpha),$$

$$\hat{\alpha}\chi_{\kappa\mu} = \sum_{\mu'=-j_\kappa}^{j_\kappa} \chi_{\kappa\mu'} D^{j_\kappa}_{\mu'\mu}(\alpha), \tag{B5b}$$

$$\hat{\alpha}\chi_\sigma = \sum_{\sigma'=\pm 1} \chi_{\sigma'} D^{\frac{1}{2}}_{\sigma'\sigma}(\alpha), \tag{B5c}$$

where $j_\kappa = \frac{2|\kappa|-1}{2}$ and $\tilde{D}_{m'm}(\alpha) = (UD(\alpha)U^+)_{m'm}$, with U from Eq. (B2).

From Eqs. (B3)–(B5)

$$D^{\frac{1}{2}} D^l T^l = T^l D^j \tag{B6}$$

where all matrices must be appropriately formed for the complete l shell (which includes the two $j = l \pm \frac{1}{2}$ subshells or the single $j = \frac{1}{2}$ shell for $l = 0$). Now, since $j_{-\kappa} = j_\kappa$ both spherical spinors in Eq. (A1) transform with the same D^{j_κ} and Eq. (B6) yields

$$\hat{\alpha}(\Phi^l T^{l+}) = (\Phi^l T^{l+}) D^{\frac{1}{2}} D^l, \tag{B7}$$

which shows that the totality of all four spinors of an l shell $\Phi^l = (\Phi^l_{j=l-\frac{1}{2}} \Phi^l_{j=l+\frac{1}{2}})$ multiplied by T^{l+} transforms as nonrelativistic complex harmonics $\mathcal{Y}$ (or as real harmonics Y if $(UT^l)^+$ is used).

Finally, the time reversal operator is defined as $\theta = -i\sigma_y K_0$, where σ_y is the y component of the Pauli matrix vector and K_0 is complex conjugation, which gives the general action $\theta f_i = \sum_{i'} f_{i'} D^\theta_{i'i} K_0$, where D^θ can be read off the following relations:

$$\theta\mathcal{Y}_{lm} = \mathcal{Y}_{l-m}(-1)^m\theta, \tag{B8a}$$

$$\theta Y_{lm} = Y_{lm}\theta, \tag{B8b}$$

$$\theta\chi_{\kappa\mu} = \chi_{\kappa-\mu}(-1)^{l+j-\mu}K_0, \tag{B8c}$$

$$\theta\chi_\sigma = \chi_{-\sigma}\sigma K_0. \tag{B8d}$$

2. Space group symmetry/time reversal

The space group contains the set of operations

$$T_{\boldsymbol{R}}g = T_{\boldsymbol{R}}\{\alpha|\boldsymbol{\tau}_\alpha\} = \{\alpha|\boldsymbol{\tau}_\alpha + \boldsymbol{R}\},$$

where $T_{\boldsymbol{R}}$ is a lattice translation and $g = \{\alpha|\boldsymbol{\tau}_\alpha\}$ is the Seitz symbol containing a proper/improper rotation α and a nonlattice translation $\boldsymbol{\tau}_\alpha$. The latter depends on the origin choice and a particular pick among all the vectors $\boldsymbol{\tau}_\alpha + \boldsymbol{R}$. A real space vector transforms according to

$$T_R g\boldsymbol{r} = \{\alpha|\boldsymbol{\tau} + \boldsymbol{R}\}\boldsymbol{r} = g\boldsymbol{r} + \boldsymbol{R} = \alpha\boldsymbol{r} + \boldsymbol{\tau} + \boldsymbol{R}.$$

This is especially true for a lattice site $\boldsymbol{s} + \boldsymbol{R}'$ for which one gets

$$T_R g(\boldsymbol{R}' + \boldsymbol{s}) = \alpha\boldsymbol{R}' + g\boldsymbol{s} + \boldsymbol{R} = \alpha\boldsymbol{R}' + \alpha\boldsymbol{s} + \boldsymbol{\tau} + \boldsymbol{R}.$$

The inverse is given by

$$\{\alpha|\boldsymbol{\tau} + \boldsymbol{R}\}^{-1} = \{\alpha^{-1}| - \alpha^{-1}(\boldsymbol{\tau} + \boldsymbol{R})\}. \tag{B9}$$

When setting up a structure a certain set of sites will be generated. They do not need to lie in the first unit cell. The set of transformed sites $g\boldsymbol{s}$ will in general not be identical to this original set. A simple lattice translation

$$g\boldsymbol{s} = \boldsymbol{s}_g + \boldsymbol{R}_{g,s}$$

will map the transformed set back onto the original one. If this is done consistently, the site numbers s, s_g can be used as indices to orbitals and Bloch sums.

The vector of all orbitals (and of Wannier functions) at a site transforms according to

$$\begin{aligned}
g\Phi_{\boldsymbol{R}\boldsymbol{s}}(\boldsymbol{r}) &= g\Phi_s(\boldsymbol{r} - \boldsymbol{R} - \boldsymbol{s})\\
&= \Phi_s(g^{-1}\boldsymbol{r} - \boldsymbol{R} - \boldsymbol{s})\\
&= \Phi_s(\alpha^{-1}(\boldsymbol{r} - \boldsymbol{\tau}) - \boldsymbol{R} - \boldsymbol{s})\\
&= \Phi_s(\alpha^{-1}(\boldsymbol{r} - \alpha\boldsymbol{R} - \alpha\boldsymbol{s} - \boldsymbol{\tau}))\\
&= \Phi_s(\boldsymbol{r} - \alpha\boldsymbol{R} - \boldsymbol{s}_g - \boldsymbol{R}_{g,s})D^\Phi_s(\alpha)\\
&= \Phi_{\alpha\boldsymbol{R}+\boldsymbol{R}_{g,s},\boldsymbol{s}_g}(\boldsymbol{r})D^\Phi_s(\alpha) && \text{(B10a)}\\
&= \Phi_{g(\boldsymbol{R}\boldsymbol{s})}(\boldsymbol{r})D^\Phi_s(\alpha), && \text{(B10b)}
\end{aligned}$$

where $D^\Phi_s(\alpha)$ is the appropriate transformation matrix, which transforms orbitals at site indexed by s into orbitals at site indexed by s_g. For the FPLO basis, these matrices are the same at each site and are obtained according to Appendix B 1. The last row, Eq. (B10b), is a useful short hand for Eq. (B10a) in deriving symmetry properties since $g(\boldsymbol{R} + \boldsymbol{s})$ is a complete set of lattice sites which can serve as summation variable.

In case of molecular orbitals as WF projectors, the symmetry properties of the WFs is an implicit input in our method an they are required to transform akin to Eq. (B10a). The input matrix U in Eq. (A7) together with the transformation properties of the orbitals D_s^Φ determine the transformation properties of $\phi_{\boldsymbol{c}}$ completely. In practice, one chooses U in Eq. (A7). The code looks if application of symmetry replicates the set of Wannier functions and if the resulting matrices D_c^ϕ are unitary. If not the input is invalid. This requires the following relations

$$\begin{aligned} g\phi_{\boldsymbol{c}} &= \sum_{\boldsymbol{Rs}} g\Phi_{\boldsymbol{Rs}} U_{\boldsymbol{Rs},\boldsymbol{0c}} \\ &= \sum_{\boldsymbol{Rs}} \Phi_{g(\boldsymbol{Rs})} D_s^\Phi(\alpha) U_{\boldsymbol{Rs},\boldsymbol{0c}} \\ &= \phi_{g\boldsymbol{c}} D_c^\phi(\alpha) \\ &= \sum_{\boldsymbol{Rs}} \Phi_{\boldsymbol{Rs}} U_{\boldsymbol{Rs},g\boldsymbol{c}} D_c^\phi(\alpha) \\ &= \sum_{\boldsymbol{Rs}} \Phi_{g(\boldsymbol{Rs})} U_{g(\boldsymbol{Rs}),g\boldsymbol{c}} D_c^\phi(\alpha) \end{aligned}$$

or

$$U_{\boldsymbol{Rs},\boldsymbol{0c}} = \left(D_s^\Phi(\alpha)\right)^+ U_{g(\boldsymbol{Rs}),g\boldsymbol{c}} D_c^\phi(\alpha),$$

where again we need to replace $g(\boldsymbol{Rs})$ by $\alpha\boldsymbol{R} + \boldsymbol{R}_{g,s}$, $\boldsymbol{s}_g$ and $g\boldsymbol{c}$ by $\boldsymbol{R}_{g,\boldsymbol{c}}$, $\boldsymbol{c}_g$.

Additionally, useful operators need to be lattice periodic

$$T_{\boldsymbol{R}} \hat{B}(\boldsymbol{r}) T_{\boldsymbol{R}}^{-1} = \hat{B}(\boldsymbol{r}-\boldsymbol{R}) = \hat{B}(\boldsymbol{r}) \tag{B11}$$

and invariant under the space group

$$g\hat{B}(\boldsymbol{r})g^{-1} = \hat{B}(g^{-1}\boldsymbol{r}) = \hat{B}(\boldsymbol{r})D^B(\alpha), \tag{B12}$$

where $D^B(\alpha)$ is the representation matrix of the operator. For example, $D^B(\hat{I}\alpha) = \pm\alpha$ if $\hat{B}$ is a polar ($+\alpha$) or axial ($-\alpha$) vector and α a proper rotation. This does however not apply to the position operator $\hat{\boldsymbol{r}}$, since it is not translational invariant. For all point group operations which leave the origin invariant, $\hat{\alpha}\hat{\boldsymbol{r}}\hat{\alpha}^{-1} = \alpha^{-1}\boldsymbol{r} = \boldsymbol{r}\alpha$ holds, but for a general space group operation one gets $g\hat{\boldsymbol{r}}g^{-1} = \alpha^{-1}(\boldsymbol{r}-\boldsymbol{\tau}) = (\boldsymbol{r}-\boldsymbol{\tau})\alpha$.

If time reversal applies, it yields

$$\theta\hat{B}(\boldsymbol{r})\theta^{-1} = \hat{B}(\boldsymbol{r})D^B(\theta), \tag{B13}$$

where $D^B(\theta)$ is, e.g., $+1$ for the Hamiltonian and -1 for the spin and magnetic field. In full relativistic spin polarized mode products of time reversal with operations, which flip the magnetic field, are group elements. We apply the latter only to the subset of the actual space group, which preserves the magnetization axis, i.e., we do not implement full magnetic groups.

Using the shorthand Eq. (B10b) with its meaning Eq. (B10a) matrix elements transform as

$$\begin{aligned} B_{\boldsymbol{R}'\boldsymbol{s}',\boldsymbol{Rs}} &= \langle \Phi_{\boldsymbol{R}'\boldsymbol{s}'}|\hat{B}|\Phi_{\boldsymbol{Rs}}\rangle \\ &= \langle g\Phi_{\boldsymbol{R}'\boldsymbol{s}'}|g\hat{B}g^{-1}|g\Phi_{\boldsymbol{Rs}}\rangle \\ &= D_{s'}^{\Phi+}\langle \Phi_{g(\boldsymbol{R}'\boldsymbol{s}')}|\hat{B}|\Phi_{g(\boldsymbol{Rs})}\rangle D_s^\Phi D^B \\ &= D_{s'}^{\Phi+} B_{g(\boldsymbol{R}'\boldsymbol{s}'),g(\boldsymbol{Rs})} D_s^\Phi D^B, \end{aligned} \tag{B14}$$

where D^B applies to the degrees of freedom of the internal tensor structure of B.

With the general behavior [details in Eq. (B8)]

$$\theta\Phi = \Phi D^{\Phi\theta} K_0, \tag{B15a}$$

$$\Phi^+\theta^{-1} = K_0 D^{\Phi\theta+}\Phi^+, \tag{B15b}$$

one gets the general behavior of matrix elements under time reversal

$$\begin{aligned} B_{\boldsymbol{R}'\boldsymbol{s}',\boldsymbol{Rs}} &= \langle \Phi_{\boldsymbol{R}'\boldsymbol{s}'}|\theta^{-1}\theta\hat{B}\theta^{-1}\theta|\Phi_{\boldsymbol{Rs}}\rangle \\ &= K_0 D_{s'}^{\Phi\theta+}\langle \Phi_{\boldsymbol{R}'\boldsymbol{s}'}|\hat{B}D^{B\theta}|\Phi_{\boldsymbol{Rs}}\rangle D_s^{\Phi\theta} K_0 \\ &= (D_{s'}^{\Phi\theta+}\hat{B}_{\boldsymbol{R}'\boldsymbol{s}',\boldsymbol{Rs}} D_s^{\Phi\theta} D^{B\theta})^*. \end{aligned} \tag{B16}$$

Now, the transformation of Bloch sums of LOs/WFs is obtained from Eqs. (A4) and (B10a) where the use of backfolded sites $\boldsymbol{s}_g$ is of the essence

$$\begin{aligned} g\Phi_{\boldsymbol{s}}^{\boldsymbol{k}} &= \frac{1}{\sqrt{N}}\sum_{\boldsymbol{R}} \mathrm{e}^{i\boldsymbol{k}(\boldsymbol{R}+\lambda\boldsymbol{s})} g\Phi_{\boldsymbol{Rs}} \\ &= \frac{1}{\sqrt{N}}\sum_{\boldsymbol{R}} \mathrm{e}^{i\boldsymbol{k}(\boldsymbol{R}+\lambda\boldsymbol{s})} \Phi_{\alpha\boldsymbol{R}+\boldsymbol{R}_{g,s},\boldsymbol{s}_g} D_s^\Phi \\ &= \frac{1}{\sqrt{N}}\sum_{\boldsymbol{R}} \mathrm{e}^{i\alpha\boldsymbol{k}(\alpha\boldsymbol{R}+\lambda\alpha\boldsymbol{s})} \Phi_{\alpha\boldsymbol{R}+\boldsymbol{R}_{g,s},\boldsymbol{s}_g} D_s^\Phi \\ &= \frac{1}{\sqrt{N}}\sum_{\boldsymbol{R}} \mathrm{e}^{i\alpha\boldsymbol{k}\left(\boldsymbol{R}+\lambda\boldsymbol{s}_g+\lambda\alpha\boldsymbol{s}-\boldsymbol{R}_{g,s}-\lambda\boldsymbol{s}_g\right)} \Phi_{\boldsymbol{R}\boldsymbol{s}_g} D_s^\Phi \\ &= \Phi_{\boldsymbol{s}_g}^{\alpha\boldsymbol{k}} D_s^\Phi \mathrm{e}^{i\alpha\boldsymbol{k}\left(\lambda\alpha\boldsymbol{s}-\boldsymbol{R}_{g,s}-\lambda\boldsymbol{s}_g\right)} \\ &= (\Phi^{\alpha\boldsymbol{k}} D^{\Phi\boldsymbol{k}})_{\boldsymbol{s}} \end{aligned} \tag{B17}$$

with

$$D_{s's}^{\Phi\boldsymbol{k}} = \delta_{s's_g} D_s^\Phi \mathrm{e}^{-i\alpha\boldsymbol{k}(\bar{\lambda}(g\boldsymbol{s}-\boldsymbol{s}_g)+\lambda\boldsymbol{\tau})}. \tag{B18}$$

Forming matrix elements of $\hat{B}$ with Bloch sums, inserting pairs of gg^{-1} and using Eqs. (B12) and (B17) yields

$$\left\langle \Phi_{\boldsymbol{s}'}^{\boldsymbol{k}}\middle|\hat{B}\middle|\Phi_{\boldsymbol{s}}^{\boldsymbol{k}}\right\rangle = \left\langle g\Phi_{\boldsymbol{s}'}^{\boldsymbol{k}}\middle|g\hat{B}g^{-1}\middle|g\Phi_{\boldsymbol{s}}^{\boldsymbol{k}}\right\rangle \tag{B19}$$

$$= \mathrm{e}^{i\alpha\boldsymbol{k}\bar{\lambda}(g\boldsymbol{s}'-\boldsymbol{s}'_g)} D_{s'}^{\Phi+}\left\langle \Phi_{\boldsymbol{s}'_g}^{\alpha\boldsymbol{k}}\middle|\hat{B}\middle|\Phi_{\boldsymbol{s}_g}^{\alpha\boldsymbol{k}}\right\rangle D_s^\Phi D^B \mathrm{e}^{-i\alpha\boldsymbol{k}\bar{\lambda}(g\boldsymbol{s}-\boldsymbol{s}_g)} \tag{B20}$$

from this one sees that the relative gauge $\bar{\lambda} = 0$ leads to simpler expressions, since all the phase factors in Eq. (B20) vanish.

Equations (A4) and (B15a) gives the time reversal of the orbital Bloch sums

$$\begin{aligned} \theta\Phi_{\boldsymbol{s}}^{\boldsymbol{k}} &= \theta\frac{1}{\sqrt{N}}\sum_{\boldsymbol{R}} \mathrm{e}^{i\boldsymbol{k}(\boldsymbol{R}+\lambda\boldsymbol{s})}\Phi_{\boldsymbol{Rs}} \\ &= \frac{1}{\sqrt{N}}\sum_{\boldsymbol{R}} \mathrm{e}^{-i\boldsymbol{k}(\boldsymbol{R}+\lambda\boldsymbol{s})}\theta\Phi_{\boldsymbol{Rs}} \\ &= \frac{1}{\sqrt{N}}\sum_{\boldsymbol{R}} \mathrm{e}^{-i\boldsymbol{k}(\boldsymbol{R}+\lambda\boldsymbol{s})}\Phi_{\boldsymbol{Rs}} D_s^{\Phi\theta} K_0 \\ &= \Phi_{\boldsymbol{s}}^{-\boldsymbol{k}} D_s^{\Phi\theta} K_0 \end{aligned} \tag{B21}$$

and together with Eqs. (B15b) and (B13)

$$\begin{aligned} \left\langle \Phi_{\boldsymbol{s}'}^{\boldsymbol{k}}\middle|\hat{B}\middle|\Phi_{\boldsymbol{s}}^{\boldsymbol{k}}\right\rangle &= \left\langle \Phi_{\boldsymbol{s}'}^{\boldsymbol{k}}\middle|\theta^{-1}\theta\hat{B}\theta^{-1}\theta\middle|\Phi_{\boldsymbol{s}}^{\boldsymbol{k}}\right\rangle \\ &= \left(D_{s'}^{\Phi\theta+}\left\langle \Phi_{\boldsymbol{s}'}^{-\boldsymbol{k}}\middle|\hat{B}\middle|\Phi_{\boldsymbol{s}}^{-\boldsymbol{k}}\right\rangle D_s^{\Phi\theta} D^{B\theta}\right)^*. \end{aligned} \tag{B22}$$

If the operation is a product θg this gets modified by carefully inserting Eq. (B20) for $-\boldsymbol{k}$ into Eq. (B22) which is not spelled out due to the unwieldy phase factors. Essentially we let $D^{\Phi} \rightarrow D^{\Phi} D^{\Phi\theta}$, $D^{B} \rightarrow D^{B} D^{\Phi\theta}$ and $\alpha\boldsymbol{k} \rightarrow -\alpha\boldsymbol{k}$ in Eq. (B20) and apply complex conjugation to the whole rhs.

In order to symmetrize the matrix elements when needed we make use of the fact that the sum of the rhs of Eq. (B14) over all group operations divided by the number of group elements is a projector. So, for all pairs of lattice sites we perform this sum over all transformed pairs. In case if time reversal is contained in the operation the corresponding formulas Eq. (B16) or a mix of this with Eq. (B14) must be used.

On a final note, in relativistic case the ambiguity of choosing the rotation or rotation $+\,2\pi$ as pointgroup part of g cancels out in all formulas which transform matrix elements, since they are bilinear in the orbitals.

3. Bloch theorem

Equation (B17) can be specialized to pure translations by using $\alpha = 1$, $\boldsymbol{\tau} = \boldsymbol{R}$ i.e., $g = \{E|\boldsymbol{R}\}$ for which $g\boldsymbol{s} = \boldsymbol{s} + \boldsymbol{R}$ and $D^{\Phi}_{s}(\alpha) = 1$, which gives the Bloch theorem

$$T_{\boldsymbol{R}} \Phi^{\boldsymbol{k}}_{s} = \Phi^{\boldsymbol{k}}_{s} \mathrm{e}^{-i\boldsymbol{k}\boldsymbol{R}}, \tag{B23}$$

which can be applied to matrix elements of translational invariant operators Eq. (B11) between Bloch sums Eq. (A4) of different $\boldsymbol{k}$ vectors (the most general case) to get (dropping all nonessential indices)

$$\begin{aligned} \langle \Phi^{\boldsymbol{q}} | \hat{B} | \Phi^{\boldsymbol{k}} \rangle &= \langle T_{\boldsymbol{R}} \Phi^{\boldsymbol{q}} | T_{\boldsymbol{R}} \hat{B} T_{\boldsymbol{R}}^{-1} | T_{\boldsymbol{R}} \Phi^{\boldsymbol{k}} \rangle \\ &= \langle \Phi^{\boldsymbol{q}} | \hat{B} | \Phi^{\boldsymbol{k}} \rangle \mathrm{e}^{-i(\boldsymbol{k}-\boldsymbol{q})\boldsymbol{R}}. \end{aligned} \tag{B24}$$

For $\boldsymbol{q} \neq \boldsymbol{k}$ in the first BZ, the phase cannot become one and hence

$$\langle \Phi^{\boldsymbol{q}} | \hat{B} | \Phi^{\boldsymbol{k}} \rangle = \delta_{\boldsymbol{q},\boldsymbol{k}} \langle \Phi^{\boldsymbol{k}} | \hat{B} | \Phi^{\boldsymbol{k}} \rangle. \tag{B25}$$

For the position operator which fulfills

$$T_{\boldsymbol{R}} \boldsymbol{r} T_{\boldsymbol{R}}^{-1} = \boldsymbol{r} - \boldsymbol{R}, \tag{B26}$$

Eq. (B24) becomes

$$\langle \Phi^{\boldsymbol{q}} | \boldsymbol{r} | \Phi^{\boldsymbol{k}} \rangle = (\langle \Phi^{\boldsymbol{q}} | \boldsymbol{r} | \Phi^{\boldsymbol{k}} \rangle - \delta_{\boldsymbol{q}\boldsymbol{k}} S^{\boldsymbol{k}} \boldsymbol{R}) \mathrm{e}^{-i(\boldsymbol{k}-\boldsymbol{q})\boldsymbol{R}}, \tag{B27}$$

which specializes to

$$\langle \Phi^{\boldsymbol{k}} | \boldsymbol{r} | \Phi^{\boldsymbol{k}} \rangle = \langle \Phi^{\boldsymbol{k}} | \boldsymbol{r} | \Phi^{\boldsymbol{k}} \rangle - S^{\boldsymbol{k}} \boldsymbol{R} \tag{B28}$$

for the $\boldsymbol{k}$-diagonal terms, which shows that the limit $\boldsymbol{q} \rightarrow \boldsymbol{k}$ is badly defined and that the operator is essentially $\boldsymbol{k}$-nondiagonal.

The Berry operator Eq. (28) transforms like the position operator itself:

$$\begin{aligned} T_{\boldsymbol{R}} \boldsymbol{\beta}_{\boldsymbol{k}} T_{\boldsymbol{R}}^{-1} &= \mathrm{e}^{i\boldsymbol{k}\boldsymbol{r}} \mathrm{e}^{-i\boldsymbol{k}\boldsymbol{R}} i\nabla_{\boldsymbol{k}} \mathrm{e}^{-i\boldsymbol{k}\boldsymbol{r}} \mathrm{e}^{i\boldsymbol{k}\boldsymbol{R}} \\ &= \mathrm{e}^{i\boldsymbol{k}\boldsymbol{r}} i\nabla_{\boldsymbol{k}} \mathrm{e}^{-i\boldsymbol{k}\boldsymbol{r}} + \mathrm{e}^{-i\boldsymbol{k}\boldsymbol{R}} (i\nabla_{\boldsymbol{k}} \mathrm{e}^{i\boldsymbol{k}\boldsymbol{R}}) \\ &= \boldsymbol{\beta}_{\boldsymbol{k}} - \boldsymbol{R}, \end{aligned}$$

which then gives

$$\begin{aligned} T_{\boldsymbol{R}} | \boldsymbol{\beta}_{\boldsymbol{k}} \Phi^{\boldsymbol{k}} \rangle &= \left| T_{\boldsymbol{R}} \boldsymbol{\beta}_{\boldsymbol{k}} T_{\boldsymbol{R}}^{-1} T_{\boldsymbol{R}} \Phi^{\boldsymbol{k}} \right\rangle \\ &= | (\boldsymbol{\beta}_{\boldsymbol{k}} - \boldsymbol{R}) \Phi^{\boldsymbol{k}} \mathrm{e}^{-i\boldsymbol{k}\boldsymbol{R}} \rangle \\ &= | \boldsymbol{\beta}_{\boldsymbol{k}} \Phi^{\boldsymbol{k}} \mathrm{e}^{-i\boldsymbol{k}\boldsymbol{R}} \rangle - | \Phi^{\boldsymbol{k}} \rangle \mathrm{e}^{-i\boldsymbol{k}\boldsymbol{R}} \boldsymbol{R}. \end{aligned}$$

Applying Eq. (29a) to the first term of the rhs yields

$$T_{\boldsymbol{R}} | \boldsymbol{\beta}_{\boldsymbol{k}} \Phi^{\boldsymbol{k}} \rangle = | \boldsymbol{\beta}_{\boldsymbol{k}} \Phi^{\boldsymbol{k}} \rangle \mathrm{e}^{-i\boldsymbol{k}\boldsymbol{R}} \tag{B29}$$

and hence Eqs. (B24) and (B25) apply and $\boldsymbol{\beta}_{\boldsymbol{k}}$ is $\boldsymbol{k}$-diagonal.

4. Berry connection/curvature

The transformation of the vector valued functions Eq. (38) is obtained by using Eq. (B9) and $gf(\boldsymbol{r}) = f(g^{-1}\boldsymbol{r})$ as in Eq. (B10) which results in $(g^{-1}\boldsymbol{r} - \boldsymbol{R} - \boldsymbol{s}) = (\boldsymbol{r} - \alpha\boldsymbol{R} - g\boldsymbol{s})\alpha$ for the $\boldsymbol{r}$ factor and hence in

$$g(\boldsymbol{r}\Phi)_{\boldsymbol{R}\boldsymbol{s}} = (\boldsymbol{r}\Phi)_{g(\boldsymbol{R}\boldsymbol{s})} D^{\Phi}_{s}(\alpha)\alpha, \tag{B30}$$

where the last α acts on the vector structure. Hence, the reduced position operator matrix elements Eq. (43) transform as Eq. (B14) with $D^{B} \rightarrow \alpha$, i.e., as LO matrix elements in the orbital indices and as a polar vector in the position operator indices. Bloch sums of Eq. (B30) lead to the transformation of Eq. (42) according to

$$\langle \Phi^{\boldsymbol{k}} | (\boldsymbol{r}\Phi)^{\boldsymbol{k}} \rangle = D^{\Phi\boldsymbol{k}+} \langle \Phi^{\alpha\boldsymbol{k}} | (\boldsymbol{r}\Phi)^{\alpha\boldsymbol{k}} \rangle D^{\Phi\boldsymbol{k}} \alpha \tag{B31}$$

with $D^{\Phi\boldsymbol{k}}$ from Eq. (B18).

Equations (41) and (B31) then lead to

$$\boldsymbol{A}^{\boldsymbol{k}}_{\Phi} - \overline{\lambda} S^{\boldsymbol{k}} \boldsymbol{s} = D^{\Phi\boldsymbol{k}+} \big(\boldsymbol{A}^{\alpha\boldsymbol{k}}_{\Phi} - \overline{\lambda} S^{\alpha\boldsymbol{k}} \boldsymbol{s} \big) D^{\Phi\boldsymbol{k}} \alpha, \tag{B32}$$

where $\boldsymbol{s}$ is the diagonal matrix containing the site vectors of the corresponding orbitals. By using Eqs. (B18) and (B20) with $\hat{B} = 1$ this can be transformed into

$$\boldsymbol{A}^{\boldsymbol{k}}_{\Phi} = D^{\Phi\boldsymbol{k}+} \boldsymbol{A}^{\alpha\boldsymbol{k}}_{\Phi} D^{\Phi\boldsymbol{k}} \alpha + \overline{\lambda} S^{\boldsymbol{k}} (\boldsymbol{s} - \boldsymbol{s}_{g}\alpha). \tag{B33}$$

From this, it is clear that for WFs ($S^{\boldsymbol{k}} = 1$) approximation Eq. (46) fulfills the transformation law Eq. (B32) trivially while setting the basis connection to zero $\boldsymbol{A}^{\boldsymbol{k}}_{\Phi} = 0$ will in general not.

Acting with g on $\boldsymbol{r}$ in Eq. (28) and using $\nabla_{\boldsymbol{k}} = \nabla_{\alpha\boldsymbol{k}}\alpha$, we get

$$g \boldsymbol{\beta}_{\boldsymbol{k}} g^{-1} = (\boldsymbol{\beta}_{\alpha\boldsymbol{k}} - \boldsymbol{\tau})\alpha,$$

which allows to derive the general transformation properties of $\boldsymbol{A}^{\boldsymbol{k}}_{\Phi}$ directly when assuming a general law $g\Phi^{\boldsymbol{k}} = \Phi^{\alpha\boldsymbol{k}} D^{\Phi\boldsymbol{k}}$ with some representation matrices $D^{\Phi\boldsymbol{k}}$

$$\begin{aligned} \boldsymbol{A}^{\boldsymbol{k}}_{\Phi} &= \langle \Phi^{\boldsymbol{k}} | \boldsymbol{\beta}_{\boldsymbol{k}} \Phi^{\boldsymbol{k}} \rangle \\ &= \langle \Phi^{\alpha\boldsymbol{k}} D^{\Phi\boldsymbol{k}} | (\boldsymbol{\beta}_{\alpha\boldsymbol{k}} - \boldsymbol{\tau}) \alpha \Phi^{\alpha\boldsymbol{k}} D^{\Phi\boldsymbol{k}} \rangle \\ &= \langle \Phi^{\alpha\boldsymbol{k}} D^{\Phi\boldsymbol{k}} | (\boldsymbol{\beta}_{\alpha\boldsymbol{k}} \alpha \Phi^{\alpha\boldsymbol{k}}) D^{\Phi\boldsymbol{k}} + \Phi^{\alpha\boldsymbol{k}} i\nabla_{\alpha\boldsymbol{k}} \alpha D^{\Phi\boldsymbol{k}} \rangle - S^{\boldsymbol{k}}_{\Phi} \boldsymbol{\tau} \alpha \\ &= \langle \Phi^{\alpha\boldsymbol{k}} D^{\Phi\boldsymbol{k}} | \boldsymbol{\beta}_{\alpha\boldsymbol{k}} \alpha \Phi^{\alpha\boldsymbol{k}} \rangle D^{\Phi\boldsymbol{k}} + D^{\Phi\boldsymbol{k}+} S^{\alpha\boldsymbol{k}}_{\Phi} i\nabla_{\boldsymbol{k}} D^{\Phi\boldsymbol{k}} - S^{\boldsymbol{k}}_{\Phi} \boldsymbol{\tau} \alpha \\ &= D^{\Phi\boldsymbol{k}+} \big(\boldsymbol{A}^{\alpha\boldsymbol{k}}_{\Phi} \alpha + S^{\alpha\boldsymbol{k}}_{\Phi} i\nabla_{\boldsymbol{k}} \big) D^{\Phi\boldsymbol{k}} - S^{\boldsymbol{k}}_{\Phi} \boldsymbol{\tau} \alpha, \end{aligned} \tag{B34}$$

which specializes to Eq. (B33) by inserting the gradient of Eq. (B18), in other words the local basis connection transforms as a general Berry connection matrix would.

Now, we introduce the basis change $\Psi^{\boldsymbol{k}} = w^{\boldsymbol{k}} C^{\boldsymbol{k}}$, which leads to the Berry connection matrix Eq. (54a). Then we can show that if $\boldsymbol{A}^{\boldsymbol{k}}_{w}$ transforms as Eq. (B34) with $\Phi \rightarrow w$, also $\boldsymbol{A}^{\boldsymbol{k}}_{\Psi}$ [Eq. (54a)] transforms like Eq. (B34) with $\Phi \rightarrow \Psi$. Using the abbreviations $b^{\boldsymbol{k}} \rightarrow b$, $b^{\alpha\boldsymbol{k}} \rightarrow b^{\alpha}$, and $C^{+}bC \rightarrow \langle b \rangle_{C}$, one gets the transformation properties of Ψ, w, and C

$$\begin{aligned} gw &= w^{\alpha} D^{w}, \quad & \Psi &= wC, \\ g\Psi &= \Psi^{\alpha} D^{\Psi}, \quad & D^{w} C &= C^{\alpha} D^{\Psi}, \end{aligned}$$

and

$$\begin{aligned}\langle S_w^\alpha i\nabla\rangle_{D^wC} &= \langle\langle S_w^\alpha i\nabla\rangle_{D^w}\rangle_C + \langle\langle S_w^\alpha\rangle_{D^w} i\nabla\rangle_C\\ &= \langle\langle S_w^\alpha i\nabla\rangle_{D^w}\rangle_C + \langle S_w i\nabla\rangle_C,\end{aligned}\tag{B35}$$

which leads to

$$\begin{aligned}\boldsymbol{A}_w &= \langle\boldsymbol{A}_w^\alpha\alpha\rangle_{D^w} + \langle S_w^\alpha i\nabla\rangle_{D^w} - S_w\boldsymbol{\tau}\alpha,\ \text{Eq. (B34)};\\ \boldsymbol{A}_\Psi &= \langle\boldsymbol{A}_w\rangle_C + \langle S_w i\nabla\rangle_C\ [\text{Eq. (B54a)}]\\ &= \langle\langle\boldsymbol{A}_w^\alpha\alpha\rangle_{D^w}\rangle_C + \langle\langle S_w^\alpha i\nabla\rangle_{D^w}\rangle_C - S_\Psi\boldsymbol{\tau}\alpha + \langle S_w i\nabla\rangle_C\\ &= \langle\boldsymbol{A}_w^\alpha\alpha\rangle_{D^wC} + \langle S_w^\alpha i\nabla\rangle_{D^wC} - S_\Psi\boldsymbol{\tau}\alpha\\ &= \langle\boldsymbol{A}_w^\alpha\alpha\rangle_{C^\alpha D^\Psi} + \langle S_w^\alpha i\nabla\rangle_{C^\alpha D^\Psi} - S_\Psi\boldsymbol{\tau}\alpha\\ &= \langle\boldsymbol{A}_w^\alpha\alpha\rangle_{C^\alpha D^\Psi} + \langle\langle S_w^\alpha i\nabla\rangle_{C^\alpha}\rangle_{D^\Psi} + \langle\langle S_w^\alpha\rangle_{C^\alpha} i\nabla\rangle_{D^\Psi} - S_\Psi\boldsymbol{\tau}\alpha\\ &= \langle\boldsymbol{A}_\Psi^\alpha\alpha\rangle_{D^\Psi} + \langle S_\Psi^\alpha i\nabla\rangle_{D^\Psi} - S_\Psi\boldsymbol{\tau}\alpha.\end{aligned}\tag{B36}$$

Of course, usually Wannier and eigenfunctions are orthonormal, which means $S_{w,\Psi} = 1$. Equation (B36) explicitly shows that the basis change again leads to the generic transformation law Eq. (B34). All we need to show now is that this law leads to the proper transformation behavior of the curvature.

We start with the cross-product term, which we write in its most general form (including the correction for nonorthonormal Ψ) using Eq. (B36)

$$i\boldsymbol{A}_\Psi^+\frac{1}{S_\Psi}\times\boldsymbol{A}_\Psi = (\boldsymbol{a} - S_\Psi\boldsymbol{\tau}\alpha)^+\frac{1}{S_\Psi}\times(\boldsymbol{a} - S_\Psi\boldsymbol{\tau}\alpha)\tag{B37}$$

with $\boldsymbol{a} = \boldsymbol{A}_\Psi + S_\Psi\boldsymbol{\tau}\alpha = \langle\boldsymbol{A}_\Psi^\alpha\alpha\rangle_{D^\Psi} + \langle S_\Psi^\alpha i\nabla\rangle$. Using the fact that $\boldsymbol{\tau}\alpha$ is constant diagonal in matrix space and hence commutes with any matrix one gets $(\boldsymbol{\tau}\alpha)\times S_\Psi(\boldsymbol{\tau}\alpha) = 0$ and $\boldsymbol{a}\times(\boldsymbol{\tau}\alpha) + (\boldsymbol{\tau}\alpha)\times\boldsymbol{a} = 0$. Furthermore, Eq. (35) gives $\boldsymbol{a}^+ = \boldsymbol{a} - i\nabla S_\Psi$ and hence $\boldsymbol{a}^+\times\boldsymbol{\tau}\alpha + \boldsymbol{\tau}\alpha\times\boldsymbol{a} = -(i\nabla S_\Psi)\times\boldsymbol{\tau}\alpha$. which ultimately yields

$$i\boldsymbol{A}_\Psi^+\frac{1}{S_\Psi}\times\boldsymbol{A}_\Psi = i\boldsymbol{a}^+\frac{1}{S_\Psi}\times\boldsymbol{a} - (\nabla S_\Psi)\times(\boldsymbol{\tau}\alpha).\tag{B38}$$

Next the transformation of Ψ yields $S_\Psi = D^{\Psi+}S_\Psi^\alpha D^\Psi$ and since all matrices are invertable also

$$1 = D^\Psi\frac{1}{S_\Psi}D^{\Psi+}S_\Psi^\alpha,$$

which by insertion gives

$$\begin{aligned}i\nabla D^\Psi &= D^\Psi\frac{1}{S_\Psi}D^{\Psi+}S_\Psi^\alpha i\nabla D^\Psi\\ &= D^\Psi\frac{1}{S_\Psi}\langle S_\Psi^\alpha i\nabla\rangle_{D^\Psi}.\end{aligned}\tag{B39}$$

Furthermore, for any two vector valued quantities $(\boldsymbol{b}\alpha)\times(\boldsymbol{c}\alpha) = (\boldsymbol{b}\times\boldsymbol{c})\overline{\alpha}$ holds, where $\overline{\alpha} = I\alpha$ if the point group operation is improper and α otherwise. The gradient transforms as $\nabla_{\alpha\boldsymbol{k}}\alpha = \nabla_{\boldsymbol{k}}$, which leads to $\nabla\times\boldsymbol{A}_\Psi^\alpha\alpha = (\nabla_\alpha\times\boldsymbol{A}_\Psi^\alpha)\overline{\alpha}$ and with Eqs. (B39)

$$\begin{aligned}&\nabla\times\langle\boldsymbol{A}_\Psi^\alpha\alpha\rangle_{D^\Psi}\\ &= \langle(\nabla_\alpha\times\boldsymbol{A}_\Psi^\alpha)\overline{\alpha}\rangle_{D^\Psi} + i\langle S_\Psi^\alpha i\nabla\rangle_{D^\Psi}^+\frac{1}{S_\Psi}\times\langle\boldsymbol{A}_\Psi^\alpha\alpha\rangle_{D^\Psi}\\ &\quad + i\langle\boldsymbol{A}_\Psi^\alpha\alpha\rangle_{D^\Psi}\frac{1}{S_\Psi}\times\langle S_\Psi^\alpha i\nabla\rangle_{D^\Psi}.\end{aligned}\tag{B40}$$

Also, by differentiation and Eqs. (B39)

$$\nabla\times\langle S_\Psi^\alpha i\nabla\rangle_{D^\Psi} = i(\langle S_\Psi^\alpha i\nabla\rangle_{D^\Psi}^+ - \langle(i\nabla S_\Psi^\alpha)\rangle_{D^\Psi})\frac{1}{S_\Psi}\langle S_\Psi^\alpha i\nabla\rangle_{D^\Psi}.\tag{B41}$$

Equations (35), (B40), and (B41) then yield the curl of Eq. (B36) after some term sorting

$$\begin{aligned}\nabla\times\boldsymbol{A}_\Psi &= \langle(\nabla_\alpha\times\boldsymbol{A}_\Psi^\alpha)\overline{\alpha}\rangle_{D^\Psi} - i\langle\boldsymbol{A}_\Psi^\alpha\alpha\rangle_{D^\Psi}^+\frac{1}{S_\Psi}\times\langle\boldsymbol{A}_\Psi^\alpha\alpha\rangle_{D^\Psi}\\ &\quad + i\boldsymbol{a}^+\frac{1}{S_\Psi}\times\boldsymbol{a} - (\nabla S_\Psi)\times(\boldsymbol{\tau}\alpha),\end{aligned}\tag{B42}$$

which together with Eq. (B38) results in

$$\begin{aligned}\nabla\times\boldsymbol{A}_\Psi &= \langle(\nabla_\alpha\times\boldsymbol{A}_\Psi^\alpha)\overline{\alpha}\rangle_{D^\Psi} - i\langle\boldsymbol{A}_\Psi^\alpha\alpha\rangle_{D^\Psi}^+\frac{1}{S_\Psi}\times\langle\boldsymbol{A}_\Psi^\alpha\alpha\rangle_{D^\Psi}\\ &\quad + i\boldsymbol{A}_\Psi^+\frac{1}{S_\Psi}\times\boldsymbol{A}_\Psi.\end{aligned}\tag{B43}$$

This is the most general case.

If Ψ is orthonormal and an eigenbasis, the representation matrices D^Ψ are now unitary $D^{\Psi+}D^\Psi = 1$ and block diagonal with blocks for each degenerate subspace and hence the subspace projector P commutes $[D^\Psi, P]_- = 0$ and hence

$$\begin{aligned}Q\langle i\nabla\rangle_{D^\Psi}P &= QD^{\Psi+}i\nabla D^\Psi P\\ &= D^{\Psi+}iQP\nabla D^\Psi\\ &= 0\end{aligned}\tag{B44}$$

and $Q\boldsymbol{a}P = Q\langle\boldsymbol{A}_\Psi^\alpha\alpha\rangle_{D^\Psi}P$ and together Eq. (B38) specializes to

$$\begin{aligned}iP\boldsymbol{A}_\Psi Q\times Q\boldsymbol{A}_\Psi P &= iP\langle\boldsymbol{A}_\Psi^\alpha\alpha\rangle_{D^\Psi}Q\times Q\langle\boldsymbol{A}_\Psi^\alpha\alpha\rangle_{D^\Psi}P\\ &= i\langle P\boldsymbol{A}_\Psi^\alpha\alpha Q\times Q\boldsymbol{A}_\Psi^\alpha\alpha P\rangle_{D^\Psi}\\ &= i\langle P\boldsymbol{A}_\Psi^\alpha Q\times Q\boldsymbol{A}_\Psi^\alpha P\rangle_{D^\Psi}\overline{\alpha},\end{aligned}\tag{B45}$$

which shows that the $A\times A$ term of the non-Abelian Berry curvature alone transforms as a matrix in orbital indices and as pseudo vector in vector indices. Subtracting $iPAP\times PAP$ from Eq. (B43), one finally gets for the full non-Abelian Berry curvature $P\boldsymbol{F}_{nA}P = P(\nabla\times\boldsymbol{A}_\Psi - i\boldsymbol{A}_\Psi P\times P\boldsymbol{A}_\Psi)P$ the expression

$$\boldsymbol{F}_{\Psi nA}^{\boldsymbol{k}} = D^{\Psi\boldsymbol{k}+}\boldsymbol{F}_{\Psi nA}^{\alpha\boldsymbol{k}}D^{\Psi\boldsymbol{k}}\overline{\alpha}.\tag{B46}$$

Now, since both the full curvature as well as the $A\times A$ term transform the same proper way, so also the difference $\langle\boldsymbol{f}\rangle_C - i\langle\boldsymbol{A}\rangle_C Q_i\times Q_i\langle\boldsymbol{A}\rangle_C$ in Eq. (54b) must transform this way.

The discussion of this section shows that the approximation Eq. (46) leads to proper behavior of the connection and hence curvature and consequently, that the leading term $\langle Si\nabla\rangle\times\langle Si\nabla\rangle$ alone cannot transform properly in the periodic gauge.

5. Bloch sum gauge invariance

We show the influence of the Bloch sum gauge choice (λ) on various expressions used in the main text. From Eq. (A4) with $\Phi\to w$, one gets

$$w^{\boldsymbol{k}\lambda} = w^{\boldsymbol{k}\overline{\lambda}}\Lambda^{\boldsymbol{k}},\quad \Lambda^{\boldsymbol{k}} = \mathrm{e}^{i\boldsymbol{k}\boldsymbol{s}(\lambda-\overline{\lambda})},\quad 0 = [\Lambda^{\boldsymbol{k}}, \boldsymbol{s}]_-,\tag{B47}$$

$$S^{\boldsymbol{k}\lambda} = \Lambda^{-\boldsymbol{k}}S^{\boldsymbol{k}\overline{\lambda}}\Lambda^{\boldsymbol{k}}\tag{B48}$$

with $\bar\lambda = 1-\lambda$ and $(\lambda-\bar\lambda)^2 = 1$. Together with $\Psi^{\boldsymbol{k}} = w^{\boldsymbol{k}}C^{\boldsymbol{k}} = w^{\boldsymbol{k}\lambda}C^{\boldsymbol{k}\lambda}$ this leads to

$$C^{\boldsymbol{k}\bar\lambda} = \Lambda^{\boldsymbol{k}}C^{\boldsymbol{k}\lambda}, \tag{B49a}$$

$$1 = C^{\boldsymbol{k}\lambda+}S^{\boldsymbol{k}\lambda}C^{\boldsymbol{k}\lambda} \tag{B49b}$$

$$= C^{\boldsymbol{k}\bar\lambda+}S^{\boldsymbol{k}\bar\lambda}C^{\boldsymbol{k}\bar\lambda} \tag{B49c}$$

and altogether to

$$\begin{aligned}\boldsymbol{A}_w^{\boldsymbol{k}\lambda} &= \Lambda^{-\boldsymbol{k}}\langle w^{\boldsymbol{k}\bar\lambda}|\boldsymbol{\beta}_{\boldsymbol{k}} w^{\boldsymbol{k}\bar\lambda}\Lambda^{\boldsymbol{k}}\rangle\\ &= \Lambda^{-\boldsymbol{k}}\langle w^{\boldsymbol{k}\bar\lambda}|\boldsymbol{\beta}_{\boldsymbol{k}} w^{\boldsymbol{k}\bar\lambda}\rangle\Lambda^{\boldsymbol{k}} + \Lambda^{-\boldsymbol{k}}\langle w^{\boldsymbol{k}\bar\lambda}|w^{\boldsymbol{k}\bar\lambda}\rangle(i\nabla_{\boldsymbol{k}}\Lambda^{\boldsymbol{k}})\\ &= \Lambda^{-\boldsymbol{k}}\boldsymbol{A}_w^{\boldsymbol{k}\bar\lambda}\Lambda^{\boldsymbol{k}} - (\lambda-\bar\lambda)\Lambda^{-\boldsymbol{k}}S_w^{\boldsymbol{k}\bar\lambda}\Lambda^{\boldsymbol{k}}\boldsymbol{s}\\ &= \Lambda^{-\boldsymbol{k}}\boldsymbol{A}_w^{\boldsymbol{k}\bar\lambda}\Lambda^{\boldsymbol{k}} - (\lambda-\bar\lambda)S_w^{\boldsymbol{k}\lambda}\boldsymbol{s}\end{aligned} \tag{B50}$$

so, the basis connection does not transform like a simple operator [as the overlap Eq. (B48)]. Equations (B47), (B49), and (B50) then give

$$\begin{aligned}\langle\boldsymbol{A}\rangle_C^\lambda &= C^{\boldsymbol{k}\lambda+}\boldsymbol{A}_w^{\boldsymbol{k}\lambda}C^{\boldsymbol{k}\lambda}\\ &= C^{\boldsymbol{k}\lambda+}\big[\Lambda^{-\boldsymbol{k}}\boldsymbol{A}_w^{\boldsymbol{k}\bar\lambda}\Lambda^{\boldsymbol{k}} - (\lambda-\bar\lambda)S_w^{\boldsymbol{k}\lambda}\boldsymbol{s}\big]C^{\boldsymbol{k}\lambda}\\ &= C^{\boldsymbol{k}\bar\lambda+}\boldsymbol{A}_w^{\boldsymbol{k}\bar\lambda}C^{\boldsymbol{k}\bar\lambda} - (\lambda-\bar\lambda)C^{\boldsymbol{k}\lambda+}S_w^{\boldsymbol{k}\lambda}\boldsymbol{s}C^{\boldsymbol{k}\lambda}\\ &= \langle\boldsymbol{A}_w\rangle_C^{\bar\lambda} - (\lambda-\bar\lambda)\langle S\boldsymbol{s}\rangle_C^\lambda,\end{aligned} \tag{B51}$$

and in a similar way,

$$\begin{aligned}\langle Si\nabla\rangle_C^\lambda &= C^{\boldsymbol{k}\lambda+}S^{\boldsymbol{k}\lambda}i\nabla_{\boldsymbol{k}}C^{\boldsymbol{k}\lambda}\\ &= C^{\boldsymbol{k}\lambda+}S^{\boldsymbol{k}\lambda}i\nabla_{\boldsymbol{k}}\Lambda^{\boldsymbol{k}+}C^{\boldsymbol{k}\bar\lambda}\\ &= C^{\boldsymbol{k}\lambda+}[S^{\boldsymbol{k}\lambda}\Lambda^{\boldsymbol{k}+}i\nabla_{\boldsymbol{k}} + S^{\boldsymbol{k}\lambda}i(\nabla_{\boldsymbol{k}}\Lambda^{\boldsymbol{k}+})]C^{\boldsymbol{k}\bar\lambda}\\ &= \langle Si\nabla\rangle_C^{\bar\lambda} + (\lambda-\bar\lambda)\langle S\boldsymbol{s}\rangle_C^\lambda.\end{aligned} \tag{B52}$$

Consequently, Eqs. (49) and (50) are not invariant under gauge change of the Bloch sums, even though they are expressions in the eigenbasis. However, their sum and hence the Berry connection matrix in eigenbasis Eq. (54a) and the $\boldsymbol{A}\times\boldsymbol{A}$ term in Eq. (54b) are invariant. In the following, we drop the $\boldsymbol{k}$ index for simplification. The gradient of Eq. (B48) then reads

$$\nabla S^\lambda = \Lambda^+(\nabla S^{\bar\lambda} + i(\lambda-\bar\lambda)[S^{\bar\lambda},\boldsymbol{s}]_-)\Lambda. \tag{B53}$$

The curl of the basis connection together with Eqs. (B50) and (35) and $S\boldsymbol{s}\times\boldsymbol{s} = 0$ then reads

$$\begin{aligned}\nabla\times\boldsymbol{A}_w^\lambda &= \nabla\times\big(\Lambda^+\boldsymbol{A}_w^{\bar\lambda}\Lambda\big) - (\lambda-\bar\lambda)\big(\nabla S_w^\lambda\big)\times\boldsymbol{s}\\ &= \Lambda^+\big(\nabla\times\boldsymbol{A}_w^{\bar\lambda}\big)\Lambda\\ &\quad - i\Lambda^+(\lambda-\bar\lambda)\big(\boldsymbol{s}\times\boldsymbol{A}_w^{\bar\lambda} + \boldsymbol{A}_w^{\bar\lambda+}\times\boldsymbol{s}\big)\Lambda\\ &\quad + \Lambda^+(i\boldsymbol{s}S^{\bar\lambda}\times\boldsymbol{s})\Lambda,\end{aligned} \tag{B54}$$

which bracketed between $C^{\boldsymbol{k}}$, by inserting $CC^+S = 1$ where needed and using Eq. (B49a), gives

$$\begin{aligned}\langle\nabla\times\boldsymbol{A}_w\rangle_C^\lambda &= \langle\nabla\times\boldsymbol{A}_w\rangle_C^{\bar\lambda} - i(\lambda-\bar\lambda)\langle(\boldsymbol{s}\times\boldsymbol{A}_w + \boldsymbol{A}_w^+\times\boldsymbol{s})\rangle_C^{\bar\lambda}\\ &\quad + i\langle\boldsymbol{s}S\times\boldsymbol{s}\rangle_C^{\bar\lambda}.\end{aligned} \tag{B55}$$

Finally, $\langle S\boldsymbol{s}\rangle_C^\lambda = \langle S\boldsymbol{s}\rangle_C^{\bar\lambda}$ and application of $CC^+S = 1$ and Eq. (B51) yields

$$\begin{aligned}\langle\boldsymbol{A}\rangle_C^{\lambda+}\times\langle\boldsymbol{A}\rangle_C^\lambda &= \langle\boldsymbol{A}_w\rangle_C^{\bar\lambda+}\times\langle\boldsymbol{A}_w\rangle_C^{\bar\lambda}\\ &\quad - (\lambda-\bar\lambda)\langle\boldsymbol{s}\times\boldsymbol{A}_w + \boldsymbol{A}_w^+\times\boldsymbol{s}\rangle_C^{\bar\lambda}\\ &\quad + \langle\boldsymbol{s}S\times\boldsymbol{s}\rangle_C^{\bar\lambda}\end{aligned} \tag{B56}$$

from which follows

$$\begin{aligned}&\langle\boldsymbol{f}\rangle_C^\lambda - i\langle\boldsymbol{A}_w\rangle_C^{\lambda+}\times\langle\boldsymbol{A}_w\rangle_C^\lambda\\ &\quad = \langle\boldsymbol{f}\rangle_C^{\bar\lambda} - i\langle\boldsymbol{A}_w\rangle_C^{\bar\lambda+}\times\langle\boldsymbol{A}_w\rangle_C^{\bar\lambda},\end{aligned} \tag{B57}$$

and hence the full Berry connection Eq. (54b) is invariant too.

APPENDIX C: CRYSTAL STRUCTURES

1. CaCuO2

CaCuO2 forms a tetragonal lattice with spacegroup 123 (P4/mmm). We used lattice parameters $a_0 = 7.29434a_\mathrm{B}$ and $c_0 = 6.04712a_\mathrm{B}$ with Wyckoff positions: Ca at $1d = (\frac{1}{2}\frac{1}{2}\frac{1}{2})$, Cu at $1a = (000)$ and O at $2f = (\frac{1}{2}00)$. We performed a non-spin-polarized calculation in scalar relativistic mode within the local (spin) density approximation L(S)DA [36] (PW92) in FPLO version 19.00-60. The self-consistent $\boldsymbol{k}$ mesh contains 12^3 points in the primitive reciprocal unit cell.

2. bcc Fe

We performed a full relativistic spin polarized calculation for bcc iron with space group 229 (Im$\bar3$m), Wyckoff position $2a = (000)$ and lattice parameter $a_0 = 5.4a_\mathrm{B}$ in FPLO version 19.00-60. The exchange and correlation functional is LSDA (PW92) and the magnetization axis is (001) with resulting spin moment of $2.19\mu_\mathrm{B}$. The self consistent $\boldsymbol{k}$ mesh contains 16^3 points in the primitive reciprocal unit cell.

3. B2 FeAl

We performed a full relativistic spin polarized calculation for B2 FeAl with space group 221 (Pm$\bar3$m) with Fe at Wyckoff position $1a = (000)$ and Al at $1b = (\frac{1}{2}\frac{1}{2}\frac{1}{2})$ and lattice parameter $a_0 = 5.364a_\mathrm{B}$ in FPLO version 19.00-60. The exchange and correlation functional is LSDA (PW92) and the magnetization axis is (001) with resulting spin moment of $0.662\mu_\mathrm{B}$. The self consistent $\boldsymbol{k}$ mesh contains 12^3 points in the primitive reciprocal unit cell.

4. HgS

We performed a full relativistic non-spin-polarized calculation for HgS with space group 216 (F$\bar4$3m) with Hg at Wyckoff position $4a = (000)$ and S at $4c = (\frac{1}{4}\frac{1}{4}\frac{1}{4})$ and lattice parameter $a_0 = 5.85a_\mathrm{B}$ in FPLO version 19.00-60. The exchange and correlation functional is LSDA (PW92). The self consistent $\boldsymbol{k}$ mesh contains 12^3 points in the primitive reciprocal unit cell.

5. MgB_2

We performed a scalar relativistic non-spin-polarized calculation for MgB_2 with space group 191 (P6/mmm) with Mg at Wyckoff position $1a = (000)$ and B at $2d = (\frac{1}{3}\frac{2}{3}\frac{1}{2})$ and lattice parameters $a_0 = 3.078a_\mathrm{B}$, $c_0 = 3.552a_\mathrm{B}$ in FPLO version 19.00-60. The exchange and correlation functional is LSDA (PW92). The self consistent $\boldsymbol{k}$ mesh contains 12^3 points in the primitive reciprocal unit cell.

6. H_2O

We performed a scalar relativistic non-spin-polarized calculation for H_2O in the group $Pmm2$ with H at Wyckoff position $2e = (1.457, 0, 1.127)a_\mathrm{B}$ and O at $1a = (000)$ in FPLO version 19.00-60 within LDA (PW92).

For completeness, we give the WF model Hamiltonian

$$H = \begin{pmatrix} h_{2s} & h_{2s,2p_z} & h_{2s,1s} & h_{2s,1s} \\ h_{2s,2p_z} & h_{2p_z} & h_{2p_z,1s} & h_{2p_z,1s} \\ h_{2s,1s} & h_{2p_z,1s} & h_{1s} & h_{1s,1s} \\ h_{2s,1s} & h_{2p_z,1s} & h_{1s,1s} & h_{1s} \end{pmatrix} \tag{C1}$$

with parameters are $h_{2s} = -18.9547$, $h_{2s,2p_z} = 1.6832$, $h_{2p_z} = -8.3644$, $h_{2s,1s} = 6.5549$, $h_{2p_z,1s} = -2.9232$, $h_{1s} = -8.9814$, and $h_{1s,1s} = 3.5277$ and a subset of the DFT eigenenergies

$$E = \begin{pmatrix} -24.398 & \\ -12.509 & \\ -8.6791 & \\ -6.6177 & \mathrm{O}2p_y \text{ omitted} \\ 0.3046 & \end{pmatrix}. \tag{C2}$$

7. Related citations

For the interested reader, we give an (incomplete) list of recent publications, which used the FPLO Wannier function module [92–105].

[1] I. Sodemann and L. Fu, Phys. Rev. Lett. **115**, 216806 (2015).

[2] N. Marzari and D. Vanderbilt, Phys. Rev. B **56**, 12847 (1997).

[3] I. Souza, N. Marzari, and D. Vanderbilt, Phys. Rev. B **65**, 035109 (2001).

[4] G. Pizzi, V. Vitale, R. Arita, S. Blügel, F. Freimuth, G. Géranton, M. Gibertini, D. Gresch, C. Johnson, T. Koretsune, J. Ibañez-Azpiroz, H. Lee, J.-M. Lihm, D. Marchand, A. Marrazzo, Y. Mokrousov, J. I. Mustafa, Y. Nohara, Y. Nomura, L. Paulatto *et al.*, J. Phys.: Condens. Matter **32**, 165902 (2020).

[5] R. Sakuma, Phys. Rev. B **87**, 235109 (2013).

[6] R. Wang, Phys. Rev. B **90**, 165125 (2014).

[7] W. Ku, H. Rosner, W. E. Pickett, and R. T. Scalettar, Phys. Rev. Lett. **89**, 167204 (2002).

[8] K. Koepernik and H. Eschrig, Phys. Rev. B **59**, 1743 (1999).

[9] H. Eschrig and K. Koepernik, Phys. Rev. B **80**, 104503 (2009).

[10] B. Sporkmann and H. Bross, Phys. Rev. B **49**, 10869 (1994).

[11] X. Qian, J. Li, L. Qi, C.-Z. Wang, T.-L. Chan, Y.-X. Yao, K.-M. Ho, and S. Yip, Phys. Rev. B **78**, 245112 (2008).

[12] N. Marzari, A. A. Mostofi, J. R. Yates, I. Souza, and D. Vanderbilt, Rev. Mod. Phys. **84**, 1419 (2012).

[13] V. P. Smirnov and D. E. Usvyat, Phys. Rev. B **64**, 245108 (2001).

[14] E. I. Blount, Formalisms of band theory, in *Solid State Physics*, edited by Frederick Seitz and David Turnbull (Academic Press, New York, 1962), vol. 13, pp. 305–373.

[15] M.-C. Chang and Q. Niu, Phys. Rev. B **53**, 7010 (1996).

[16] N. Nagaosa, J. Sinova, S. Onoda, A. H. MacDonald, and N. P. Ong, Rev. Mod. Phys. **82**, 1539 (2010).

[17] J. R. Yates, X. Wang, D. Vanderbilt, and I. Souza, Phys. Rev. B **75**, 195121 (2007).

[18] B. Bradlyn, L. Elcoro, J. Cano, M. G. Vergniory, Z. Wang, C. Felser, M. I. Aroyo, and B. A. Bernevig, Nature (London) **547**, 298 (2017).

[19] D. Vanderbilt, *Berry Phases in Electronic Structure Theory* (Cambridge University Press, 2018).

[20] R. D. King-Smith and D. Vanderbilt, Phys. Rev. B **47**, 1651 (1993).

[21] X. Wang, J. R. Yates, I. Souza, and D. Vanderbilt, Phys. Rev. B **74**, 195118 (2006).

[22] D. Culcer, Y. Yao, and Q. Niu, Phys. Rev. B **72**, 085110 (2005).

[23] M. P. López-Sancho, J. M. López-Sancho, and J. Rubio, J. Phys. F: Met. Phys. **14**, 1205 (1984).

[24] M. P. López-Sancho, J. M. López-Sancho, and J. Rubio, J. Phys. F **15**, 851 (1985).

[25] K. Koepernik, D. Kasinathan, D. V. Efremov, S. Khim, S. Borisenko, B. Büchner, and J. van den Brink, Phys. Rev. B **93**, 201101(R) (2016).

[26] T. Fukui, Y. Hatsugai, and H. Suzuki, J. Phys. Soc. Jpn. **74**, 1674 (2005).

[27] R. Yu, X. L. Qi, A. Bernevig, Z. Fang, and X. Dai, Phys. Rev. B **84**, 075119 (2011).

[28] A. A. Soluyanov and D. Vanderbilt, Phys. Rev. B **83**, 235401 (2011).

[29] M. Legner, A. Rüegg, and M. Sigrist, Phys. Rev. B **89**, 085110 (2014).

[30] J. I. Facio, S. K. Das, Y. Zhang, K. Koepernik, J. van den Brink, and I. C. Fulga, Phys. Rev. Mater. **3**, 074202 (2019).

[31] S. Borisenko, D. Evtushinsky, Q. Gibson, A. Yaresko, K. Koepernik, T. Kim, M. Ali, J. van den Brink, M. Hoesch, A. Fedorov, E. Haubold, Y. Kushnirenko, I. Soldatov, R. Schäfer, and R. J. Cava, Nat. Commun. **10**, 3424 (2019).

[32] S. Khim, K. Koepernik, D. V. Efremov, J. Klotz, T. Förster, J. Wosnitza, M. I. Sturza, S. Wurmehl, C. Hess, J. van den Brink, and B. Büchner, Phys. Rev. B **94**, 165145 (2016).

[33] A. A. Mostofi, J. R. Yates, Y.-S. Lee, I. Souza, D. Vanderbilt, and N. Marzari, Comput. Phys. Commun. **178**, 685 (2008).

[34] A. A. Mostofi, J. R. Yates, G. Pizzi, Y.-S. Lee, I. Souza, D. Vanderbilt, and N. Marzari, Comput. Phys. Commun. **185**, 2309 (2014).

[35] P. Giannozzi, O. Baseggio, P. Bonfá, D. Brunato, R. Car, I. Carnimeo, C. Cavazzoni, S. de Gironcoli, P. Delugas, F. F. Ruffino, A. Ferretti, N. Marzari, I. Timrov, A. Urru, and S. Baroni, J. Chem. Phys. **152**, 154105 (2020).

[36] J. P. Perdew and Y. Wang, Phys. Rev. B **45**, 13244 (1992).

[37] A. M. Rappe, K. M. Rabe, E. Kaxiras, and J. D. Joannopoulos, Phys. Rev. B **41**, 1227 (1990).

[38] A. Dal Corso, Comput. Mater. Sci. **95**, 337 (2014).

[39] P. E. Blöchl, Phys. Rev. B **50**, 17953 (1994).

[40] D. Xiao, Y. Yao, Z. Fang, and Q. Niu, Phys. Rev. Lett. **97**, 026603 (2006).

[41] H.-L. Huang, J.-C. Tung, and G.-Y. Guo, Phys. Rev. B **91**, 134409 (2015).

[42] K. Hamaya, N. Hashimoto, S. Oki, S. Yamada, M. Miyao, and T. Kimura, Phys. Rev. B **85**, 100404(R) (2012).

[43] D. Bombor, C. G. F. Blum, O. Volkonskiy, S. Rodan, S. Wurmehl, C. Hess, and B. Büchner, Phys. Rev. Lett. **110**, 066601 (2013).

[44] P. Dheer, Phys. Rev. **156**, 637 (1967).

[45] X. Wang, D. Vanderbilt, J. R. Yates, and I. Souza, Phys. Rev. B **76**, 195109 (2007).

[46] E. Roman, Y. Mokrousov, and I. Souza, Phys. Rev. Lett. **103**, 097203 (2009).

[47] Q. Wang, S. Sun, X. Zhang, F. Pang, H. Lei *et al.*, Phys. Rev. B **94**, 075135 (2016).

[48] L. Ye, M. Kang, J. Liu, F. Von Cube, C. R. Wicker, T. Suzuki, C. Jozwiak, A. Bostwick, E. Rotenberg, D. C. Bell *et al.*, Nature (London) **555**, 638 (2018).

[49] E. Liu, Y. Sun, N. Kumar, L. Muechler, A. Sun, L. Jiao, S.-Y. Yang, D. Liu, A. Liang, Q. Xu *et al.*, Nat. Phys. **14**, 1125 (2018).

[50] J. Noky, Y. Zhang, J. Gooth, C. Felser, and Y. Sun, npj Comput. Mater. **6**, 77 (2020).

[51] K. Kim, J. Seo, E. Lee, K.-T. Ko, B. Kim, B. G. Jang, J. M. Ok, J. Lee, Y. J. Jo, W. Kang *et al.*, Nat. Mater. **17**, 794 (2018).

[52] I.-M. Imort, P. Thomas, G. Reiss, and A. Thomas, J. Appl. Phys. **111**, 07D313 (2012).

[53] A. Sakai, S. Minami, T. Koretsune, T. Chen, T. Higo, Y. Wang, T. Nomoto, M. Hirayama, S. Miwa, D. Nishio-Hamane *et al.*, Nature (London) **581**, 53 (2020).

[54] S. N. Guin, K. Manna, J. Noky, S. J. Watzman, C. Fu, N. Kumar, W. Schnelle, C. Shekhar, Y. Sun, J. Gooth *et al.*, NPG Asia Mater. **11**, 16 (2019).

[55] S. N. Guin, P. Vir, Y. Zhang, N. Kumar, S. J. Watzman, C. Fu, E. Liu, K. Manna, W. Schnelle, J. Gooth *et al.*, Adv. Mater. **31**, 1806622 (2019).

[56] J. Xu, W. A. Phelan, and C.-L. Chien, Nano Lett. **19**, 8250 (2019).

[57] M. Dyakonov and V. Perel, Phys. Lett. A **35**, 459-460 (1971).

[58] S. Murakami, N. Nagaosa, and S.-C. Zhang, Science **301**, 1348-1351 (2003).

[59] J. Sinova, D. Culcer, Q. Niu, N. A. Sinitsyn, T. Jungwirth, and A. H. MacDonald, Phys. Rev. Lett. **92**, 126603 (2004).

[60] J. Sinova, S. O. Valenzuela, J. Wunderlich, C. H. Back, and T. Jungwirth, Rev. Mod. Phys. **87**, 1213 (2015).

[61] G. Y. G. Guo, S. Murakami, T.-W. Chen, and N. Nagaosa, Phys. Rev. Lett. **100**, 096401 (2008).

[62] J. Qiao, J. Zhou, Z. Yuan, and W. Zhao, Phys. Rev. B **98**, 214402 (2018).

[63] J. H. Ryoo, C.-H. Park, and I. Souza, Phys. Rev. B **99**, 235113 (2019).

[64] M. Gradhand, D. V. Fedorov, F. Pientka, P. Zahn, I. Mertig, and B. L. Györffy, Phys. Rev. B **84**, 075113 (2011).

[65] M. Morota, Y. Niimi, K. Ohnishi, D. H. Wei, T. Tanaka, H. Kontani, T. Kimura, and Y. Otani, Phys. Rev. B **83**, 174405 (2011).

[66] K. Ando, S. Takahashi, K. Harii, K. Sasage, J. Ieda, S. Maekawa, and E. Saitoh, Phys. Rev. Lett. **101**, 036601 (2008).

[67] O. Mosendz, V. Vlaminck, J. E. Pearson, F. Y. Fradin, G. E. W. Bauer, S. D. Bader, and A. Hoffmann, Phys. Rev. B **82**, 214403 (2010).

[68] A. Azevedo, L. H. Vilela-Leão, R. L. Rodríguez-Suárez, A. Lacerda Santos, and S. M. Rezende, Phys. Rev. B **83**, 144402 (2011).

[69] A. Ganguly, K. Kondou, H. Sukegawa, S. Mitani, S. Kasai, Y. Niimi, Y. Otani, and A. Barman, Appl. Phys. Lett. **104**, 072405 (2014).

[70] L. Liu, T. Moriyama, D. C. Ralph, and R. A. Buhrman, Phys. Rev. Lett. **106**, 036601 (2011).

[71] G. Guo, J. Appl. Phys. **105**, 07C701 (2009).

[72] Y. Yao and Z. Fang, Phys. Rev. Lett. **95**, 156601 (2005).

[73] G. Mihajlović, J. E. Pearson, M. A. Garcia, S. D. Bader, and A. Hoffmann, Phys. Rev. Lett. **103**, 166601 (2009).

[74] H. Hung, G. Luo, Y. Chiu, P. Chang, W. Lee, J. Lin, S. Lee, M. Hong, and J. Kwo, J. Appl. Phys. **113**, 17C507 (2013).

[75] V. Vlaminck, J. E. Pearson, S. D. Bader, and A. Hoffmann, Phys. Rev. B **88**, 064414 (2013).

[76] T. Seki, Y. Hasegawa, S. Mitani, S. Takahashi, H. Imamura, S. Maekawa, J. Nitta, and K. Takanashi, Nat. Mater. **7**, 125 (2008).

[77] S. Watt and M. Kostylev, Phys. Rev. B **101**, 174422 (2020).

[78] K. Ando and E. Saitoh, J. Appl. Phys. **108**, 113925 (2010).

[79] K. Kondou, H. Sukegawa, S. Mitani, K. Tsukagoshi, and S. Kasai, Appl. Phys. Express **5**, 073002 (2012).

[80] L. Liu, C.-F. Pai, Y. Li, H. Tseng, D. Ralph, and R. Buhrman, Science **336**, 555 (2012).

[81] C. Hahn, G. de Loubens, O. Klein, M. Viret, V. V. Naletov, and J. Ben Youssef, Phys. Rev. B **87**, 174417 (2013).

[82] X. Sui, C. Wang, J. Kim, J. Wang, S. H. Rhim, W. Duan, and N. Kioussis, Phys. Rev. B **96**, 241105(R) (2017).

[83] C.-F. Pai, L. Liu, Y. Li, H. Tseng, D. Ralph, and R. Buhrman, Appl. Phys. Lett. **101**, 122404 (2012).

[84] F. Freimuth, S. Blügel, and Y. Mokrousov, Phys. Rev. Lett. **105**, 246602 (2010).

[85] P. Jadaun, L. F. Register, and S. K. Banerjee, Proc. Natl. Acad. Sci. USA **117**, 11878 (2020).

[86] H. Xu, J. Wei, H. Zhou, J. Feng, T. Xu, H. Du, C. He, Y. Huang, J. Zhang, Y. Liu *et al.*, Adv. Mater. **32**, 2000513 (2020).

[87] M. H. Guimaraes, G. M. Stiehl, D. MacNeill, N. D. Reynolds, and D. C. Ralph, Nano Lett. **18**, 1311 (2018).

[88] B. Zhao, D. Khokhriakov, Y. Zhang, H. Fu, B. Karpiak, A. M. Hoque, X. Xu, Y. Jiang, B. Yan, and S. P. Dash, Phys. Rev. Res. **2**, 013286 (2020).

[89] J. Han, A. Richardella, S. A. Siddiqui, J. Finley, N. Samarth, and L. Liu, Phys. Rev. Lett. **119**, 077702 (2017).

[90] A. Mellnik, J. Lee, A. Richardella, J. Grab, P. Mintun, M. H. Fischer, A. Vaezi, A. Manchon, E.-A. Kim, N. Samarth *et al.*, Nature (London) **511**, 449 (2014).

[91] Y. Zhang, Y. Sun, and B. Yan, Phys. Rev. B **97**, 041101(R) (2018).

[92] S. Thirupathaiah, Y. S. Kushnirenk, K. Koepernik, B. R. Piening, B. Buechner, S. Aswartham, J. van den Brink, S. V. Borisenko, and I. C. Fulga, SciPost Phys. **10**, 004 (2021).

[93] K. Riedl, Y. Li, R. Valentí, and S. M. Winter, Phys. Status Solidi (b) **256**, 1800684 (2019).

[94] I. I. Mazin, M. Shimizu, N. Takemori, and H. O. Jeschke, Phys. Rev. Lett. **123**, 267001 (2019).

[95] M. Iakovleva, O. Janson, H.-J. Grafe, A. P. Dioguardi, H. Maeter, N. Yeche, H.-H. Klauss, G. Pascua, H. Luetkens, A. Möller, B. Büchner, V. Kataev, and E. Vavilova, Phys. Rev. B **100**, 144442 (2019).

[96] T. Mashoff, J. Regel, K. Medjanik, G. Schönhense, M. Huth, J. Müller, M. Lang, R. Valentí, M. Baumgarten, and H.-J. Elmers, Phys. Status Solidi (b) **256**, 1800674 (2019).

[97] M. Shimizu, N. Takemori, D. Guterding, and H. O. Jeschke, Phys. Rev. B **101**, 180511(R) (2020).

[98] M. Shimizu, N. Takemori, D. Guterding, and H. O. Jeschke, Phys. Rev. Lett. **121**, 137001 (2018).

[99] K. Nawa, O. Janson, and Z. Hiroi, Phys. Rev. B **96**, 104429 (2017).

[100] W. Shi, B. Wieder, H. Meyerheim *et al.*, Nat. Phys. **17**, 381 (2021).

[101] S. N. Guin, Q. Xu, N. Kumar, H.-H. Kung, S. Dufresne, C. Le, P. Vir, M. Michiardi, T. Pedersen, S. Gorovikov *et al.*, Adv. Mater., **33** 2006301 (2021).

[102] C. Le, Y. Zhang, C. Felser, and Y. Sun, Phys. Rev. B **102**, 121111(R) (2020).

[103] Y. Zhang, Q. Xu, K. Koepernik, C. Fu, J. Gooth, J. van den Brink, C. Felser, and Y. Sun, New J. Phys. **22**, 093003 (2020).

[104] M. Yao, K. Manna, Q. Yang, A. Fedorov, V. Voroshnin, B. V. Schwarze, J. Hornung, S. Chattopadhyay, Z. Sun, S. N. Guin *et al.*, Nat. Commun. **11**, 1 (2020).

[105] Q. Xu, G. Li, Y. Zhang, Q. Yang, Y. Sun, and C. Felser, ACS Catal. **10**, 5042 (2020).